



Variable white dwarfs in the SuperWASP archive. A search for sub-stellar and planetary companions

Francesca Faedi

Supervisors:

Matt Burleigh

Richard West

Mike Goad

Thesis to be submitted for the degree of
Doctor of Philosophy
at the University of Leicester.

X-ray & Observational Astronomy Group

Department of Physics and Astronomy

University of Leicester

December 13, 2009

Abstract

This PhD thesis is an investigation of the characteristics and detection limits for transit signals due to sub-stellar and terrestrial companions to white dwarfs in the SuperWASP survey.

The work is described as follow: there is an introductory chapter on the field of white dwarfs and exoplanets. In chapter 2 I describe the SuperWASP project, the two SuperWASP telescopes the problematics of data analysis and the results obtained so far. In chapter 3 I discuss the simulations I performed to investigate the characteristics of the transit signals due to sub-stellar and planetary companions to white dwarfs and the detection limits derived for SuperWASP light-curves by means of my optimised version of Box-Least Square (BLS) algorithm. In chapter 4 I present a study of 194 spectroscopically identified white dwarfs which are a cross-correlation of the McCook & Sion catalogue and the SuperWASP archive. In addition, I derive upper limits to the frequency of sub-stellar and planetary companions to white dwarfs using my sample and the results obtained from my simulations. In chapter 5 I present a variability study for the sample of 194 white dwarfs. I have investigated the light-curves of the 194 white dwarfs in the sample to search for photometric variability due to non-radial pulsations, the presence of star spots in magnetic white dwarfs, and to irradiation and reflection effects on low-mass close companions. Finally, in chapter 6 I conclude and present my project for future work.

Acknowledgements

Where to start? First of all I need and I want to thank Professor Giovanni Bignami e Professor Patrizia Caraveo. I really never had the opportunity to properly say thank you for believing in me and for giving me the possibility of pursuing my interest in Astrophysics. Your personal and professional opinion was the reason why I was selected for a PhD in Astronomy at the University of Leicester. It is also thanks to you if I have now the opportunity to pursue my interests as a post doctoral researcher at Queen's University Belfast.

It is rhetorical to say that I thank my "three" Supervisors. Yes, three. As I am a special student, I did not have just one but three: Matt Burleigh, Mike Goad and Richard West. Thank you guys for teaching me all I know, for helping me to understand things and to introduce me to the world of research. Thank you Matt, because you have introduced me to the degenerate world of white dwarf stars!! I want to say a particular thank to Mike and Richard because you have always been listening to my good, bad, strange etc. ideas and because you guided me through my PhD. You are very good teachers.

Since I moved to Leicester and since Ricky moved with me, we found immediately a new home. That is also because we met a lot of friends some of which are now very good friends! I have been introduced to the heavy beer drinking by Graham, Mike, Richard, Matt, Andy, Jonny and Steve and many others! OK, OK, no just that, but Ricky and I, we shared with you guys a lot of pleasant nights in the pub!! During these last three and a half years I switched from an Italian style to and hybrid Italo-English style which I like!!! I got used to go out at 6 p.m. instead of 11p.m. and

to enjoy pub food and good beers, of course always under the supervision of the Master's!! Thanks guys for sharing this with me.

I need to thank Jonny and Jenny because you have always been very kind and helped me from the beginning with my English and with all the rest. I hope this reciprocate. Graham and Lisa (Graham be nice at my viva!!! Please!!) Kriss and Mike, well guys I love you and you know that!! Kriss you have always been nice and listened to my good and bad moods. You know I will do the same for you!

I have to say thank you to Sarah for helping me with my thesis and Merv for all the open days!

How can I forget Gauthier. I want to thank you for being a very good friend and for a lot of pleasant nights with very good food!! I also want to say thank you to Gail and her kids, Rafael, Antonios, Nick, Emma and all the people that were coming to the morning coffee for foreigners at café Piazza!!

Thanks also to Mike Watson for giving me the opportunity to work for him. Thanks to all the secretaries Pat, Pam and Lisa, you have always been very nice and helpful. Finally thanks to all the people I might have forgotten here ... sorry I am very tired and absolutely need a long holiday to recover!!

Ringraziamenti

Innanzitutto ringrazio tutte le persone che mi sono state sempre vicino e che mi hanno sostenuto in ogni passo che mi ha portato fino all'ottenimento di questo dottorato di ricerca. Forse non tutti sanno quanto lavoro e fatica richiede portare a termine un dottorato di ricerca e quindi potrebbero sottovalutare l'importanza che il loro continuo appoggio ha significato durante questi tre anni per la sottoscritta. GRAZIE di cuore. Vorrei dedicare questa fatica di Ercole ad una persona in particolare, Mina. Cara Mina tu sai che sai quello che significa ottenere un dottorato! Vorrei dedicarti questa mia personale vincita per avermi sempre capita e sostenuta. Mi dispiace di non avere fatto prima per festeggiare con te!

Certamente non posso che ringraziare, anzi direi di piú, tutta la mia famiglia: mia mamma Patrizia e mio babbo Giovanni, perché senza di voi non sarei mai potuta arrivare dove sono. Mi avete sempre sostenuto in ogni mia scelta anche quando questo significava andare a vivere lontano da casa. Grazie per avermi insegnato che le cose nella vita si guadagnano a fatica e anche per avermi insegnato ad affrontare la vita! Mi mancate anche voi!! Ovviamente devo anche ringraziare mia sorella Ilaria, e mio fratello Fabio perché quando torno a casa litighiamo come se non fossi mai andata via!! Grazie per farmi sentire sempre parte della famiglia!!

Ora mi manca di ringraziare l'altra mia famiglia; I Giabbani, tutti! ma in particolare Sara e Vanni. Ormai lo sapete che siete la mia seconda famiglia.

Un posto speciale é ovviamente solamente dedicato a Riky. Non solo perché mi vuoi bene (tanto anche io!), e me ne hai voluto tanto anche durante quest'ultimo periodo dove le mie crisi di depressione e di nervi credo avrebbero messo alla prova anche un

santo! Ma anche perché mi hai sempre spronato ad andare avanti e mi hai sempre seguito mettendo molte volte i miei bisogni prima dei tuoi! Lo sai che occupi un posto speciale nel mio cuore.

Ovviamente un saluto ed un abbraccio in Italiano alla gang di Italiani di Leicester: Agnese, Valentina, Fabrizio, Giuseppe, Emilio, Eleonora, e ancora Ivan, Emanuele, Davide, Marco, e tutti gli altri.

In fine vorrei spendere due righe per ringraziare tutti quelli che mi hanno sempre scoraggiato dal seguire i mie interessi e i miei sogni, grazie per avermi insegnato che non é sempre facile per tutti, e che nella vita ci si puó sbagliare!

CONTENTS

1	Introduction	1
1.1	The discovery of white dwarfs	1
1.2	How stars become white dwarfs	4
1.2.1	The Pauli principle and the degenerate core of WDs	6
1.3	Properties of white dwarfs	8
1.3.1	WDs spectra and spectral classification	8
1.3.2	The importance of white dwarfs to the evolution of galaxies	10
1.3.3	WDs luminosity function: insights on the Milky Way	11
1.4	White dwarfs' photometric variability	13
1.4.1	Pulsations, star spots, irradiation and reflection	13

1.4.2	Sub-stellar companions to white dwarfs	17
1.4.3	Can planets survive stellar evolution?	19
1.5	Extra-solar planets: detection methods	21
1.5.1	The transit method	25
1.5.2	Radial Velocity	29
1.5.3	Timing, astrometry, microlensing and imaging	30
2	The SuperWASP project	35
2.1	Introduction	36
2.2	Instrumentation	38
2.2.1	SuperWASP telescopes	40
2.2.2	Data acquisition system	42
2.2.3	Data acquisition software	43
2.2.4	SuperWASP pipeline	44
2.2.5	Data archive	45
2.3	SuperWASP observing strategy	48
2.4	SuperWASP data	50

2.5	De-trending algorithm	54
2.6	Planet detection and candidate selection	55
2.6.1	BLS algorithm	56
2.6.2	Candidate selection	57
2.7	Summary	57
3	Simulations	59
3.1	Introduction	60
3.2	Simulations	63
3.2.1	Characteristics of the transit signals	64
3.2.2	Synthetic SuperWASP light-curves	67
3.2.3	Detecting transit signals	69
3.3	Estimating SN_E	75
3.4	Characterisation of the BLS response	81
3.4.1	BLS response to pure noise: testing the algorithm false detection rate	82
3.5	Results	87

3.5.1	Optimised BLS implementation	93
3.6	Conclusions	99
4	Data analysis	108
4.1	White Dwarfs in the SuperWASP archive	109
4.2	Visual inspection of SuperWASP light-curves	113
4.3	Results	116
4.4	Limits to companions' frequency	118
4.5	Conclusion	124
5	Photometric variability	135
5.1	Introduction	136
5.2	Data Analysis	138
5.3	MS Peg	146
5.3.1	Variability results	150
5.3.2	WD0353+284	153
5.3.3	WD1024+326	157
5.3.4	HZ 43	158

5.3.5	GD 358	162
5.4	conclusion	164
6	Conclusions	170
6.1	Conclusions	170
6.1.1	Sub-stellar and planetary companions to white dwarfs	171
6.1.2	WDs variability	174
6.2	Future work	175
6.2.1	A search for hidden white dwarfs by occultations due to low-mass stellar companions	175
6.2.2	Technique	177
	References	181

LIST OF FIGURES

1.1	Hertzprung-Russell diagram	6
1.2	Extra-solar planet detection techniques	22
1.3	Sketch of a planetary transit	24
1.4	Geometry of a transit event	26
1.5	Transit duration	28
2.1	Location of SuperWASP telescopes	39
2.2	SuperWASP-North telescope	40
2.3	SuperWASP filter	42
2.4	Number of stars per SuperWASP field	47
2.5	Average number of points per star	48

2.6	SuperWASP object RMS versus Magnitude	50
2.7	Vignetting distortion of SuperWASP cameras	52
3.1	Comparison of the transit light-curve of a Jupiter across a sun-like star with an Earth across a white dwarf	65
3.2	Contour of transit duration and transit depth	68
3.3	Contour of transit Probability	69
3.4	Model BLS-box function	71
3.5	Examples of simulated transit light-curves	72
3.6	Expected Signal-to-Noise (SN_E) from white noise light-curves of $\sigma = 1\%$	75
3.7	Expected SN_E for white noise of $\sigma = 0.5\%$	76
3.8	Expected SN_E for a white noise light-curve of $\sigma = 10\%$	77
3.9	Estimated S/N vs orbital period for the simulated transiting systems	79
3.10	BLS periodogram for pure white noise	83
3.11	Probability Distribution Functions for SDE	86
3.12	Example of a transit folded light-curve	88
3.13	Transit light-curve folded on a random period	89

3.14	Example of a BLS periodogram	91
3.15	PDF for the optimised BLS routine	95
3.16	Improved BLS periodogram	96
3.17	SDE values for transit signals detected in a SuperWASP light-curve of $V \sim 12$	97
3.18	SDE values for transits detected in a $V \sim 13$ and $V \sim 15$ light-curve	98
4.1	Sky coverage for the sample of 194 white dwarfs	109
4.2	Light-curve examples of 4 white dwarfs in the sample	114
4.3	Synthetic transit light-curve for an Earth-sized body	115
4.4	Binomial probability distribution	119
4.5	Upper-limits to the frequency of companions to WDs	120
4.6	Revised upper-limits to WDs companions frequency	121
4.7	Frequency upper-limits for the sample of 194 WDs	123
5.1	Lomb-Scargle FAP for white noise simulations	141
5.2	Schwarzenberg-Czerny Post-Mortem analysis	143
5.3	Lomb-Scargle and CLEAN periodograms for MS Peg	145

5.4	MS Peg periodogram and folded light-curve	147
5.5	Period error estimate by Gaussian fit	148
5.6	2'×2' Aladin image for MS Peg	151
5.7	MS Peg raw data	152
5.8	WD0353+284 periodogram and folded light-curve for SuperWASP 2004 data	154
5.9	WD0353+284 2006 data	155
5.10	DFT residual for WD0353+284	156
5.11	WD1026+326 periodogram and folded light-curve	159
5.12	HZ 43 periodogram and folded light-curve	161
5.13	HZ 43 Gaussian fit and period confidence interval	162
5.14	GD 358 Lomb-Scargle periodogram	163
5.15	GD 358	165
5.16	Periodogram and folded light-curves for the variable WDs in the sample	167
5.17	continue from Figure 5.16.	169
6.1	DE CV _n folded light-curve	177

6.2 V471 Tau folded light-curve	180
---	-----

LIST OF TABLES

- 3.1 First results from simulations 92
- 3.2 BLS detection rates 98
- 3.3 SuperWASP detection limits 102

- 4.1 WDs in the SuperWASP archive 125

- 5.1 Variable WDs 168

Chapter 1

Introduction

1.1 The discovery of white dwarfs

White dwarf stars are compact objects formed when a progenitor star ceases burning helium and is not massive enough to produce elements heavier than helium giving rise to a gravitational collapse. The vast majority of the stars in our galaxy ($\sim 97\%$), including the Sun, will finally evolve towards the white dwarf state. The first discovery of any such star dates back to the nineteenth century when Sirius, the brightest star in the sky, was revealed to be a binary system by Friedrich Wilhelm Bessel in 1844 and subsequently confirmed by Alvan Clark in 1862 (orbital period ~ 50 years). The measurements taken by Clark during apastron, when the stars are at the maximum separation ($\sim 10''$), revealed their extremely different luminosities ($L_A = 23.5L_\odot$ and $L_B = 0.03L_\odot$). In 1910 the mass of the companion was also derived from astrometric measurements, as $0.94M_\odot$ (Boss, 1910), which give a model-independent dynamical mass from Kepler's laws (a more recent value

is $0.984 M_{\odot}$, Holberg et al. 1998). At the time of the subsequent apastron configuration, when new spectroscopic techniques were available, Walter Adams obtained the spectrum of Sirius B and revealed the enigma of white dwarf stars (Adams, 1915). Although Sirius B is a thousand times fainter than Sirius A, its spectrum is identical to that of Sirius A: “*identical in all respect so far as can be judged from a close comparison of the spectra*”. Contrary to any expectation at that time Sirius B was found to be a hot, blue-white star emitting the majority of its energy in the ultraviolet. Indeed in the UV/soft X-ray band Sirius B becomes brighter than Sirius A (a modern value of the temperature of Sirius B is $T_{\text{eff}} = 25,193$ K; Barstow et al. 2005, while Sirius A has a temperature of $T_{\text{eff}} = 9,940$ K; Adelman 2004). A similar puzzle was provided by two other well known stars: 40 Eridani B first discovered by William Herschel in 1783, and Van Maanen 2 discovered by Van Maanen (1917). The measurement of their parallaxes showed the two stars to be many magnitudes fainter than other stars of similar spectral type. Many faint white stars were found with high proper motion, i.e. the angular change in position over time, indicating that they could be low-luminosity stars close to the Earth, and hence white dwarfs. Willem Luyten appears to have been the first to use the term *white dwarf* when he studied these stars in 1922 (Luyten 1922b, Luyten 1922a, and Eddington 1924). By 1939, 18 white dwarfs had been discovered (Schatzman, 1958). By 1950, over one hundred white dwarfs were known (Luyten, 1950), and by 1999, over 2,000 were known (McCook & Sion, 2003). Since then the Sloan Digital Sky Survey (SDSS) has found over 9,000 white dwarfs, most of which were previously unknown (Eisenstein et al., 2006).

Knowing the effective temperature and luminosity of Sirius B and using the Stefan-

Boltzmann equation the radius of the star could be estimated. Stefan-Boltzmann's law relates the total energy irradiated by a body to its surface temperature by:

$$L = 4\pi R^2 \sigma T_{\text{eff}}^4 \quad (1.1)$$

where L is the star luminosity, σ is the Stefan-Boltzmann constant, R is the stellar radius and T_{eff} is the star effective temperature. So the radius of Sirius B in solar radii is obtained as:

$$\frac{R}{R_{\odot}} \sim \left(\frac{T_{\odot}}{T_{\text{eff}}} \right)^2 \sqrt{\frac{L}{L_{\odot}}} \quad (1.2)$$

where R_{\odot} , T_{\odot} and L_{\odot} are the radius, temperature and luminosity of the Sun respectively. The estimated radius for Sirius B was $R_{\text{WD}} \sim 0.008 R_{\odot}$ (a recent value for the radius of Sirius B is $0.00864 R_{\odot}$, Holberg et al. 1998) for a star with a mass of $\sim 1 M_{\odot}$. Thus, surprisingly, Sirius B was found to have the mass of the Sun confined within a volume smaller than the Earth ($R_{\oplus} = 0.00916 R_{\odot}$). This result implies an extremely high stellar density ($\rho \sim 3.0 \times 10^6 \text{ g cm}^{-3}$), a million times that of a normal star, and a surface gravity (g) of about $4.0 \times 10^6 \text{ ms}^{-2}$ which is approximately 15,000 times larger than the surface gravity of the Sun ($g_{\odot} \sim 274 \text{ ms}^{-2}$) and $\sim 408,000$ times larger than that of the Earth. An independent test of the high density of Sirius B was conducted in 1920 by Adams who, following the suggestion of Einstein's theory of general relativity (1907), measured the redshift of light in the strong gravitational field of Sirius B. Adams estimated a gravitational redshift (λ) of $\sim 19 \text{ kms}^{-1}$. This measurement was more recently refined by Greenstein et al. (1971) who found a value of $\sim 85 \text{ kms}^{-1}$. Although Adams's estimate was incorrect (due to strong contamination in the measurement by light from Sirius A) it confirmed the strong gravitational field of Sirius B and provided one of the first test of Einstein's

general theory of relativity. The effect of the extremely high gravitational field is directly observable in the spectra of white dwarfs which show very broad hydrogen absorption lines. For example a recent spectrum of Sirius B is shown in Figure 4 of Barstow et al. (2005).

The first observational results on white dwarfs were so unexpected that astronomers struggled to understand their physics. The advent of the theory of quantum mechanics finally provided the tools needed to describe the equation of state of the matter in the degenerate core of these objects. Solving the mystery behind the stars with a mass similar to the Sun and the size of the Earth yielded a powerful demonstration of the combined action of the Pauli's exclusion principle and the Heisenberg uncertainty principle (see e.g. Fowler 1926 and Chandrasekhar 1935).

1.2 How stars become white dwarfs

All the stars less massive than $8 M_{\odot}$ will end their lives as white dwarfs. White dwarf stars are manufactured in the core of low and intermediate mass stars near the end of their life at the end of the asymptotic giant branch (AGB) phase of stellar evolution. A star spends most of its life in the main-sequence phase during which all of the hydrogen is converted into helium via nuclear reactions in the core (see Figure 1.1). When the hydrogen becomes depleted, shell burning of hydrogen becomes the main energy source. Since the core no longer produces significant luminosity this naturally results in its collapse (Schönberg & Chandrasekhar 1942). The core and the envelope become dynamically decoupled, when the core contracts and the temperature increases a greater pressure is created on the external layers and

the shell's energy production is rapidly increased. As a consequence the envelope expands and the star swells at a nearly constant luminosity. During this phase of pure hydrogen-shell burning rapid core contractions and envelope expansions carries the star to the beginning of red giant evolution (Iben 1965), this phase is indicated as RGB phase in Figure 1.1. As evolution along the red giant branch (RGB) track continues the star develops a convection zone because of the effective temperature drop due to the envelope expansion. The star then ignites the helium in a non degenerate core. For low-mass stars the core becomes partially degenerate before helium ignition occurs. The core does not expand and helium flashes are observed (Iben & Renzini, 1983), see also Figure 1.1 at the top of the RGB phase. Helium flashes are explosives releases of energy absorbed by the overlying layers of the envelope, causing mass loss from the star surface (Iben & Renzini, 1983).

During the Asymptotic Giant Branch (AGB) phase (see Figure 1.1), the helium is exhausted in the core and it burns in a shell surrounding a Carbon-Oxygen (C/O) degenerate core. The star reaches its maximum radius and loses most of its mass. At the top of the AGB track the star undergoes thermal pulses caused by the helium shell that periodically turns on and off, and the onset of super-wind eventually ejects the remainder of the star's envelope (Cassinelli 1979 and Castor 1981). The physical nature of the mechanism behind mass loss is not well understood (Iben & Renzini, 1983). When leaving the AGB track the star becomes unstable and ejects the majority of its atmosphere to be later observed as planetary nebula (PN) (Iben & Renzini, 1983). At this point the core of the star collapses under gravity and becomes the pre-white dwarf. During the PN phase the star is left with a C/O degenerate core surrounded by a thin layer of residual H and He. The star can reach very high temperatures and luminosities, see Figure 1.1. The development of the

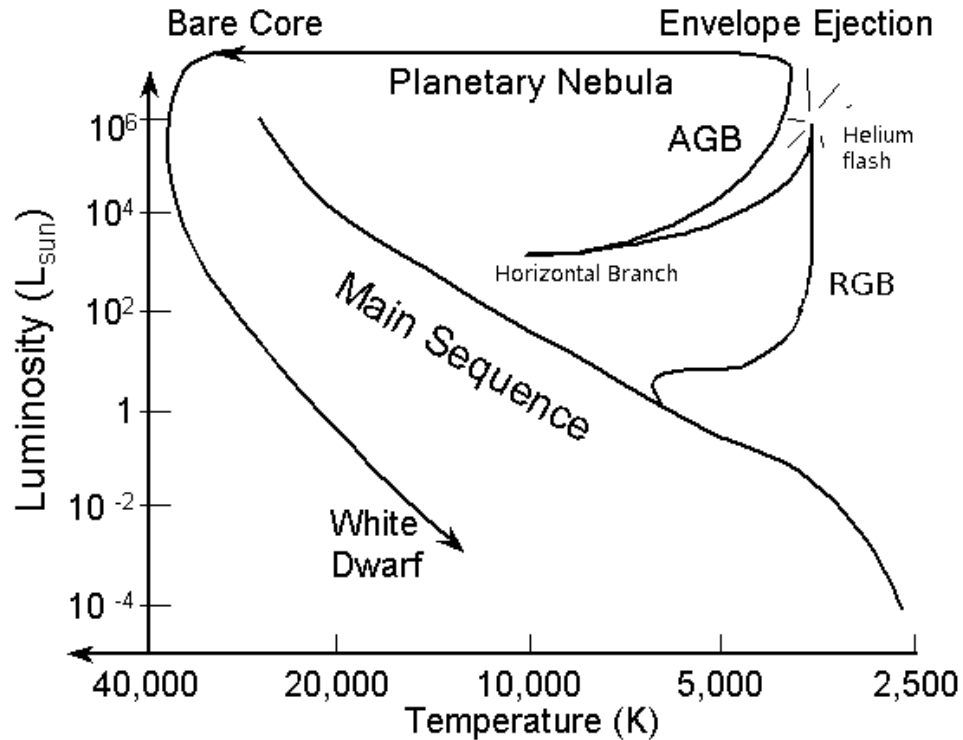


Figure 1.1: Hertzsprung-Russell diagram (HR). Luminosity (L_{\odot}) versus Temperature (Kelvin). The Figure shows the different stages of post main-sequence stellar evolution. Indicated is the Main Sequence, the Red Giant Branch (RGB), the Horizontal Branch (HB), the Asymptotic Giant Branch (AGB), the Planetary Nebula (PN) phases of stellar evolution towards the final evolution end point of white dwarfs. Also indicated is the onset of helium flashes and the stage of the stellar envelope ejection at the top of the RGB and AGB tracks respectively.

strong wind that interacts with the material ejected by the AGB star dissipates the nebula's gas in approximately 50,000 years progressively unveiling the newly born white dwarf (Iben & Renzini 1983 and references therein).

1.2.1 The Pauli principle and the degenerate core of WDs

White dwarfs are born from extremely hot collapsed objects which can only cool off. For all but the coolest white dwarf the core is a plasma consisting of ions and

degenerate electrons (e^-), for which the energy sources of nuclear reaction have been completely depleted. The degenerate pressure of the e^- is therefore the main force balancing gravitational collapse, as the thermal pressure of the ions is negligible in comparison (Fowler, 1926). Thus, the mechanical structure of white dwarfs is nearly entirely specified by the degenerate electrons. As the pressure of the degenerate e^- depends weakly on the temperature they do not contribute to the thermal reservoir of the star, and cannot give up a significant amount of kinetic energy. Pauli's exclusion principle states that any two electrons cannot occupy the same quantum state, thus all lower energy levels are occupied by e^- that are no longer free. The majority of the thermal energy is therefore provided by the non-degenerate ions. This implies that an isolated white dwarf shines at the expense of its thermal ions.

The curious relation between the mass and the radius of a white dwarf ($M_{\text{WD}} R_{\text{WD}}^3 = \text{constant}$) is also explained by electron degeneracy. Because of the Heisenberg uncertainty principle ($\Delta X \Delta P \geq \hbar/2$), the electrons must be more closely confined to generate a larger degeneracy pressure required to support a more massive star. Thus, the volume of a white dwarf is inversely proportional to its mass and more massive white dwarfs are actually smaller (Mazzitelli & Dantona 1986). Similarly, relativistic degeneracy is also responsible for the existence of a limiting mass above which white dwarfs cannot exist, the Chandrasekhar mass $M_{\text{ch}} = 1.4 M_{\odot}$ (Chandrasekhar 1935). Another important characteristic of the degenerate core is its ability to conduct heat. The electrons in the degenerate gas can travel long distances before having a collision with a nucleus, thus energy is better carried out by electron conduction rather than radiation. Indeed, this is so efficient that the internal regions of white dwarfs are nearly isothermal ($\sim 99\%$ of the entire mass). The temperature drops significantly only in the outer non degenerate surface layers

which account for $\sim 1\%$ of the white dwarf mass, and also control the total amount of energy slowly released.

1.3 Properties of white dwarfs

The defining characteristic of white dwarfs is the fact that their mass is typically of the order of half that of the Sun, while their size is similar to that of a planet. Their compact degenerate nature explains their large average densities, surface gravities and low luminosities. The properties of these objects are therefore related to their degenerate nature and some of their peculiar properties can be determined directly from observations.

1.3.1 WDs spectra and spectral classification

Analyses of spectra of white dwarfs show that their effective temperatures range from ~ 4000 K (Bergeron et al., 1994) for the coolest WD up to $\sim 170,000$ K for the hottest white dwarf (Werner et al. 2008). This large range in effective temperature is reflected in the range of luminosity covered by these stars, exceeding seven orders of magnitudes ($L \propto T_{\text{eff}}^4$). From spectral analyses we can also infer their surface gravities as $\log g \sim 8$ (cm s^{-2} ; with $g = GM_{\star}/R_{\star}^2$). The width of the observed spectral lines depends on the density of the particles in the atmosphere of the star, which in turn depends on the surface gravity. The value of the mass and the radius of the star can then be estimated from $\log g$. However, in the spectra of cooler and older white dwarfs the H and He features are no longer visible ($T_{\text{eff}} < 5000$ K) and

the measurement of the surface gravity is more difficult as it is not possible to rely on line profile analyses to infer the atmospheric composition of the star (Bergeron et al., 1994) and a different approach is needed. In such cases, a parallax measurement can be used to estimate the radius and the mass of the star, and hence $\log g$.

The typical structure of a white dwarf is that of a stratified object with a mass of $\sim 0.6 M_{\odot}$ (Fontaine et al. 2001, Bergeron et al. 1994) consisting of a carbon-oxygen core surrounded by a thin helium envelope, in turn surrounded by a thin hydrogen layer. Heavy elements diffuse downward in white dwarf atmospheres due to gravitational settling in their high gravitational fields (Schatzman 1945).

The spectral energy distribution of white dwarfs is determined by the effective temperature, the pressure stratification (determined by the surface gravity) and the chemical composition of the surface layers. White dwarfs are classified according to the presence and strength of absorption lines in their spectra. The current classification scheme has been derived by Sion et al. (1983):

DA: only Balmer lines, no He I or metals

DB: He I lines, no hydrogen or metals

DC: continuous spectrum

DO: He II strong, He I or hydrogen

DZ: metal lines only

DQ: carbon features

Where ‘D’ stays for *dwarfs* and the second capital letter indicates the dominant spectroscopic feature observed in the optical spectrum. The majority of white dwarfs, $\sim 84\%$ (Winget & Kepler 2008) have hydrogen dominated atmospheres (DA), with the vast majority of the remaining (16%) being He-dominated atmosphere, (the DOs

and DBs) (Eisenstein et al., 2006). Nevertheless, a well established class (DAZ) of white dwarfs with metal contaminated atmospheres is also known (Koester et al. 1997, Holberg et al. 1997, Zuckerman et al. 2003, Koester et al. 2005), and more recently C-atmosphere DQ WDs have been discovered (Dufour et al. 2007). Moreover, there is observational evidence that some spectral evolution is taking place in white dwarfs. The ratio of DA to non-DA white dwarfs changes along the cooling sequence with the variation of the star's effective temperature (Huegelmeier & Dreizler 2009, and Malo et al. 1999). Thus, some white dwarfs change the chemical composition of their surface layers from helium to hydrogen-dominated, and again to helium, during the star's lifetime. However, to date there is no convincing explanation for such a phenomenon (Fontaine et al. 2001).

1.3.2 The importance of white dwarfs to the evolution of galaxies

White dwarfs are the only stable final evolutionary state for the $\sim 97\%$ of all stars (Winget & Kepler, 2008), thus the evolution towards white dwarfs is the dominant channel in galaxies. The actual population of white dwarfs therefore constrains an ensemble of information on the evolution of individual stars from birth to death, on the previous history of the galaxy and finally on the rate of star formation. The spectroscopic identification of massive white dwarfs, members of relatively young galactic clusters (Reimers & Koester 1982 and Weidemann & Koester 1983) have suggested an upper limit of $\sim 8 M_{\odot}$ to the turn-off mass of white dwarfs' progenitor stars. The majority of white dwarfs have a typical core composition of mostly Carbon and Oxygen (see e.g. Fontaine et al. 2001), the products of helium burning. The

mass distribution of the actual population of isolated white dwarfs is sharply peaked around the mean value of $0.6 M_{\odot}$ (Fontaine et al. 2001), however, low-amplitude tails extended at both ends of the mass spectrum, from ~ 0.3 to $\sim 1.2 M_{\odot}$. This narrow mass distribution is a remarkable property of these stars, and is related to the process of mass loss on white dwarfs progenitors. The extreme difference between the initial main-sequence masses and the final white dwarf masses highlights the very important rôle of mass loss in post main-sequence stellar evolution. Therefore by determining the masses of white dwarfs and tracing their evolution back to their progenitors, it is statistically possible to estimate the total mass loss. This might provide valuable constraints on the little understood mass loss process (Iben & Renzini 1983, van Loon 2008). On the other hand a better understanding on the critical stage of mass loss in stellar evolution can also provide new insights into the total mass budget of the galaxy (Koester & Chanmugam, 1990), for example what is the amount of mass recycled in the interstellar medium, and how much mass is retained in the core of white dwarfs?

1.3.3 WDs luminosity function: insights on the Milky Way

Because nuclear burning is no longer active in their cores, white dwarfs evolve at the expense of their thermal reservoir and slowly fade away to invisibility in about 5 to 10 billion years (Koester & Chanmugam, 1990). This implies the existence of a relation between the age of a white dwarf and its luminosity. Indeed, the faintest observed white dwarfs are also very old and carry information on the early stage of evolution of our galaxy (Mestel 1952 and Dantona & Mazzitelli 1978). Because of their intrinsic faintness, spectroscopic observations of these stars are restricted to

small distances. For example the bulk of the sample of spectroscopically identified white dwarfs (see e.g. McCook & Sion 2003) is confined to within ~ 500 pc from the Sun (Fontaine et al. 2001). The white dwarfs luminosity function (the number of white dwarfs observed per unit of absolute luminosity) shows a deficit in the number of the coolest, oldest white dwarfs at luminosity $L = 10^{-4.5} L_{\odot}$ (see e.g. Liebert et al. 1979 and Liebert et al. 1988). Modelling this absence of the faintest objects with theoretical cooling models provided an estimate to the finite age of the galactic disc (~ 8 Gyr, see Winget et al. 1987; Iben & Laughlin 1989 and Wood 1992, for a full discussion). The cut off in the luminosity function of white dwarfs is not due to an observational selection effect but is simply due to the fact that white dwarfs have not had enough time to cool to fainter magnitudes. A recent estimate of the age of the galactic disc is $\sim 9 \pm 1.5$ Gyr (Leggett et al. 1998, Knox et al. 1999, Bergeron et al. 1995).

Because of their low luminosity, white dwarfs are also considered interesting candidates for the baryonic dark matter halo. The first indication of the galactic dark matter (Ostriker & Peebles 1973, Faber & Gallagher 1979) led to the hypothesis that remnants of stellar evolution of a population of early stars in the galaxy could account for a fraction of the unseen dynamical mass (Larson 1987, Silk 1991). The observed turn over of the luminosity function of white dwarfs by Liebert et al. (1988) provided a direct constraint to the estimate of the ages of the halo population; > 12 Gyr (Tamanaha et al., 1990). Observation of microlensing by the MACHO project (MASSive Compact Halo Objects, Alcock et al. 1993) in the direction of the Large Magellanic Cloud suggested that the most probable candidates for the objects causing the microlensing events are cool white dwarfs (Alcock 2000, Koester 2002 and Calchi Novati et al. 2005). Oppenheimer et al. (2001) conducted a deep proper mo-

tion survey for high velocity halo white dwarfs and appeared to confirm the above result. However, both results remain controversial.

From observations of white dwarfs and constraints given by theoretical cooling models an estimate of the total age of the universe can also be inferred (10.3 ± 2.2 Gyr, see Winget et al. 1987).

1.4 White dwarfs' photometric variability

Photometric observations of white dwarfs are of crucial importance as they can reveal the presence of unseen low-mass stellar and sub-stellar companions via their eclipses (see for example Littlefair et al. 2006) or by means of the presence of sinusoidal modulations in their light-curves (see chapter 5 for a few examples). Magnetic isolated white dwarfs can show light-curve variations due to the presence of star spots on their surfaces. In addition, the detection and analysis of non-radial pulsations of white dwarfs can reveal the internal structure and composition and the mechanical properties of these degenerate objects (Winget & Kepler 2008, Fontaine & Brassard 2008, Koester & Chanmugam 1990).

1.4.1 Pulsations, star spots, irradiation and reflection

The majority of white dwarfs are known to be photometrically stable and are often used as calibration standards for optical and ultra-violet observations (Holberg 2007; and Holberg & Bergeron 2006). However, three different classes of white dwarfs are known to be non-radial pulsators. These are ZZ Ceti stars or DAVs, hydrogen

atmosphere white dwarfs; the DBVs also known as V 777 Her, helium atmosphere WDs; and the GW Vir or DOVs white dwarfs with atmospheres mainly composed of helium, carbon, and oxygen (see Winget & Kepler 2008). These stars show non radial pulsations associated with the excitation and partial ionisation of the most abundant element in their surface layer.

ZZ Ceti stars show non radial g-mode pulsations with variability timescales between a hundred and a thousand seconds. ZZ Ceti stars are observed in a very narrow temperature region around $T_{\text{eff}} \sim 12,000\text{K}$, around the transition region between the radiative and convective atmosphere. At this T_{eff} the partial ionisation and recombination of the hydrogen in the envelope is the mechanism responsible for the excitation of the low-order g-modes across the ZZ Ceti instability (temperature) strip (Fontaine & Brassard 2008). In the case of non-radial pulsation the dominant force restoring the hydrostatic equilibrium in the star is gravity (Winget & Kepler 2008), while for p-modes, radial displacements are favoured and the principal restoring force is pressure (periods of few seconds in white dwarfs). By direct analogy with ZZ Ceti stars Winget et al. (1982) predicted that helium-atmosphere (DB) white dwarfs could also exhibit non-radial oscillations at higher temperatures (around $T_{\text{eff}} \simeq 25,000\text{K}$), the temperature of helium recombination. This prediction was soon after confirmed by the detection of GD 358 (Winget et al. 1982; and chapter 5 this work) a pulsating DB star with a temperature of $T_{\text{eff}} = 24,000\text{K}$ (Kotak et al. 2003). The first object belonging to the GW Vir class of pulsators is represented by the pre-white dwarf PG 1159-035, the first detected such star (McGraw 1979), with temperature between $75,000 \leq T_{\text{eff}} \leq 170,000\text{K}$. The envelope of DOV stars is devoid of hydrogen and is mostly made of a mixture of helium, carbon and oxygen in approximately comparable proportions (Fontaine & Brassard, 2008). However, GW

Vir stars have atmospheric compositions that vary from object to object. For this class of star, non-radial pulsations are driven by the cyclic ionisation of the carbon and oxygen in their atmosphere (Fontaine & Brassard 2008 and references therein).

It has been suggested (Fontaine et al. 1982) that the ZZ Ceti star is a phase of the evolution of every white dwarf, implying that DA white dwarfs are to become ZZ Ceti pulsators as they cool and cross the instability strip. If this is true in general, it means that every white dwarf will become a non-radial pulsator as it cools during its lifetime. Therefore, it is extremely important to certify the purity of these instability strips.

Non-radial pulsations have also been observed in the DA white dwarf component of cataclysmic variables (van Zyl et al. 2004 and Mukadam et al. 2007). This suggests that accretion and mass transfer do not affect the convection/partial ionisation region where the pulsations originate. Finally, the recent detection of non-radial pulsations (Montgomery et al. 2008) in carbon-dominated atmosphere white dwarfs (DQ, Dufour et al. 2007), indicate Hot DQ stars as a fourth, new class of pulsator ($T_{\text{eff}} \sim 20,000\text{K}$).

As mentioned previously photometric variability is also observed in the light-curves of magnetic white dwarfs. About 2% of the total white dwarf population consist of isolated magnetic white dwarfs (Brinkworth et al., 2005). While these stars are rare they are extremely important as they offer the possibility of determining the rotational period of the star. The presence of spots on the stellar surface cause changes in the observed stellar brightness as the spots rotates in and out of view, revealing the rotational period of the star. Rotation periods in isolated non-magnetic white dwarfs

is otherwise difficult to measure due to heavy gravitational broadening of their spectral lines (Brinkworth et al., 2005). A few very highly magnetic white dwarfs also display photometric variability due to changes in the magnetic field strength and structure as the star rotates, resulting from changes in the opacity of the outermost layers of the stellar atmosphere, as in the case of RE J0317-853 (Barstow et al. 1995, magnetic dichroism, see Ferrario et al. 1997). The detection and characterisation of variability connected to the star's magnetic field is important to better constraint the origin of this physical phenomenon. Ferrario & Wickramasinghe (2007) suggest that magnetic fields in high field magnetic white dwarfs (HFMWDs) are linked to the magnetic fields of their progenitors. The hypothesis of the fossil origin of the magnetic field thus connects their properties from main-sequence stars to HFMWDs.

White dwarfs in close binaries often display optical variability such as eclipses, or the effects of reflection and irradiation on a low-mass companion. The detection of the orbital period of these binary systems is extremely important to constrain post-main sequence stellar evolution and in particular the most important process of Common Envelope interaction (Paczynski 1976; and Willems & Kolb 2004). In addition, detailed studies of systems orbital periods, masses and ages, can help us to better understand the physics of cataclysmic variable stars and Type Ia supernovae, possibly shedding light on physical phenomena such as angular momentum loss via gravitational wave versus magnetic braking radiation (King 1988; Parthasarathy et al. 2007). Moreover, a detailed analysis of the light-curve of any such system can help reveal the effects of tidal and rotational distortions as well as the irradiation and reflection due to mutual heating and radiative interaction of the binary components. The temperature changes and the reprocessed emitted light have the effect of raising the detected flux from the facing hemisphere of the secondary. The effects of

irradiation and in particular the detection of reflected light from low-mass companions is also important for the study of the secondary atmosphere (e.g. Peraiiah 1983).

In my thesis I mainly focused on the analysis of white dwarfs in the SuperWASP archive searching for signatures of their intrinsic and/or extrinsic variability. In particular I have explored the possibility of detecting low-mass, sub-stellar and planetary companions orbiting white dwarfs in the SuperWASP survey, by means of their transit signatures. Because white dwarfs are the end state of $\sim 97\%$ of stars in our galaxy they offer the unique possibility of investigating the fate of extra-solar planetary systems and their survival to the later stages of stellar evolution. In the following I will introduce the field explaining the motivations behind my work.

1.4.2 Sub-stellar companions to white dwarfs

Observationally, sub-stellar companions to white dwarfs are found to be rare ($< 0.5\%$ for L dwarfs, e.g. Farihi et al. 2005). Only two wide binary system GD165 (Becklin & Zuckerman, 1988) and PHL5038 (Steele et al., 2009), and two detached non-eclipsing, short-period white dwarf+brown dwarf systems are currently known, WD0137-349 (Maxted et al. 2006, orbital period ~ 116 min), and GD1400 (Burleigh et al. 2009 in preparation, orbital period ~ 10 hours). GD1400B and WD0137-349B are the only two sub-stellar companions known to have survived the common envelope (CE) phase of stellar evolution. During the CE phase the more massive component in the binary evolves into a red giant. If the initial orbital period is less than 10 years, the envelope of the giant will expand beyond the orbit of its compan-

ion. As a result the two components spiral towards each other, the CE is ejected leaving behind the progenitor remnant of the compact component with its companion at much smaller separations (see e.g. Paczynski 1976 and Iben & Livio 1993). WD0137-349B is the lowest mass object known ($\sim 50 M_{\text{JUP}}$) to have survived CE evolution. Although surveys such as the UK Infrared Deep Sky Survey (UKIDSS) and observatories such as the space infrared telescope (Spitzer) hope to reveal many more such binaries, they remain difficult to identify either as infra-red excesses or through radial velocity measurements. The detection of more such systems will allow us to place observational upper limits on the mass of sub-stellar companions that can survive CE evolution. For example, can Hot Jupiters survive their parent star's evolution to a white dwarf?

In addition the detection of a significant number of eclipsing white dwarf+brown dwarf (WD+BD) binary systems might help uncover the hypothesised population of 'old' cataclysmic variables (CVs) in which the current accretion rate is extremely low and the companion has been reduced to sub-stellar mass (e.g. Patterson 1998; Patterson et al. 2005; Littlefair et al. 2003). While these systems elude direct detection as X-ray sources and remain difficult to identify in optical and infra-red surveys, it is possible to measure the mass and the radius of the donor in eclipsing CVs. Indeed, Littlefair et al. (2006) finally confirmed the first such system through the system eclipses. Old CVs are important for shedding light on models of close binary evolution as well as for placing constraints on the period distribution of cataclysmic variables; in particular, the period gap and the period minimum (King 1988; Parthasarathy et al. 2007).

1.4.3 Can planets survive stellar evolution?

To date more than 350 extra-solar planets have been detected around nearby stars. Because the majority of stars with mass $< 8 M_{\odot}$ will evolve to white dwarfs it is natural to ask what will be the fate of these planetary systems. This question also has particular interest for us, in that the Earth's survival to the Sun's post-main sequence evolution is uncertain (Rasio et al. 1996; Duncan & Lissauer 1998; and Villaver & Livio 2007). Several theoretical studies discuss post-main sequence evolution of planetary systems and show that planetary survival is not beyond possibility (Duncan & Lissauer 1998; Debes & Sigurdsson 2002; Burleigh et al. 2002; and Villaver & Livio 2007). Observations indicate that planets in orbits beyond the extent of the RG and AGB radius, can survive stellar evolution (see Frink et al. 2002; Hatzes et al. 2005, Sato et al. 2003). More recently Silvotti et al. (2007) reported the detection of a $\sim 3 M_{\text{JUP}}$ planet orbiting an extreme horizontal branch star. Furthermore, Mullally et al. (2008) found convincing evidence of a $2 M_{\text{JUP}}$ planet in a 4.5 year orbit around a pulsating white dwarf. The latter, if confirmed, will be the first planet detected in orbit around a white dwarf, and will show that planets can indeed survive the death of their parent star.

Short-period planetary companions to white dwarfs may seem less likely. Only two scenarios can yield planets around a white dwarf in close orbits: 1) planets undergo CE evolution and survive the stellar evolution to a white dwarf, or 2) their orbits are significantly changed by a process occurring at the end of the AGB phase of stellar evolution. Villaver & Livio (2007) investigated the fate of a planet engulfed by the envelope of a red giant star and suggested that planets in orbit within the

reach of the red giant's envelope will either totally evaporate or in rare cases, more massive bodies can accrete mass and become a close companion to the star. Thus, only massive companions are likely to survive CE evolution. Villaver & Livio (2007) suggested that brown-dwarfs are more likely to survive the RGB and the AGB phases of stellar evolution. However, the estimate of the minimum planetary mass is uncertain and depend on several factors, such as the efficiency of the envelope ejection, which are largely unknown (Villaver & Livio 2007 and references therein).

Planets that escape the RGB and AGB engulfment and are sufficiently far from the stellar surface so that they do not experience tidal drag, will have their orbit increased to conserve angular momentum (as described by Jeans 1924). Duncan & Lissauer (1998) investigated the stability of planetary systems during post main-sequence evolution, and found that for WD progenitors experiencing substantial mass loss during AGB, planetary orbits become unstable on timescales of $\leq 10^8$ yr. Debes & Sigurdsson (2002) also studied the stability of planetary systems and found that mass loss from the central star is sufficient to destabilise systems of two or more planets. For unstable systems, in the case of orbit crossing, Debes & Sigurdsson (2002) found that the most likely result was that one planet would be scattered into an inner orbit, while the other would be boosted into a larger orbit or ejected from the system. This may result in white dwarf systems which have settled into a configuration with planets at orbital radii which were originally occupied by inner planets before the RGB phase of stellar evolution.

These results can provide an explanation for the recent detection of silicate-rich dust discs around a growing number of white dwarfs at orbital radii up to $\sim 1 R_{\odot}$ (e.g. Reach et al. 2005; Farihi et al. 2007, Farihi et al. 2008; Jura 2003). Jura (2003)

suggest that the formation of dust discs around white dwarfs is most probably due to the tidal disruption of an asteroid or a larger object in close orbit to the star. Dynamical instabilities during the final stages of solar system evolution could have caused the rocky body to migrate into inner orbits (as suggested by Debes & Sigurdsson 2002). If the body wanders too close to the Roche radius of the white dwarf it will be completely destroyed, producing a debris disc reminiscent of Saturn's rings (Jura, 2003). Recent studies of the dust disc around the white dwarf GD 362 (Jura et al. 2009) suggest that the more likely scenario which simultaneously explains all of GD 362's distinctive properties is that we are witnessing the consequences of the tidal destruction of a single body that was as massive as Mars.

The detection of any such close planetary-mass companion to WDs, will open an exciting chapter in the study of extra-solar planet evolution, constraining theoretical models of common envelope evolution and helping us to understand the ultimate fate of hot Jupiter systems as well as the fate of our own solar system in the post main-sequence phase.

1.5 Extra-solar planets: detection methods

The majority of the extra-solar planets have been detected by means of radial velocity measurements (Marcy et al. 2005). However, the first extra-solar planet ever found was detected around a millisecond pulsar, PSR1257 + 12, by means of variations in the arrival times of the star's pulsations (Wolszczan & Frail, 1992). In more recent years the transit technique has also yielded numerous planetary detections contributing importantly, to the discovery and the characterisation of extra-solar

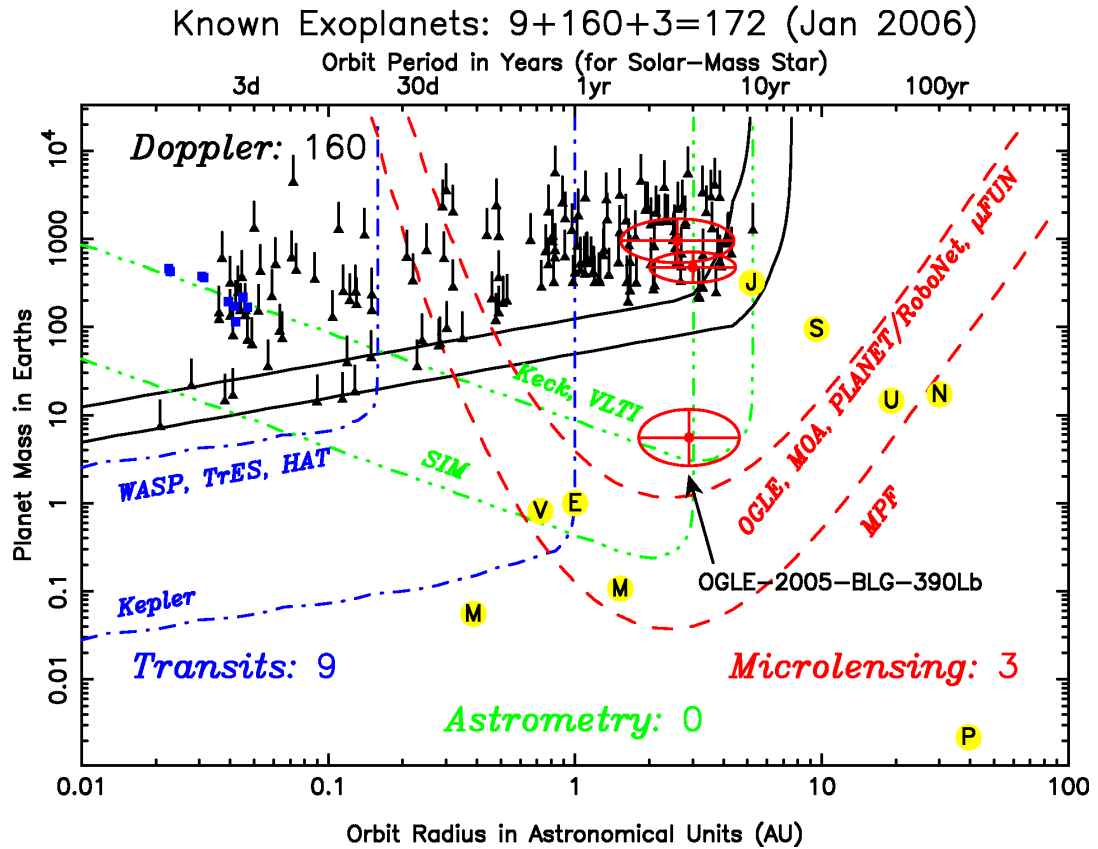


Figure 1.2: Figure from Horne (2006). Planets detection limits for different detection techniques: green astrometry; red microlensing; black radial velocity and blue transits. The Figure is referred to results on planet detection from 2006, however it clearly shows the different range of parameters covered by each individual detection technique.

planets (see e.g. Collier Cameron et al. 2006; Alonso et al. 2004; and Bakos et al. 2007 just to cite a few) together with the microlensing technique and the radial velocity method (see e.g. <http://exoplanet.eu/>, for a review on extra-solar planets). In the last few years extra-solar planets have also been discovered by means of direct imaging (see e.g. Marois et al. 2008 and references therein) and through astrometric measurements (Pravdo & Shaklan, 2009). Figure 1.2, from Horne (2006), shows the different detection limits for each of these techniques. The plot is referred to the number of extra-solar planets known by 2006. Nevertheless, the detection limits

indicated for the different detection methods are still valid. Ground-based transit searches are limited to Neptune-sized planets (Bakos et al. 2009) in orbit with periods of up to a few days. Space-based transit searches can detect smaller planets of sizes comparable to the Earth (also named Super-Earths) (blue dot-dashed line). Earth analogues might be detected from space missions such as Corot (Barge et al., 2005) and Kepler (Knutson & Charbonneau, 2009). Radial velocity searches are mostly sensitive to Jovian-like objects however recent results are pushing the mass of detectable planets to a few Earth masses (Mayor et al., 2009). In addition, the RV technique can explore longer orbital periods out to a few AU from the star (black line). Microlensing and astrometry cover the parameter space for medium to long orbital periods. The microlensing method is more sensitive to planets in Earth-to-Jupiter-like orbits with semi major axis in the range 1–5 AU (Beaulieu et al. 2006, Gaudi et al. 2008), but can detect planets even in wider orbits (red dot-dot-dashed line). The astrometric technique may be sensitive to terrestrial sized planets and the detection sensitivity increases with increasing semi-major axis distances. Thus astrometry can detect planets with long orbital periods (green-dashed lines). For an updated status on the number and characteristics of known extra-solar planets I refer the reader to the extra-solar planet encyclopedia at <http://exoplanet.eu/>.

This PhD thesis focuses on the use of the transit method for the detection of extra-solar planets; in particular the detection of transit signatures of sub-stellar and planetary companions to white dwarf stars. In the following I describe in detail the characteristics of the transit detection technique. I also briefly discuss other detection methods.

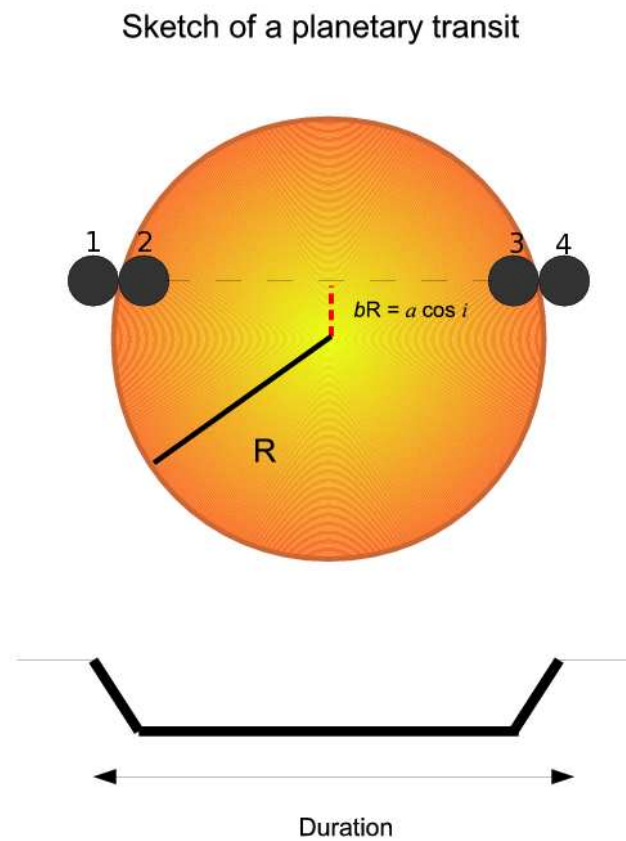


Figure 1.3: Description of a transit event. The cartoon also shows the different phases of the transit event: the ingress (points 1–2), the flat bottom (points 2–3), and the egress (points 3–4).

1.5.1 The transit method

A transit is a temporary dimming of the apparent brightness of a star that occurs when a planet crosses the stellar disc. The transit appears periodically with a period equal to the orbital period of the planet. Because planets are cooler than their parent star they cause a dip in the stellar light-curve whenever they transit the star. A sketch of a transit light-curve is shown in Figure 1.3. Points 1–2 and 3–4 illustrate the transit ingress and egress; points 2-3 the central part, flat bottom, of the transit. Also indicated are the star radius R_\star and the impact parameter b . The fractional change in the star brightness, $\Delta F/F$, is proportional to the fraction of the stellar surface subtended by the planetary disc; therefore photometric measurements directly yield a measure of the planet size. The detection of transiting planets require an almost perfect alignment between the observer, the planet and the star. This is defined by the transit (geometric) probability P_{tr} . When a planet of radius R_{pl} orbits a star of mass M_\star and radius R_\star at an orbital distance a the transit of the stellar disc will be visible only if the system inclination angle i satisfies the following condition (Charbonneau et al., 2007):

$$a \cos i \leq R_\star + R_{pl} . \quad (1.3)$$

This is illustrated in Figure 1.4 where a is the orbital distance and $d(t)$ is the planet-star distance. If we assume that $\cos i$ can take any value between 0 and 1, then the probability that the inclination satisfies the geometric criterion is:

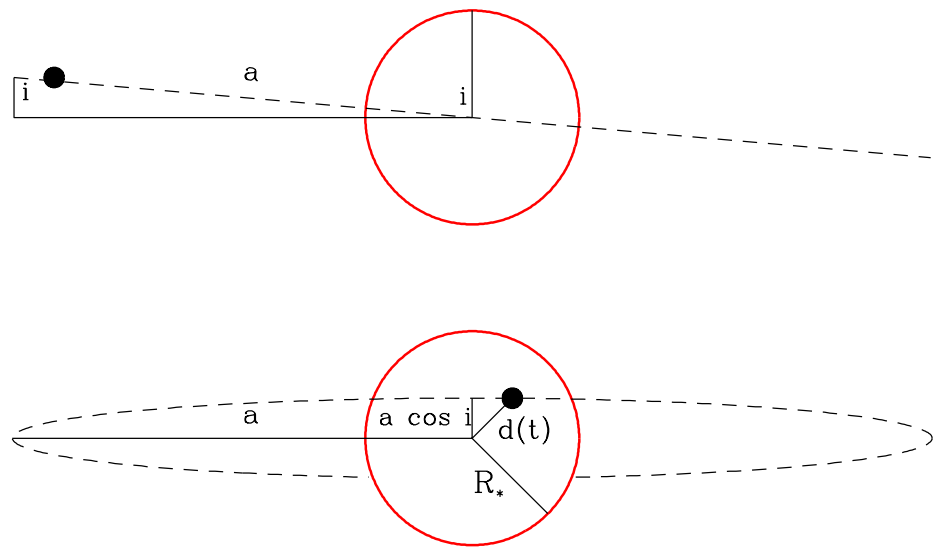


Figure 1.4: Geometry of a transit event of inclination i and orbital radius a as seen from the side (top-panel), and from the observer's vantage point (lower-panel).

$$P_{tr} = \frac{\int_0^{(R_\star + R_{pl})/a} d(\cos i)}{\int_0^1 d(\cos i)} = \frac{R_\star + R_{pl}}{a}. \quad (1.4)$$

Geometrically speaking the transit method favours planets in systems with small orbital radii. If I consider the simple case of a circular orbit ($i = 90^\circ$) then the transit duration D_{tr} , the fraction of the orbital period P during which the planet is transiting the host star (Figure 1.5), can be written as follows (Seager & Mallén-Ornelas, 2003):

$$D_{tr} = 2(R_{pl} + R_\star) \sqrt{\frac{a}{GM_{tot}}} \quad (1.5)$$

where M_{tot} is equivalent to $M_{pl} + M_\star$, and G is the constant of gravitation. Figure 1.5 shows the occurrence of a transit event for a transit of a generic inclination angle i .

The depth of the transit signature is a measure of the fractional change in the star brightness and is related to the star and planet radii as follows (Seager & Mallén-Ornelas, 2003):

$$\Delta F = \frac{F_{out} - F_{in}}{F_{out}} = \left(\frac{R_{pl}}{R_\star}\right)^2 \quad (1.6)$$

where F_{out} is the observed stellar flux out of transit, and F_{in} is the stellar flux during transit. Here for simplicity I do not consider the effects of limb darkening. However, the shape of the transit dip depends on the degree of limb darkening in the observational band, as well as on the inclination angle and on the ratio of the planet to stellar size. Transiting planets also offer the unique possibility of directly detecting

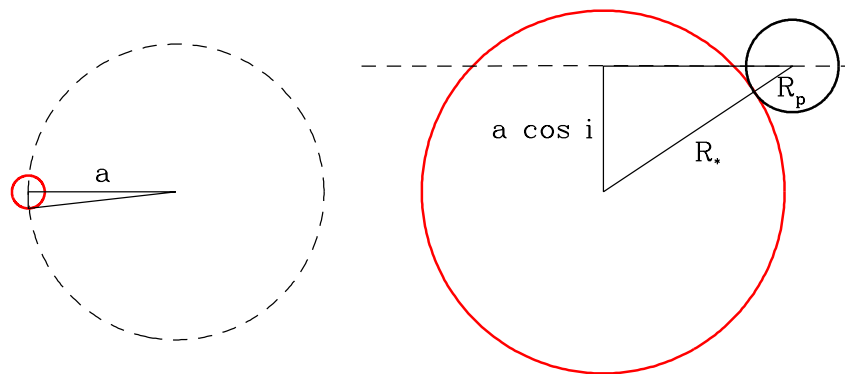


Figure 1.5: The fraction of the planetary orbit spent during transit, (left-sketch), and the geometric alignment condition for a transit as seen from the observer's point of view (right-sketch).

the light coming from the planet itself during the secondary eclipse (Deming et al. 2007, and Agol et al. 2009). This allows observers to obtain crucial information on the characteristics and the chemical composition of the planet's atmosphere (Tinetti et al., 2007), important for the detection of life signatures (Arnold et al., 2002).

1.5.2 Radial Velocity

Radial velocity (RV) is probably the most famous planet detection technique. The radial-velocity method uses the motion of the star induced by the gravitational interaction of the planetary body. The method consists of measuring the variations in the speed with which the star moves toward or away from Earth. The radial velocity can be deduced from the displacement in the parent star's spectral lines due to the Doppler effect and can be measured using high resolution spectroscopic measurements. The semi-amplitude of the radial velocity of the host star induced by small terrestrial planets is of the order of few centimetres per second. Currently the most accurate RV instrument for planet searches is the HARPS spectrograph (Mayor et al., 2003) which is able to achieve a long-term precision of better than 1ms^{-1} .

The radial velocity technique can only measure the projected radial velocity i.e. the component of the velocity in the direction of the line of sight. Thus, it only allows to estimate a projected minimum mass of $M_{pl} \sin i$ for the planetary companion. From the measure of the RV semi-amplitude, K_* , the projected mass of the planetary

companion can be derived as follows (Santos 2008):

$$K_{\star} = \frac{2\pi a}{P} \frac{M_{pl} \sin i}{M_{\star}} \quad (1.7)$$

where P is the orbital period of the planet, a is the semi-major axis of the orbit, M_{pl} is the planetary mass and M_{\star} is the mass of the star. The unambiguous determination of the planetary mass is possible when a combined value of the orbital inclination is obtained by the transit method. Thus the RV and the transit techniques are mutually dependent as spectroscopic follow-up of transiting systems is needed in order to confirm their planetary nature.

1.5.3 Timing, astrometry, microlensing and imaging

In addition to the RV method and the transit technique other planet detection methods exist and planets have also been detected by means of timing analysis, microlensing, astrometry and imaging.

The *timing* technique was firstly used by Wolszczan & Frail (1992) to detect the first ever extra-solar planet companion to the millisecond pulsar PSR1257 + 12 Wolszczan & Frail 1992. A pulsar is a neutron star: the small, ultradense remnant of a star that has exploded as a supernova. Because Pulsars emit radio waves extremely regularly as they rotate, slight anomalies in the arrival time of the observed radio pulses can be used to track the pulsar's motion. This is a powerful technique which has also been used to search for planetary companions to white dwarfs. Mullally et al. (2008) found convincing evidence for a $2 M_{JUP}$ planet in a 4.5 year orbit around a pulsating white dwarf.

More generally, if a planet is in orbit around a star the star's distance from the Sun will periodically change as it orbits the centre of mass of the system. If the star is a stable pulsator (pulsars are among the most stable pulsators known, Matsakis et al. 1997), this will cause periodic changes on the pulse arrival time. Because the pulse arrival time is proportional to the semi-major axis of the orbit the timing sensitivity increases with the orbital separation, making long period planets easier to detect (as for astrometry).

The *microlensing* technique is sensitive down to $1 R_{\odot}$. This method involves detecting the light coming from a distant background star that is magnified by the gravitational field of a foreground star. The method allows the detection of planets and stars regardless of the light they emit. Generally planets can only be detected around bright stars. Because microlensing boosts the light by several magnitudes, it allows the study of the objects that emit little or no light. Lensing events are brief, lasting for weeks or days, as the two stars and Earth are all moving relative to each other. Since the event requires a highly improbable alignment, a very large number of distant stars must be continuously monitored in order to detect planets via microlensing. This method is most fruitful for planets between Earth and the centre of the galaxy, as the galactic centre provides a large number of background stars. The application of the microlensing technique to the detection of extra-solar planets was firstly suggested by Paczynski (1991). The first detection dates back to 2002 by Udalski et al. (2002) who announced the detection of several possible planets, though limitations in the observations prevented clear confirmation. Since then, seven confirmed extrasolar planets have been detected using microlensing (see for examples Dong et al. 2009, Bennett et al. 2008, Pont et al. 2008). A notable disadvantage of the method is that the microlensing event cannot be repeated because

the chance alignment never occurs again. Also, the detected planets will tend to be several kilo parsecs away, so follow-up observations with other methods are usually difficult if not impossible.

The *Astrometry* method for planet detection consists of precisely measuring a star's position in the sky and observing how that position changes over time. If the star has a planet, then the gravitational influence of the planet will cause the star itself to move in a tiny circular or elliptical orbit. Effectively, star and planet orbit around their mutual centre of mass. Unfortunately, the changes in stellar position are so small (μ asec) and atmospheric and systematic distortions so large that ground-based detection of planets is difficult. However, the Hubble Space Telescope did succeed in using astrometry to characterise a previously discovered planet around the star Gliese 876 (Benedict et al. 2002). One potential advantage of the astrometric method is that it is most sensitive to planets with large orbits. This makes it complementary to other methods that are most sensitive to planets with small orbits. However, very long observation baselines will be required (years), and possibly decades to allow detection via astrometry. However, the first planet detected via astrometry was finally announced in 2009. Pravdo & Shaklan (2009) detected the planet VB 10b with mass of $7 M_{\text{JUP}}$ orbiting a low-mass red dwarf star by means of astrometric measurements. If confirmed, this will be the first extra-solar planet discovered by the astrometry technique.

Imaging. Because planets are extremely faint sources the direct light coming from them is generally lost in the glare of their parent stars. Thus, it is very difficult to directly detect a planet. In certain cases, however, current telescopes may be capable of directly imaging planets. Projects for the search of extra-planets employing new observing instruments are underway at the Gemini telescope (GPI, Gemini

Planet Imager, Graham et al. 2007), the VLT (SPHERE, Spectro–Polarimetric High–contrast Exoplanet Research, Mouillet et al. 2009), and the Subaru telescope (HiCIAO, High contrast Coronagraphic Imager with Adaptive Optics, Tamura et al. 2006). The direct imaging planet detection method naturally favours the detection of large planetary objects (considerably larger than Jupiter) in distant orbits from their parent star, and young bright objects so that their infrared radiation is easily detectable. In July 2004, the first planetary companion was announced around a brown dwarf star via direct imaging by Chauvin et al. (2004) and subsequently in 2005 Chauvin et al. (2005) confirmed the planetary nature of the companion which was found to have an orbital period of ~ 40 AU and a mass of $\sim 5 M_{\text{JUP}}$. More recently, in 2008 the detection of the first multiple planet system has been announced. Three planets were directly observed orbiting the star HR 8799, whose masses are approximately 10, 10 and 7 M_{JUP} (Marois et al. 2008). At the same time it was also announced that the Hubble Space Telescope directly observed an exoplanet orbiting Fomalhaut with a mass $\sim 3 M_{\text{JUP}}$ (Kalas et al. 2009).

While there are numerous direct and indirect planetary detection methods currently employed, the work presented in this thesis focuses on the transit technique for the search of sub-stellar and planetary companions to white dwarfs in the SuperWASP survey.

The work is set out as follows; in Chapter 2 I describe the SuperWASP project, the SuperWASP instrumentation, the survey designs and the scientific goals. In Chapter 3 I present simulations of transiting sub-stellar and terrestrial companions to white dwarfs and the characteristics of their transit light-curves. In Chapter

4 I search for eclipses and transit signals in a sample of 194 white dwarfs in the SuperWASP archive and I estimate an upper limit to the frequency of planetary companions to white dwarfs. In Chapter 5 I study the sample of 194 white dwarfs to search for extrinsic and intrinsic photometric variability due to white dwarf non-radial pulsations, star spots in magnetic white dwarfs, irradiation and reflection effects in binary systems with white dwarf primaries. Finally, in Chapter 6 I present my conclusions and my project for future work.

Chapter 2

The SuperWASP project

Abstract

SuperWASP (Wide Angle Search for Planets) is the world's leading project for the detection of transiting extra-solar planets. It comprises a consortium of eight institutions which include Leicester University, St. Andrews University, Queens University Belfast, the University of Cambridge, the University of Keele, the Open University, the Isaac Newton Group (ING) and the Instituto de Astrofísica de Canarias. The SuperWASP project is a ground-based ultra-wide-field photometric survey which consists of two robotic telescopes, SuperWASP-North (La Palma, Canary Islands, Spain), and SuperWASP-South (Sutherland, South Africa). Each instrument is capable of observing the entire sky every 40 minutes, and can achieve a photometric accuracy of better than 1% for stars in the range $8 < V < 12$. SuperWASP science goals are designed to explore long baseline (months-years) time domain astronomy, and in particular the detection of transiting extra-solar planets. Indeed SuperWASP

has discovered 24 extra-solar planets in the last two years (2006-2008) and is currently the most successful planet transit discovery mission of its type.

2.1 Introduction

In the last decade the field of extra-solar planets has witnessed a rapid increase in the number of newly detected systems, totalling ~ 353 planets at the time of writing (<http://exoplanet.eu/>). The majority of these systems have been detected via radial velocity (RV) measurements. However, in the last few years ground-based transit surveys and in particular the SuperWASP project, have contributed with many discoveries. When combined with RV measurements planetary detection via the transit technique offers the possibility to determine unambiguously the planetary mass and radius as the system's inclination angle is known. Photometric transit searches are strongly biased towards planets in small orbits, since they have a greater probability of presenting a transit configuration. Transit surveys also require a minimum number ($\sim 3,5$) of distinct eclipses to be observed in order to confirm the planetary detection. Since longer period systems give fewer opportunities for transits to be observed, this drastically reduces their detection probability in particular in the case of transit surveys with a limited baseline. Finally, ground-based transit surveys are biased in favour of larger planets or smaller stars, both making the transit depth $\delta = (R_{pl}/R_{\star})^2$ larger, and thus producing a deeper transit signal. These close-in planets are known as Hot Jupiters (HJ) and Very Hot Jupiters (VHJ), they have orbital periods of less than a few days (at orbits 50-100 times closer than Jupiter is to the Sun), and show transit signals of $\sim 1\%$ depth with durations between 2 to 3 hours. Transiting planets offer a unique opportunity to study the diver-

sity of planetary atmospheres (Brown 2001), and also provide an important testing ground for models of these atmospheres. Through the detection of secondary transits (i.e. when the planet goes behind its parent star) it is possible to characterise the light emitted by the day sides of these planets, and to construct a model spectrum (e.g. Charbonneau 2008; Deming et al. 2005; Grillmair et al. 2007; Knutson 2008). In addition, a detailed analysis of transit light-curves can reveal transit time and transit duration variations which can indicate the presence of secondary small bodies, exo-moons, otherwise undetectable in the system (Kipping 2008; Szabó et al. 2006; Simon et al. 2007).

Radial velocity surveys have shown that around 6% of the population of nearby solar-type stars harbour Jupiter-sized planets in orbits out to 3 AU. Less than 20% of these are HJ and VHJ planets. By definition, transiting planets have an almost perfect alignment between the observers line of sight, the planet and the host star. The probability that a Hot Jupiter, with a randomly inclined orbit, will transit its parent star is about 10% (Horne 2003). We might therefore expect to find roughly 1 in every 1000 stars ($6\% \times 20\% \times 10\%$) in a random SuperWASP field to exhibit a transit. Since the transit method clearly favours large planets orbiting their parent stars at small orbital radii, a large sample of stars must be monitored in order to detect statistically meaningful numbers of transiting planets. The SuperWASP observing strategy is designed to obtain well sampled light-curves of numerous stars with a photometric precision of better than 1%, required for the detection of planets. SuperWASP routinely observe fields of high stellar densities while avoiding crowded fields near the Galactic plane. This choice allows us to reduce the number of blended stars and stellar systems with eclipse depths, durations, and orbital periods resembling those of planets (see e.g. Brown 2003 for more details). The SuperWASP

observing strategy facilitates the selection of planetary candidates and minimises the loss in telescope time (and observers' time) spent ruling out impostors. SuperWASP employs off-the-shelf, small aperture, wide-field imaging systems which consist of a large CCD mounted directly onto a high-quality wide-angle camera optic. Each camera has a field of view of 7.8^2 degrees and continuously photographs the sky capturing up to 100,000 stars per image. This large number is needed to observe a sufficient number of bright stars ($8 < V < 12$) for which we have good quality photometry ($< 1\%$). This amounts to over 50 gigabytes of observational data per night, per observatory, which is automatically processed by our custom built pipeline. Finally, all data are stored in a data base hosted by the University of Leicester.

To date about 52 extra-solar planets have been found using the transit technique. Among those, 24 have been discovered by SuperWASP making SuperWASP the most successful project for discovering extra-solar transiting planets. In this chapter I will describe in detail the SuperWASP project and data. I will provide technical information on the two SuperWASP telescopes, the optics employed, the data acquisition system and data analysis software. Finally, I will describe the SuperWASP observing strategy and show a few examples of SuperWASP planet discoveries.

2.2 Instrumentation

The SuperWASP project is the direct successor of the Wide Angle Search for Planets prototype WASP0 project (Kane et al. 2004). The WASP0 prototype was designed to demonstrate the feasibility and efficacy of using inexpensive wide-angle camera optics in the detection of transiting planets. A detailed description of the

SuperWASP prototype WASP0 and the results obtained during the observational campaigns can be found in (Kane et al. 2004, 2005).

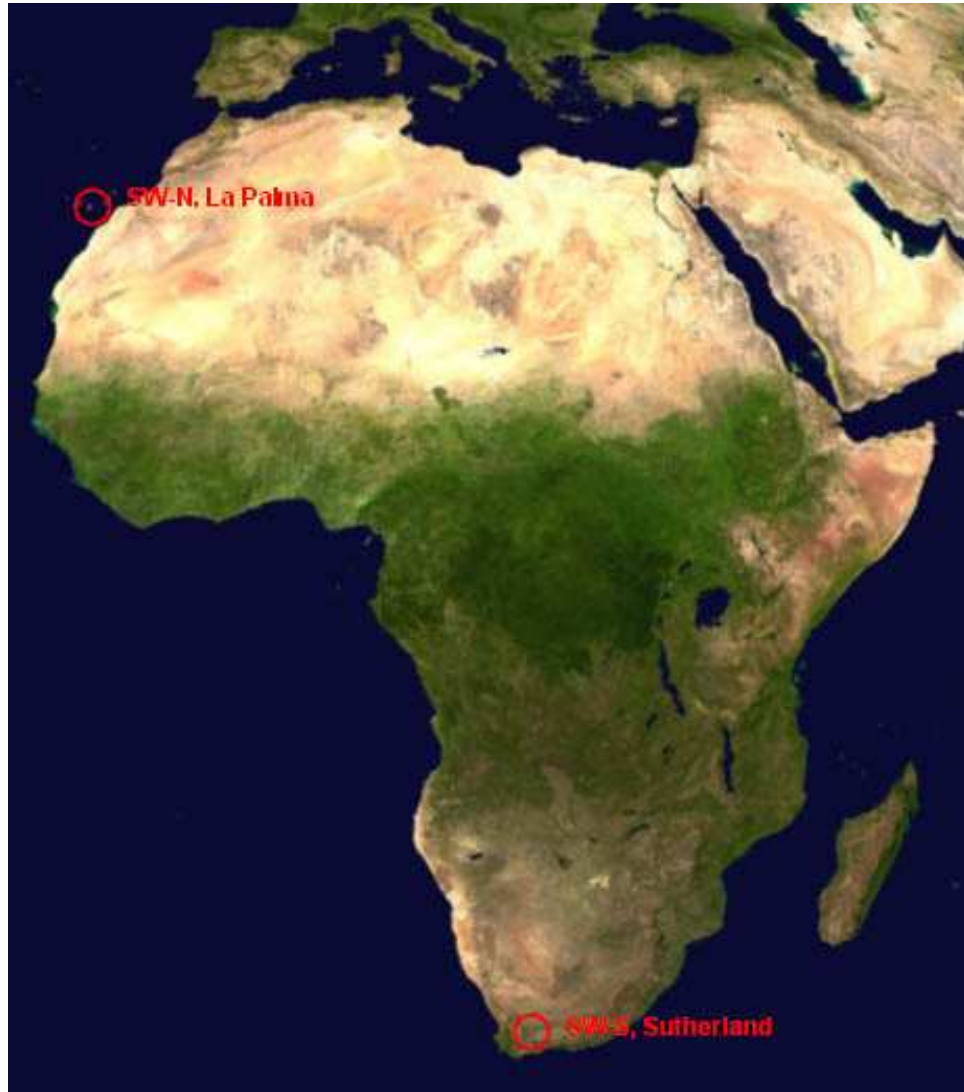


Figure 2.1: Location of SuperWASP-North and SuperWASP-South telescopes.



Figure 2.2: SuperWASP-North telescope at Roches de los Muchachos observatory on the island of La Palma.

2.2.1 SuperWASP telescopes

The SuperWASP project comprises two completely robotic telescopes

SuperWASP-North (SWN), situated among the Isaac Newton Group (ING) of tele-

scopes in La Palma, Canary islands, Spain and SuperWASP-South (SWS) in Sutherland, South Africa at the South African Astronomical Observatory (SAAO) site, (see e.g. Figure 2.1). SuperWASP first began operating in the northern hemisphere in 2004 with a complement of five cameras, observing in white light with the spectral transmission defined by the optics, detectors, and atmosphere. The SWN telescope has been subsequently up-graded to operate with eight cameras (see Figure 2.2). From 2006 SWS became operational, mounting eight cameras and using a broadband filter which define a pass-band from 400 to 700 nm, also introduced in SWN from 2006 (see also Figure 2.3). The broadband filter was introduced to remove red-light leakage thus increasing the contrast between the sky background and the objects. Figure 2.3 shows the transmission feature of the Earth atmosphere which becomes important at wavelengths > 700 nm. Both SuperWASP instruments use an equatorial fork mount, housed in a small enclosure. Each mount has been constructed by Optical Mechanics, Inc. (Iowa; formerly Torus Engineering), and have a pointing accuracy of $30''$ rms over the whole sky with a tracking accuracy of about $0''.01 s^{-1}$. The enclosure employs a roll-off roof which is better suited to the rapid rotation of the mount. The system completely retracts in less than 20 seconds and takes ~ 54 seconds to completely close. The space under the roof is used as a control and computer room and is temperature-controlled. More details can be found in Pollacco et al. (2006). Each telescope uses e2V CCD cameras manufactured by Andor Technology (Belfast, UK). The e2v CCDs consist of 2048×2048 pixels of $13.5 \mu\text{m}$. The CCDs are cooled to -50 deg degrees Celsius which is sufficient for the performance needed by SuperWASP. Figure 2.3 shows the pass-band of SuperWASP filter (nm) plotted alongside the CCDs response, the atmospheric transmission and the lens transmission.

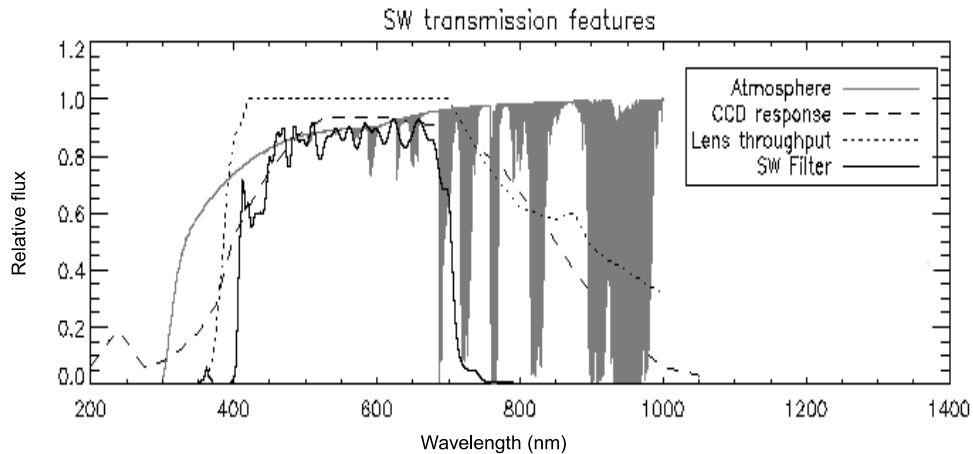


Figure 2.3: the pass-band of the SuperWASP filter (nm) plotted alongside the CCD response, the atmospheric transmission and the lens. transmission

More details of the CCDs and their performance can be found at <http://www.andor.com/>. The SuperWASP cameras use Canon 200mm f/1.8, telephoto lenses. These lenses together with the above detectors give a field of view of 7.8×7.8 degrees squared and an angular scale of $13''.7 \text{ pixel}^{-1}$.

2.2.2 Data acquisition system

We use a Data Acquisition System (DAS) PC with storage discs for each detector. The acquisition cluster deals with the high rate of data arising every night from the eight cameras of each telescope. The observations are scheduled by a TCS (telescope control system) which also controls other observing functions such as

telescope pointing and roof control. In addition the TCS is connected to a weather station and a GPS receiver which ensure that the absolute time is accurate to better than 1s. The TCS continuously monitors the systems to ensure operations run smoothly. In case of a break in communications, a close-down procedure will start abruptly. Every night the data are stored locally on DAS machines. At the end of an observing run, the data from SWN are compressed and sent back to UK via the Internet, while for SWS, due to the slower connection speed, data are copied onto a magnetic tape. Both telescope locations have a local weather station which measures the internal and external temperature and humidity, the wind direction and strength, precipitation and air pressure. A cloud sensor (infra-red activated) is also used (see the website <http://wasp.astro.keele.ac.uk/live/>).

2.2.3 Data acquisition software

The data acquisition software is high-level software which controls the entire SuperWASP system. The software is a modified version of Linux software Talon produced by Optical Mechanics, Inc. Object acquisition and tracking, scheduled operations, environmental monitoring, dome control, image analysis and processing all fall under the control of the acquisition software. Observations are possible using a standard graphical interface or a command-line interface. Talon supports two operational modes: manual control by an observer, using the graphical interface or the command line interface; and an automated observing mode. The Talon operation scheduling program takes control of the telescope and performs observations from a predefined queue (*waspsched*). The first SuperWASP observing season in 2004 was operated via the manual mode control and the observer was responsible for

taking bias and dark frames, opening and closing the dome and taking flat fields at twilight. Starting from 2005 a dynamic scheduler *waspsched* has been developed for all observations. *Waspsched* has controlled continuous operations thereby increasing the system observational efficiency. In addition, observations of all-sky fields can be easily intermixed with planetary fields, offering the possibility to support alternative observing modes, and in particular, the ability to interrupt the scheduled observations to follow up transient events (e.g. gamma-ray bursts, supernovae, comets etc.). The weather conditions from the two local weather stations are fed into the software enabling a weather alerts for different weather conditions (e.g. high humidity or strong wind). In the case of an alert, the system parks the telescope in a predefined position to avoid collisions with the closing roof. If the roof fails to close, a radio signal is sent to a receiver in the dome of the nearest observer-operated telescope.

2.2.4 SuperWASP pipeline

To deal with the large amount of data, a custom built pipeline for data reduction has been developed by the SuperWASP consortium. The pipeline uses custom written programs, shell scripts and several STARLINK packages. The pipeline corrects each science exposure using bias frames, thermal dark-current exposures, and twilight-sky flat-field exposures. An astrometric solution is computed for each field using the USNO-B1.0 catalogue (Monet et al., 2003) and Tycho-2 (Hog et al., 2000) catalogue as photometric input catalogues. Aperture photometry is performed in three circular apertures of radius 2.5, 3.5 and 4.5 pixels ($\simeq 35''$, $48''$ and $62''$) selected by inspection of images of known blended and unblended objects at these spatial resolutions.

The sky background is computed in an annulus with inner radius of 13 pixels and outer radius 17 pixels, 10 times the area of the 3.5 pixel aperture. We use the fractional variation in flux between the three different apertures to identify blended sources from unblended ones. We use the wing-to-core flux relative change defined as: $r_1 = (f_3 - f_1)/f_1$ and $r_2 = (f_3 - f_2)/f_2$, where f_1 , f_2 , f_3 are the fluxes in the three apertures defined above. For unblended images, r_1 and r_2 are related by a constant scaling factor. Finally the pipeline creates an input catalogue file. Each object is labelled with the airmass and catalogue magnitude, and is corrected to heliocentric Julian date. These, plus information on the sky background, aperture radius, raw instrumental fluxes and their associated variances, and blending information are saved in a FITS binary table. More details and information on the pipeline can be found in Pollacco et al. (2006).

The FITS binary tables produced by the pipeline are read into the post-pipeline calibration module for reduction from raw to calibrated magnitudes. The pipeline is designed to calibrate and remove photometric trends due to primary and secondary extinction, the system zero point and the system response to colour changes. The final corrected fluxes are added to the FITS table ready to be ingested into the archive.

2.2.5 Data archive

The SuperWASP data archive held at Leicester University consists of two similar catalogues, a private catalogue used by all members of the consortium and a public catalogue which will soon become available. The latter will be populated using

data from the private catalogue at defined delayed time intervals (time scale yet to be decided). The major advantage of the SuperWASP archive is its flexibility, allowing the consortium to add extra attributes (for example, periods for variable stars) as the archive gets populated with more and more data. The results from the preprocessing of large volumes of data, for example when detecting planetary transits or detecting periodicities, can be fed-back into the catalogue, by appending the information to existing objects and creating new entries as needed. Additional tables are then created and made available for the user to use in the formulation of queries. Queries can be made via an intermediate query language WQL (custom written by Dr. Richard West). WQL is a structured query language which allows us to express queries as simple ASCII text files in which the user can describe a variety of parameters and filters to be applied to and retrieved from the catalogue. Queries can include parameters such as object ID, position, brightness and variability, and can use constraints on for example the number of seasons, photometric points, the right ascension and declination, to name but a few. The query files are used in conjunction with a command-line tool, *wcatquery*, which deals with all the details of communicating with the catalogue query server. Queries can be performed on a per object basis as well as in batch mode. Other command tools to access the archive are the *wlextract* and *wimgextract* which allow users to extract respectively one or more SuperWASP light-curve FITS files, and retrieve the raw images. All the archive structure and its updating as well as the specific formulation of the intermediate query language WQL and all the related software was designed and implemented by Dr. Richard West.

In parallel to the above interface, a separate custom written interface to the archive has been developed by Dr. David Wilson (Wilson, 2007). The Variable Star In-

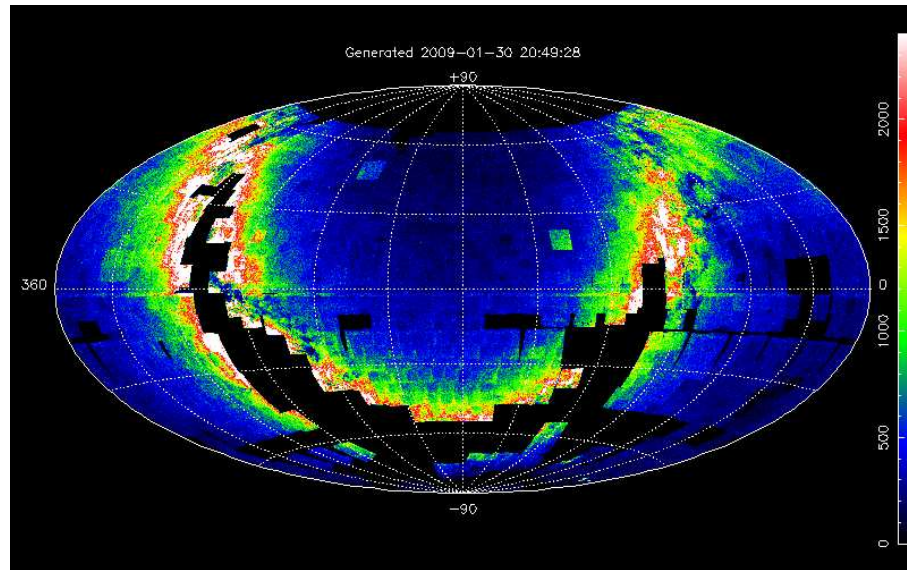


Figure 2.4: illustrates the number of observed stars per field. Black frames are region in the sky not covered by SuperWASP (for example the galactic plane). The more densely sampled SuperWASP fields contain up to ~ 300000 stars.

investigator (VSI) is a web based Virtual Observatory tool that combines parameters from an object's light-curve with external catalogue data. The returned data which includes SuperWASP light-curves and statistics, image thumbnails, as well as blending information and much more, are extremely useful particularly in the analysis of SuperWASP planet candidates. The VSI web-pages enable quick elimination of unlikely stellar hosts such as giants, known multiples or blended systems. The VSI interface is extensively used by the consortium in the identification of candidates for follow-up. More details can be found in Wilson (2007).

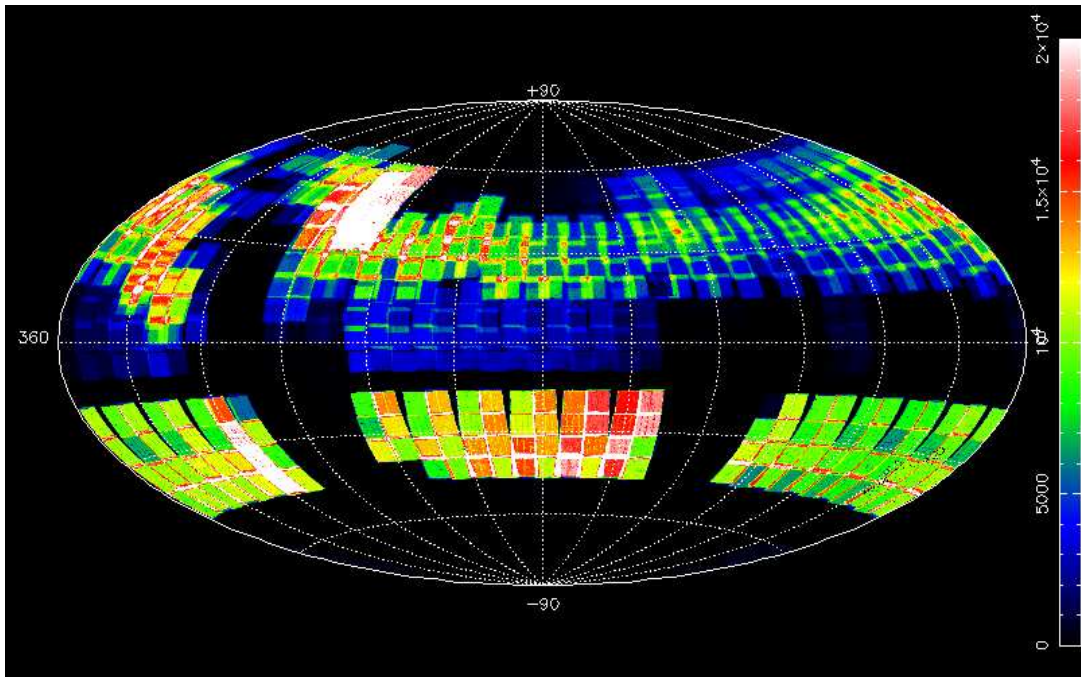


Figure 2.5: shows the average number of photometric points per star. As in Figure 2.4 black frames are regions in the sky not observed by SuperWASP. The maximum number of points per star is $\sim 2 \times 10^4$ (white coloured frames).

2.3 SuperWASP observing strategy

SuperWASP's main science goal is the detection of extra-solar planets via the transit method. As mentioned before we know from radial velocity surveys that $\sim 6\%$ of FGK stars harbour planets within 0.3 AU. Of these stars $\sim 1.2\%$ have HJ and VHJ orbiting at less than 0.1 AU (Lineweaver & Grether 2003; Marcy et al. 2005). Of these, only 10 % will transit their parent star, so we can expect about 1 in every 1000 stars to harbour a transiting planet. Therefore the SuperWASP survey needs to observe a large number of stars, with the required photometric precision ($< 1\%$), in order to detect transit signals. Some of the transit surveys (e.g. STARE and Vulcan, e.g. Brown & Charbonneau 2000; Borucki et al. 2001) have searched for

planets focusing on highly populated fields near the Galactic plane. Despite the high stellar density in such fields, the large population of early-type main sequence and giant stars only worsens the problem of stellar blending. In addition, these stars do not contribute to the detection statistics, since transit amplitude is inversely proportional to the stellar radius, making planetary companions difficult to detect. For this reason the SuperWASP observing strategy focuses on fields of high stellar densities (selected using the Besancon Galactic model, <http://www.obs-besancon.fr/model/>) but avoiding the Galactic plane where crowded fields would make reduction and detection difficult. Every clear night, SuperWASP instruments cyclically raster the sky in a series of fields centred on the Local Sidereal Time (LST), spaced by 1 hour in right ascension. A maximum of eight fields are observed at any one time, each with a duration of ~ 1 minute (including 30 seconds exposure plus the telescope slew and settling time). This observing strategy provides well-sampled light-curves with baseline of ~ 8 – 10 minutes. A typical field contains approximately 30,000 stars per camera at magnitudes brighter than $V \sim 13$. Figures 2.4 and 2.5 show the SuperWASP sky coverage. Figure 2.4 shows the star counts over the observed fields and Figure 2.5 shows the average number of points per star. The SuperWASP observing strategy enables us to obtain fields of high star density while reducing the frequency of planetary impostors. However, the planetary candidate sample is unavoidably contaminated by stellar systems that mimic transit events, for example: grazing transits in systems of two main-sequence stars, or transits of giants by main-sequence stars (see e.g. Brown 2003 for a detailed discussion). For this reason an additional photometric and spectroscopic follow-up is needed to confirm the planetary nature of the target system.

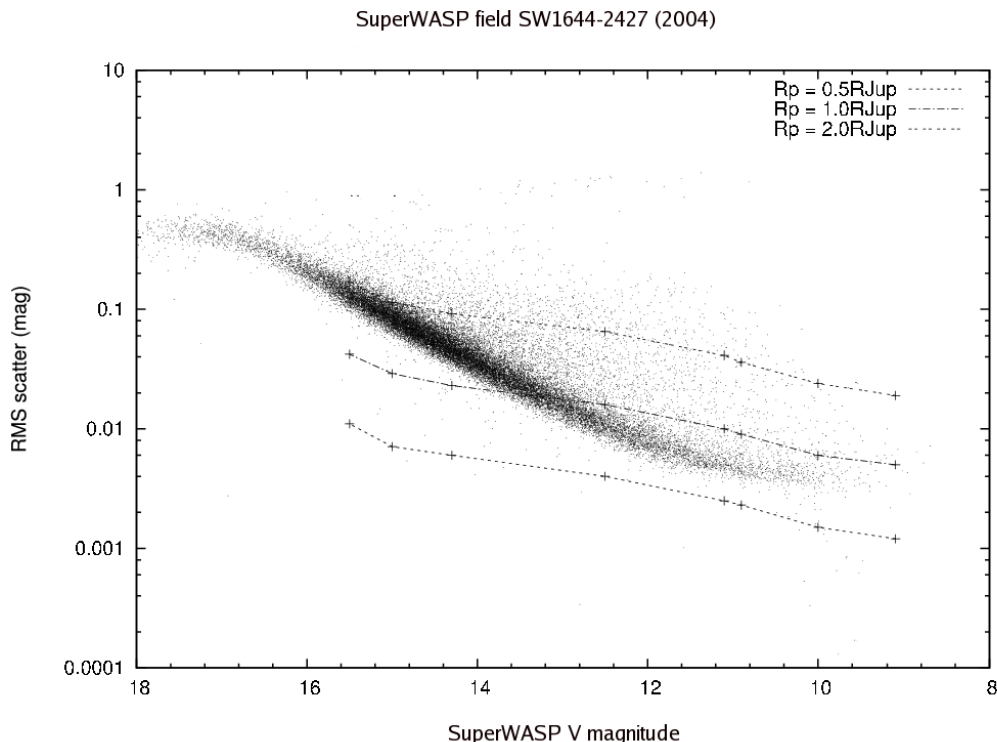


Figure 2.6: RMS plotted versus SuperWASP instrumental magnitude. Also indicated is the photometric accuracy needed for the detection of $0.5 R_{\text{JUP}}$ (dotted line), $1 R_{\text{JUP}}$ (dot-dashed line) and $2 R_{\text{JUP}}$ (dashed line) planets.

2.4 SuperWASP data

The SuperWASP observing strategy typically yields light-curves which span about 120–150 day per object per season, with seasons spanning from 2004 to 2008 in the case of SWN and 2006 to 2008 for SWS. Each light-curve is well sampled with ~ 50 – 60 photometric points per observing night, which corresponds to a total of 3000–5000 photometric points per light-curve per season, depending on the amount of time lost due to bad weather conditions. For targets in the magnitude range $8 < V < 12$, SuperWASP can achieve a photometric accuracy of better than 1%. This value becomes larger for increasingly fainter objects. Figure 2.6 shows the

root mean square *rms* values of SuperWASP light-curves against the instrumental magnitudes. Figure 2.6 illustrates the precision achievable with SuperWASP data. It also shows that stars brighter than $V \sim 12$ can be measured to a precision of few millimagnitudes. SuperWASP magnitude is calculated from the mean flux (μ Vega) using the following formula:

$$V = -2.5 \text{Log}_{10} \overline{F} + 15 \quad (2.1)$$

where \overline{F} is the mean flux of the target object.

Because SuperWASP is a wide-field long-term photometric survey, SuperWASP data will inevitably contain systematic errors which depend on correlated and uncorrelated noise sources that vary either on short timescales (intra-night), and/or on long timescales, across the observing season. Pont et al. (2006) showed that errors on ground-based millimagnitude photometry are correlated. These trends have a low-frequency component which introduces covariance between photometric points in the light-curve. The typical correlation has a time-scale of 2 to 3 hours, similar to planetary transit durations. This so called ‘red-noise’ acts to reduce significantly the effective signal-to-noise of the transit event. In such case the required signal-to-noise threshold for planetary detection is about three times higher than in the case of white Gaussian noise (see Figure 4 of Pont et al. 2006), and may render some planets undetectable. This low-frequency noise component has been observed in a wide variety of phenomena such as Biology, Geophysics, Astronomy, Economics, as well as in Psychology and music, to mention a few. This ubiquitous noise was first noticed as an effect in vacuum tubes by Johnson (1925); an extensive review is given by Press (1978). The nexus between the low-frequency noise component and its colour is to be found in the trend of the spectral density of the stochastic

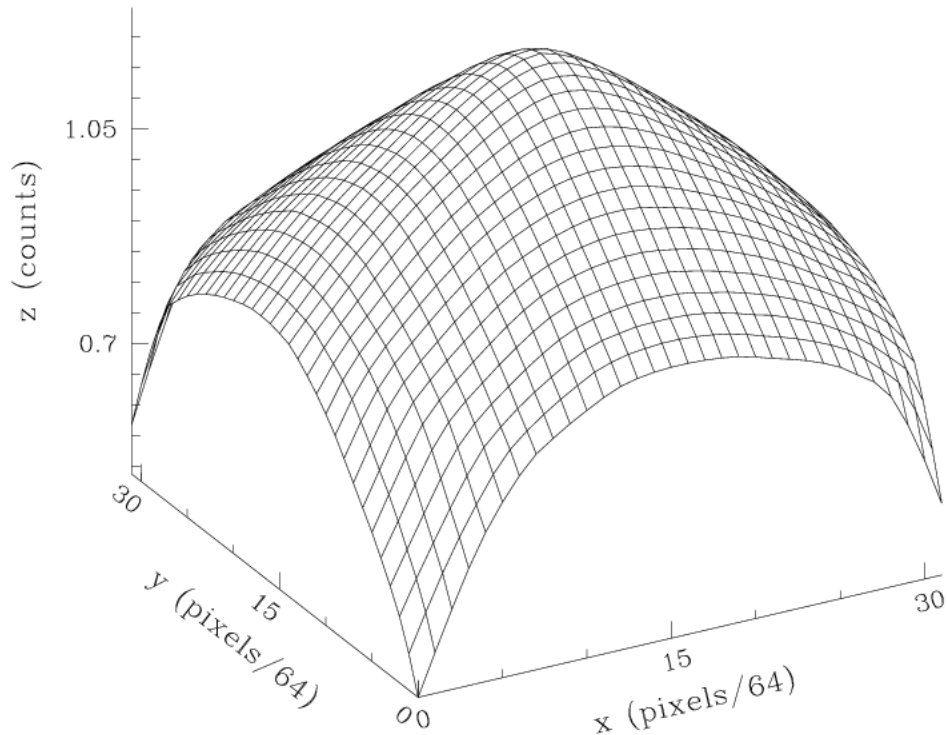


Figure 2.7: from Kane et al. 2004 (WASP0 prototype), illustrating the vignetting distortion across the frame.

process, which scales with frequency as $1/f^\alpha$. For $\alpha = 0$ we have the well known ‘white noise’ which shows a flat spectral distribution. For $\alpha = 1$ we have what is commonly referred to as flicker noise or ‘pink noise’, while for $\alpha = 2$ we have the known Brownian noise or ‘dark noise’. Linear systematics in ground-based surveys are mostly due to airmass variations during the night, variations in the telescope tracking and changing atmospheric conditions.

The SuperWASP data suffer from a variety of sources of systematic errors (see Collier Cameron et al. 2006). Because SuperWASP is wide-field, spatially dependent effects which are normally assumed to be constant across the frame vary significantly from one side of the frame to the other. For example, the SuperWASP band-pass

spans the visible spectrum, introducing significant colour-dependent terms into the extinction correction. The PPWASP process of the pipeline has been designed to remove these colour-dependent effects from the data. However, some systematics still remain. For example, bright moonlight or changing atmospheric conditions, can reduce the contrast between faint stars and the sky background, altering the rejection threshold for faint sources and biasing the photometry for faint stars. The SuperWASP camera lenses are vignetted across the entire field of view. Figure 2.7, taken from Kane et al. (2004), shows an example of vignetting distortion that can affect the position and the shape of the stellar profile. This effect tends to be particularly severe in the corners of the image.

Furthermore, temperature changes during the night can affect the camera focus, changing the shape of the point spread function across the field and biasing the photometry for fainter stars. These known systematic effects, and probably others not yet identified, have a serious impact on the detection threshold for transits. In order to remove systematic errors from the data SuperWASP employs an implementation of the Tamuz algorithm (Tamuz et al., 2005), see also Collier Cameron et al. (2006). The Tamuz algorithm searches for linear combinations of systematic effects in the data, of the kind mentioned above, in the case where the uncertainties in the measurements are unequal. The algorithm reduces to the Principal Component Analysis (PCA) for equal uncertainties in the measurements (Tamuz et al., 2005).

2.5 De-trending algorithm

Searching for low amplitude variability, as is the case when searching for transiting planets, involves finding weak periodic signals in noisy data. It is therefore of prime importance to identify and remove any covariant noise component which may hide the transit signal. The Tamuz algorithm removes systematic trends on a star by star basis, as long as these effects are present in a large number of light curves. We consider a set of N light curves, each of which consists of M observations. We first define the residual magnitude for each observation to be the stellar magnitude after subtracting the average magnitude of the individual star m_{ij} ; with $j = 1, \dots, M$. The algorithm finds the first linear systematic trend represented by the basic functions $a_j c_i$; of the i^{th} star at time j , by minimising the following expression:

$$\mathcal{S}_i^2 = \sum_j \frac{(m_{ij} - c_i a_j)^2}{\sigma_{ij}^2} \quad (2.2)$$

where σ_{ij} is the uncertainty in the magnitude of star i at time j and m_{ij} is the residual magnitude of star i at time j . Via an iterative procedure the two sets of coefficients that best describe the first linear trend are estimated. Subsequently, the whole procedure is repeated to eliminate different systematic effects hidden in the data. We define the first sets of parameters $c_i^{(1)}, a_j^{(1)}$, and we then remove these effects one after the other from the data as follows: $m_{ij}^{(k)} = m_{ij} - c_i^{(k)} a_j^{(k)}$ where k is an integer. This procedure is then repeated until no more significant trends are found in the data, i.e. when the change in the residual \mathcal{S}^2 , between two successive steps, is less than 0.01%. The basic functions $c_j^{(k)}$ represent the k^{th} red noise source at time j , while the $a_j^{(k)}$ coefficients represent the extent to which the star i is effected by the k^{th}

source of red noise. Our experience with the SuperWASP implementation of Tamuz algorithm suggests that four iterations are sufficient to remove the most significant linear trends in the data, as discussed in Collier Cameron et al. (2006). Despite the high efficiency of the Tamuz algorithm, a residual component of covariant noise is still present in the data after de-trending. These components are mostly due to poor background subtraction, and in particular, due to temperature variations causing spatially-dependent focussing variations. The latter effect introduces systematic errors which are not linearly separable and can not be fully removed by the de-trending algorithm. This residual noise component can still be significant at the millimagnitude level thus preventing planet detection.

2.6 Planet detection and candidate selection

Once the data have been de-trended and the major sources of covariant noise have been removed, the light-curve of thousands of sources are searched for transit signals by means of a Box Least-Square algorithm (BLS by Kovács et al. 2002). The BLS uses the anticipated square shape of the transit light-curve and performs a least-squares fit of step functions to the light-curve, folded on different trial periods. The BLS produces a large sample of stars showing transit-like light-curves that need to be analysed.

2.6.1 BLS algorithm

The SuperWASP BLS implementation, HUNTER, is a variant of the fitting model described in Kovács et al. (2002) reformulated such that the goodness-of-fit criterion has the dimensions of the χ^2 statistic (Collier Cameron et al., 2006). The grid of sampling frequencies is chosen such that the accumulated phase difference between successive frequencies, calculated over the length of the data set, corresponds to the transit width at the longest period searched. At each trial frequency a set of transit epochs e is defined at phase intervals equal to the transit width at that frequency. At each trial period and epoch the fitted transit depth and χ^2 statistic are calculated. We define $\Delta\chi^2$ to be the improvement in the fit (χ^2) when compared to that of a constant light-curve (χ_0^2); a transit event will thus yield large $\Delta\chi^2$ values. More details on the BLS are given in chapter 3 and also in Collier Cameron et al. (2006).

The HUNTER procedure rejects variable stars, stars with less than two transits and solutions with non-uniform phase-folded light-curves that show gaps longer than 2.5 times the transit duration. Nevertheless, the majority of the stars selected by the fitting routine are false positive detections, mostly due to grazing eclipsing binaries contaminating the light of the target star (see e.g. Brown 2003). In order to reduce the quantity of selected systems, planetary candidates must satisfy a number of tests to be considered high-priority spectroscopic targets. Therefore, further selection criteria such as the S_{red} threshold (see Pont et al. 2006), the “anti-transit” threshold (see Burke et al. 2006) to cite just a few, are needed. Out of several thousand stars typically between 100 and 200 objects satisfy the selection criteria. For these, a Markov Chain Monte Carlo (MCMC) algorithm (Collier Cameron et al. 2007 and reference therein) is applied to derive the planet and stellar parameters

more accurately.

2.6.2 Candidate selection

The final list of planetary transit candidates is then visually inspected by members of the SuperWASP consortium. We use the VSI interface, which allows a simultaneous inspection of the phase-folded transit light-curve, together with all the estimated refined parameters such as the orbital period, the transit duration, planetary and stellar radii, transit impact parameter etc. (see Collier Cameron et al. 2007 for the full analysis). A plot of the reduced proper motion (RPM) versus the $H - J$ colour is used to identify dwarfs from giant stars. In addition SuperWASP images can be retrieved to check for blends.

Each candidate is assessed taking into account all available data, and a final short-list of high priority candidates is produced. For these targets, follow up photometry and spectroscopy are carried out in order to certify the candidate planetary nature.

2.7 Summary

SuperWASP is the UK's leading project in the search for transiting extra-solar planets and is the world's most successful ground-based transit survey with 24 previously unknown extra-solar planets discovered in the period 2006-2008. SuperWASP is playing an extremely important rôle, contributing actively not only to the detection of unknown planetary systems, but also to their direct characterisation and understanding. It is now known that there are a large variety of extra-solar planets (see

e.g. the extra-solar planets encyclopedia at <http://exoplanet.eu/> for a review). The range in planetary systems discovered by transit and other techniques represents a significant new challenge for existing theories of planetary formation and evolution (see e.g. Ida & Lin 2008, and Ford 2006). Some of the planets discovered by SuperWASP are VHJ in orbits with periods of few days and less. For a review of the SuperWASP project see the web-site <http://www.superwasp.org/>. Some examples of SuperWASP planets can be found in Cameron et al. (2007), West et al. (2009), Hebb et al. (2008).

Chapter 3

Characteristics of and detection limits for
simulated transits of sub-stellar and
terrestrial companions to white dwarfs in
the SuperWASP survey

Abstract

I have investigated the transit detection limits for sub-stellar and planetary companions around white dwarfs in SuperWASP data. Because white dwarfs have approximately the same size as the Earth, any brown dwarf or gas giant companion will totally eclipse it and even bodies smaller than the Moon will have relatively large transit depths ($> 1\%$), detectable in good signal-to-noise light-curves. I have performed extensive simulations for transiting companions around white dwarfs (WDs)

with radii spanning $\sim 0.3\text{--}12 R_{\oplus}$, with orbital periods between 2 hours and 15 days and orbital distances from ~ 0.003 to 0.1 AU from the star. I have used a Box-Least Square fitting algorithm to recover the injected transit signals. My results show that for Gaussian random noise SuperWASP is sensitive to companions as small as the Moon, orbiting a $V \sim 12$ white dwarf. For fainter stars SuperWASP is sensitive to increasingly larger radius rocky bodies. Although SuperWASP detection sensitivity drops in the presence of covariant-noise structure in the data, I find that Earth-sized companions remain detectable, even in low-signal-to noise data. In the case of good quality data for which correlated noise is efficiently reduced by powerful de-trending, smaller bodies of sizes similar to Mars and Mercury can yield transits with signal-to-noise detectable by my implementation of the BLS routine.

3.1 Introduction

In recent years we have witnessed considerable progress in the search for extra-solar planets. Since the first detection of a “Hot Jupiter” around the main-sequence star 51 Peg (Mayor & Queloz 1995), the number of extra-solar planets has rapidly risen, and currently numbers about 350. Although the majority of extra-solar planets have been detected by radial velocity (RV) surveys, only planets that transit their parent stars offer the unique possibility to directly derive the planet mass and radius when combined with RV measurements, as the inclination i of the system is known (Sackett, 1999). This is also described in chapter § 1 Figure 1.4, equations 1.3 and 1.7. More recently, an increasing number of extra-solar planets (58) have been detected by dedicated planetary transit surveys including HATnet, the Hungarian-made Automated Telescope network (Bakos et al. 2004), TrES, the TRans-atlantic

Exoplanet Survey Network (e.g. Brown & Charbonneau 2000; Dunham et al. 2004; Alonso et al. 2004), OGLE, the Optical Gravitational Lensing Experiment (Udalski et al. 2002, 2003), XO, the search for *exo*-planets (McCullough et al. 2005), and SuperWASP, the UK Wide-Angle Search for Planets (Pollacco et al. 2006). Among the wide-field ground-based photometric surveys SuperWASP has been the most successful planet finding project, with 24 previously unknown exo-planets detected in the last two years (e.g. Cameron et al. 2007, and on-line <http://exoplanet.eu/>). Planet detection via the transit technique involves searching for periodic dips in stellar light-curves caused by the orbital revolution of a transiting planet, blocking a fraction of the stellar light (see chapter §1 Figure 1.3). Only planets with their orbital planes aligned within a few degrees to the line of sight are visible, this is defined by the geometric transit probability as derived in chapter §1 equation 1.3 and illustrated in Figure 1.4 (see also Charbonneau et al. 2007; Koch & Borucki 1996). The transit probability, P_{tr} , represents the fraction of the area of the celestial sphere swept out by the shadow of the planet during one orbital period. This constraint on the number of observable systems explains the relatively low number of transiting planets when compared to radial velocity studies.

For a given planetary radius, the transit depth is directly proportional to the square of the planet to star ratio. Therefore, planets orbiting a main-sequence solar-type star have extremely shallow eclipses, $\sim 10^{-2}$ for a giant planet and $\sim 10^{-4}$ for an Earth-sized planet. Current ground-based wide-field surveys can achieve photometric accuracies of better than 1%, needed for planet detection, only for bright stars (SuperWASP range $9 < V < 12$), and are therefore insensitive to planetary bodies smaller than \sim Jupiter around main-sequence stars. To date the smallest transiting extra-solar planet detected is HAT-P-11b, a Neptune-size planet transiting a K

dwarf star (Bakos et al. 2009).

A strong advantage over main sequence primaries is offered by white dwarf stars. Indeed, because of the small dimension of white dwarfs (\sim Earth), any sub-stellar or gas giant companion, orbiting the star, will completely eclipse it, while bodies as small as the Moon will have relatively large transit depths ($\sim 3\%$), with the only caveat being that it is as yet unclear whether such systems survive the later stages of stellar evolution. I briefly discuss the likelihood of sub-stellar and planetary survival to stellar evolution.

Observations indicate that sub-stellar and planetary companions in wide orbits, beyond the extent of the red giant (RGB) and the asymptotic giant (AGB) radius, can survive post main-sequence stellar evolution. For example evolved RGB stars are known to harbour sub-stellar and planetary companions (see e.g. Frink et al. 2002, Sato et al. 2003, Sato et al. 2008; Hatzes et al. 2005). Moreover, we know at least two sub-stellar objects that survived their parent star evolution and become close companions to the white dwarf (e.g. WD0137-349 and GD1400, Maxted et al. 2006; Burleigh et al. 2006; and Burleigh et al. 2009 in prep.). GD1400B and WD0137-349B are the only two sub-stellar companions known to have survived the common envelope (CE) phase of stellar evolution, and WD0137-349B is the lowest mass object known ($\sim 50 M_{\text{JUP}}$) to have done so. The detection of more such systems will allow us to place observational upper limits on the mass of sub-stellar companions that survive the CE evolution. For example, can Hot Jupiters survive their parent star evolution? Recently Silvotti et al. (2007) reported the detection of planetary mass companion in a 1.7 AU orbit around an extreme Horizontal Branch (HB) star. Moreover, Mullally et al. (2008) found convincing evidence of a $2 M_{\text{JUP}}$ (Jupiter mass) planet orbiting a pulsating white dwarf with a period of 4.5 years. The latter, if

confirmed, will be the first planet detected around a white dwarf and will show that planets in wide orbits do indeed survive their parent star evolution. Short-period companions are not expected to survive the red giant phase of stellar evolution (see Villaver & Livio 2007). Nevertheless, the detection of dust and gas discs around about 14 WDs (showing as infra-red excess) (Jura 2003, Jura 2008; Reach et al. 2005; Farihi et al. 2008, Farihi et al. 2009; Gänsicke et al. 2006, Gänsicke et al. 2007) suggests that asteroids and small rocky bodies, remnants of an old planetary system, can get dynamically destabilised during the post main-sequence phase of solar system evolution (Debes & Sigurdsson 2002) and kicked into orbits so close to the star's Roche limit that they are disrupted by tidal forces. The detection of any such companion, will open an exciting chapter in the study of extra-solar planet evolution helping to constrain theoretical models of CE and close binary evolution. They may also help us to understand the ultimate fate of Hot Jupiter systems as well as our own solar system in the post main-sequence phase. The aim of this study is to investigate whether transiting brown dwarfs, gas giants and terrestrial planets in close orbits around white dwarfs can be detected using data from the foremost ground-based survey, SuperWASP. I have designed and performed extensive simulations to investigate the characteristics and detection limits for these systems.

3.2 Simulations

I have used the time sampling of SuperWASP photometric data to create a set of synthetic light-curves in to which fake transit signals have been injected. The synthetic data set covers three magnitude ranges of $V \sim 12, 13, 15$, commensurate with the brightness of white dwarfs in the SuperWASP survey. Because SuperWASP

data show residual covariant-noise structure even after de-trending by means of the Tamuz algorithm (see § 1.5 chapter 2), I have tested the transit recovery rate both in the case of: 1) uncorrelated white noise, and 2) correlated red noise. First, I simulated white noise light-curves consisting of a transit-like event injected at different orbital periods and for different companion sizes, plus a zero mean Gaussian noise component of standard deviation σ , equal for all data points. I chose σ to be the mean error on the points in a real SuperWASP light-curve at a given magnitude. To account for red noise in the data, I injected fake transits into a set of SuperWASP light-curves obtained from a densely observed field from the 2004 SuperWASP season. This accounted for different patterns of noise in the data and allowed me to test my detection sensitivity in different noise regimes. For each light-curve I used the SuperWASP pipeline fluxes and errors derived after de-trending by the Tamuz algorithm (Tamuz et al. 2005).

3.2.1 Characteristics of the transit signals

A transit signal is characterised by its *duration*, *depth* and *shape*. The known transiting extra-solar planets around solar-type stars, show signals characterised by an ingress, a flat bottom and an egress, with typical transit durations of between 2 to 3 hours and eclipse depths of approximately 1% (see for example West et al. 2009 and Hebb et al. 2008). My simulations have been designed assuming circular orbits and fixed stellar parameters. I considered a typical 1 Gyr old Carbon-core white dwarf of mass $0.6 M_{\odot}$ and radius $\sim 0.013 R_{\odot} \sim 1 R_{\oplus}$. The observed mass distribution of isolated white dwarfs is sharply peaked around $0.6 M_{\odot}$ (see Fontaine et al. 2001 for details and references therein). However, low-amplitude tails extends

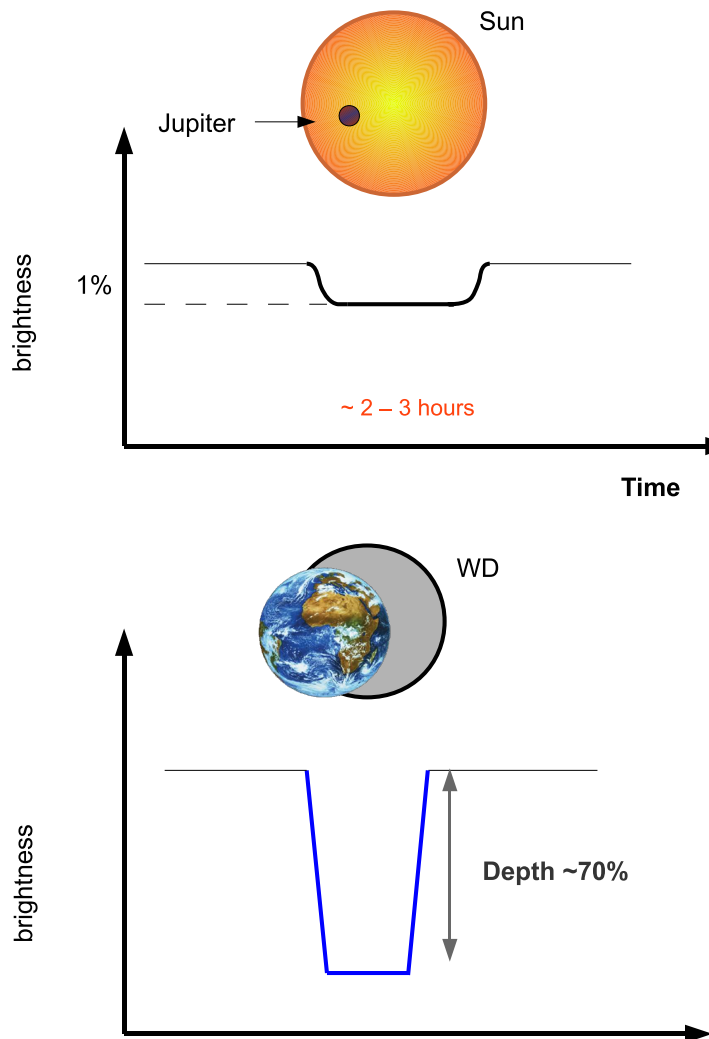


Figure 3.1: Comparison of the transit light-curve of a Jupiter across a sun-like star with an Earth across a white dwarf. The fractional change in brightness is significantly increased in the case of WD primaries. The sketch shows that any objects with size similar to the Earth or larger will completely eclipse the WD (transit depth $> 70\%$). Smaller bodies of size similar to the Moon can yield large transit depths of $\sim 1\%$, comparable to the depth of a transit signal due to a Jupiter planet around a solar-type star.

at both ends of the mass spectrum ~ 0.3 to $\sim 1.2 M_{\odot}$. The majority of white dwarfs have masses around the mean value with a very small dispersion. I have parametrised the simulations in terms of the orbital period of the planet-star system

and I have considered periods in the range ~ 2 hours - 15 days (i.e. orbital distances between ~ 0.003 and 0.1 AU). I chose the shorter orbital period to yield an orbital separation close to the Roche radius of the white dwarf. The Roche limit is the closest distance an object can come to another object without being pulled apart by tidal forces (see e.g. Roche 1859 and Paczyński 1971). I have limited the transit search to periods of ≤ 15 days in order to recover more than five transit repetitions for a typical SuperWASP light-curve of ~ 150 days. I have investigated transits for planets ranging from Moon size to Jupiter and/or a brown dwarf sizes (which have approximately the same radius of $\sim 10-12 R_{\oplus}$).

Figure 3.1 illustrate two examples of a schematic transit light-curves. The top panel shows the typical transit light-curve expected from a Hot Jupiter transiting a solar-type star yielding a transit depth of $\sim 1\%$. The lower panel, shows the simulated transit light-curve for an Earth-sized object transiting a white dwarf star yielding a considerably large depth of $\sim 70\%$. Figure 3.1 emphasises the strong gain obtained in the transit depth when considering transits of white dwarf primaries. Any companion with radius larger than the Earth will completely eclipse the white dwarf. Even rocky bodies of sizes smaller than the Moon (e.g. as small as the size of UK) could have detectable transit signals (depths $\sim 1\%$) in good signal-to-noise data. For my choice of parameters the simulated transit signals show very short duration (between 1 and 32 minutes for companions ranging from the Moon to Jupiter sizes) and exhibit large transit depths (between $\sim 3\%$ for the Moon to $\sim 100\%$ for any body larger than the Earth). Figure 3.2 and Figure 3.3 show the transit characteristics derived for the systems studied in this work. Figure 3.2 upper panel shows the systems transit durations in the parameter space defined by the planet radius in units of the Earth radius, R_{\oplus} , versus orbital period in days. The

lower panel, illustrates the transit depths for different companion sizes. I show the transit probability in Figure 3.3. The transit probability is the geometric probability that a given binary-system has its orbital plane aligned to the Earth line of sight. The transit probability ranges from $\sim 20\%$ for a Jupiter or a BD companion in a few hour orbit around a white dwarf, to $< 1\%$ for period > 10 days. For smaller companion sizes the transit probability decreases rapidly with increasing orbital period, $P_{tr} < 0.1\%$ for $P > 10$ days.

3.2.2 Synthetic SuperWASP light-curves

The set of synthetic light-curves have been modelled by injecting fake transit signals into the phase folded light-curves at random orbital period P within the period-window searched. For each trial period P I have calculated the phase width ϕ_{tr} of the transit event. Finally I have reduced the stellar magnitude by a factor proportional to the transit depth, for all data points which fall in the transit bin, i.e. that have phase values $0 \leq \phi_i \leq \phi_{tr}$, where $i = 1, \dots, N$ observations. Figure 3.4 show a sketch of a model box-like function, in red I highlight the width of the transit bin. L stands for *low* points (in-transit) and H stands for *high* points (out-of-transit) see § 3.2.3 for a detailed discussion on the model function. The synthetic transit light-curves were modelled assuming simple box-like profiles, with no data points during transit ingress and egress. This is justified by the expected short transit durations of the systems studied here and the SuperWASP observing cadence of $\sim 8-10$ minutes. Figure 3.5 shows an example of two simulated transit light-curves. The top panel shows the synthetic light-curve of an hypothetical eclipsing WD+BD binary system with an orbital period of $P \sim 116$ minutes similar to WD0137-349 (Maxted et al.,

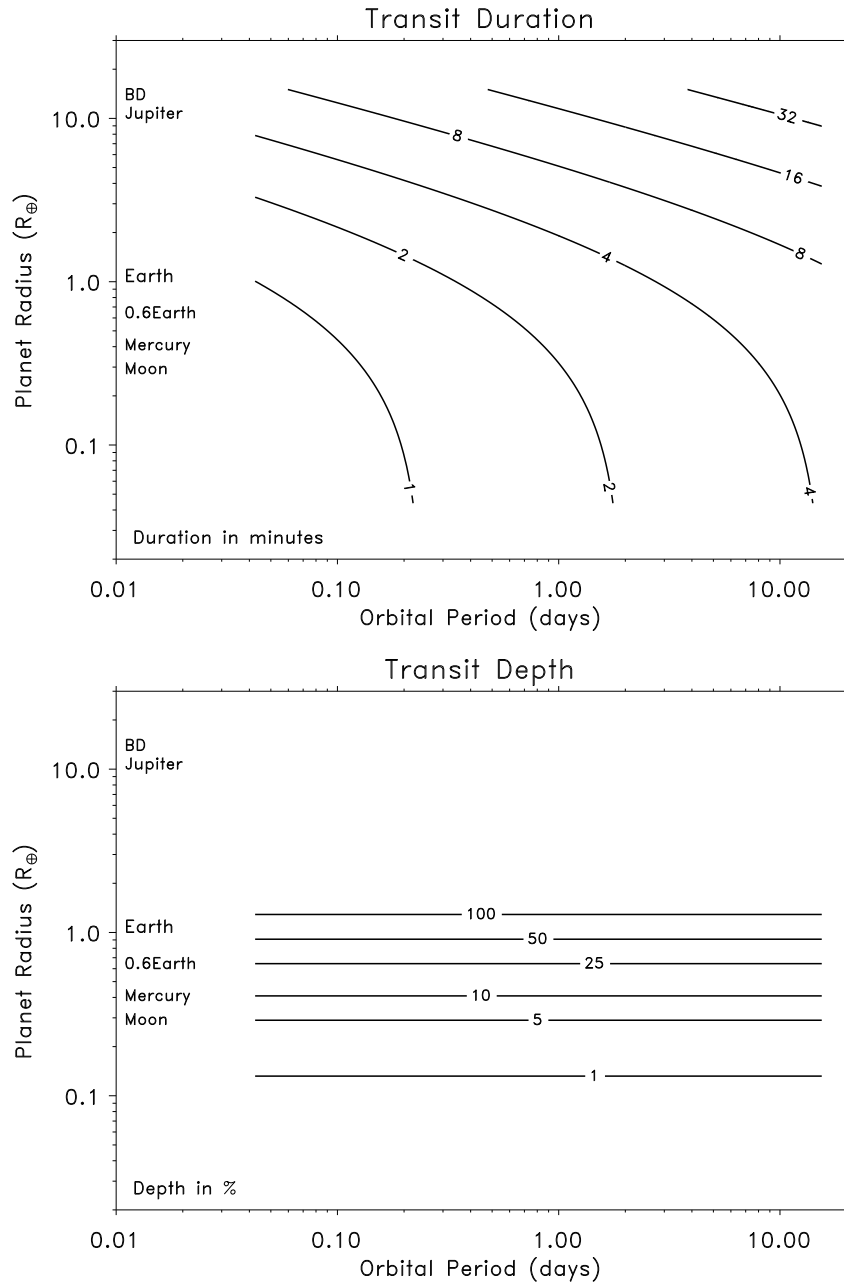


Figure 3.2: Upper panel: contour of transit duration (mins) for R_{pl} between ~ 0.3 and $10\text{--}12 R_{\oplus}$ (i.e. between the Moon and a BD or Jupiter size body), and orbital periods P between 2h and 15 days. I have assumed a white dwarf of mass $0.6 M_{\odot}$ and radius $0.013 R_{\odot} \sim 1 R_{\oplus}$. Lower panel: transit depths (%) for the same parameters as above.

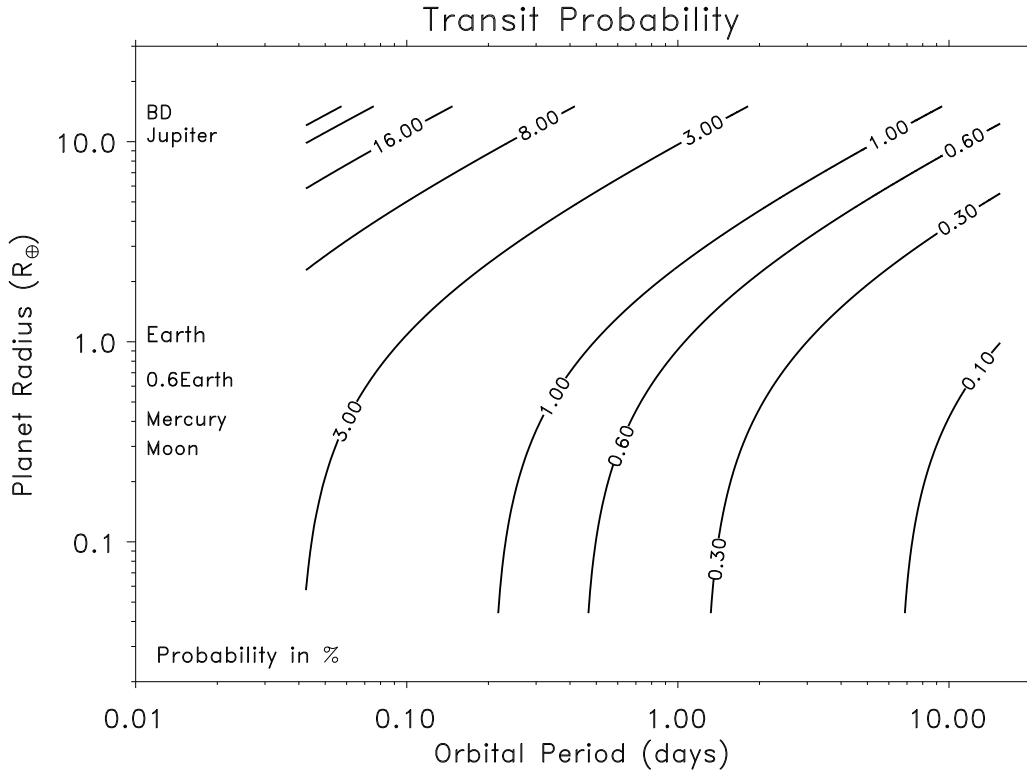


Figure 3.3: contour of transit Probability (%) for R_{pl} and orbital periods as in Figure 3.2.

2006) (which itself does not show eclipses). The lower panel shows the simulated transit light-curve for a rocky body of the size of the Earth in a ~ 5 h orbit.

To recover the transit signals injected into the set of synthetic light-curves I used a modified Box Least Square (BLS) algorithm, see Kovács et al. (2002). I will describe the implementation adopted in this work, and I will highlight the differences between the classic BLS algorithm (Kovács et al., 2002) and my modified version.

3.2.3 Detecting transit signals

The BLS algorithm performs a least-square fit of box-like functions to the transit light-curves, folded at different trial periods. The BLS algorithm is most sensitive

when the modelled box-width closely matches the duration of the true transit signal. Thus, to ensure that the BLS search was sensitive across the expected range of transit durations, I chose to search a grid of durations of $D_{tr} = [1, 2, 4, 8, 16, 32]$ minutes (see also Figure 3.2). This frequency grid covers the range in transit duration for all simulated light-curves over the parameter space (for brown dwarfs/gas giants and terrestrial planets in orbit up to ~ 15 days, see Figure 3.2 top panel). I define the grid of frequencies sampled by the BLS as follows:

$$F_{max} = \frac{1}{P_{min}} \quad , \quad F_{min} = \frac{1}{P_{max}} \quad , \quad (3.1)$$

where $P_{min} \sim 2$ hour and $P_{max} \sim 15$ day. The number of sampling frequencies used by the routine is given by:

$$n_f = \frac{\text{int}[F_{max} - F_{min}]}{\delta F} \quad , \quad (3.2)$$

and I have chosen a fixed frequency step given by:

$$\delta F = \frac{D_{tr} F_{min}}{\Delta T} \quad , \quad (3.3)$$

where D_{tr} is the transit duration and ΔT is the time spanned by the data. I only accept trial periods if the difference between subsequent periods searched is >1 second. This allows me to control oversampling at short periods.

I denote the data set by $\{m_i\}$, of $i = 1, \dots, n$ observations, and define the residual from each observation to be the stellar magnitude after subtracting the optimal

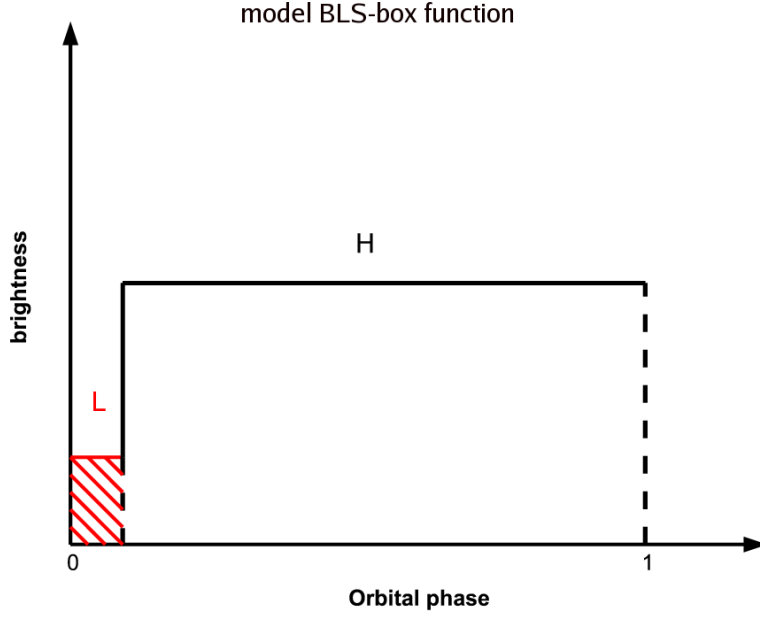


Figure 3.4: A phase-folded light-curve for a simulated transit signal. The photometric points falling in the transit bin are highlighted in red (L). H indicates the out-of-transit light-curve (black).

average magnitude \hat{m} , of the individual star, $\tilde{m}_i = \sum_i m_i - \hat{m}$. Where \hat{m} is the weighted mean defined as:

$$\hat{m} = \frac{\sum_i m_i w_i}{\sum_i w_i} \quad (3.4)$$

where w_i is the weight defined as $w_i = \sigma_i^{-2}$. The shape of the model light-curve is approximated by a periodic two-level signal, an *in-transit* phase flagged as L for *low* points, and an *out-of-transit* phase flagged as H for *high* points (see Kovács et al. 2002, and Figure 3.4).

For each trial frequency I evaluate the phase folded light-curve and I define a set of transit epochs, e , at phase intervals equal to the transit width. The number of

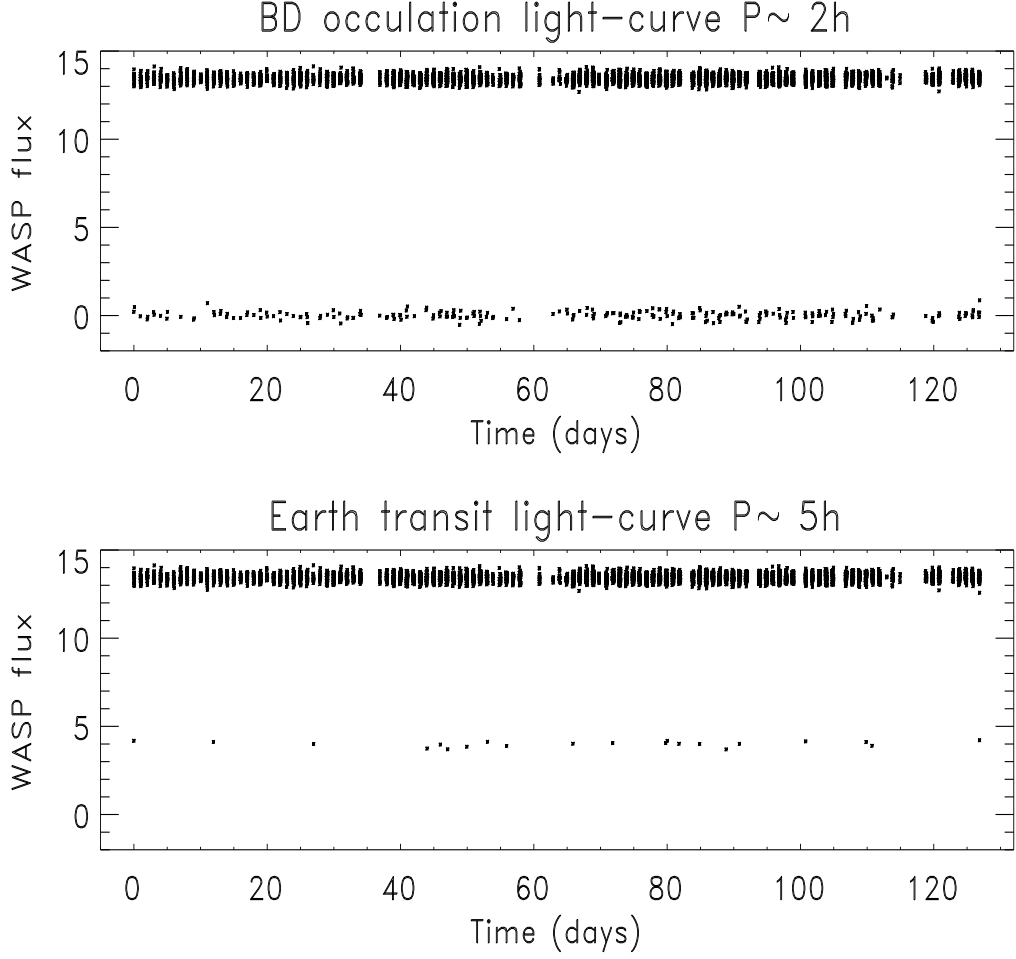


Figure 3.5: Two examples of synthetic light-curves. Top, an eclipsing brown dwarf in an orbit with a period of ~ 2 h, around a WD. Bottom, an Earth-sized companion to a WD in ~ 5 h orbit.

epochs N_e (or bins) is given by $N_e = P/D_{tr}$, where P is the trial orbital period and D_{tr} is the duration of the transit. I calculate χ^2 over the N_e bins such that:

$$\chi^2 = \sum_{i \in L} w_i (\tilde{m}_i - L)^2 + \sum_{i \in H} w_i (\tilde{m}_i - H)^2 . \quad (3.5)$$

where w_i is calculated over the in-transit and out of transit light-curve respectively, L indicates the sum over the transit bin, and H the sum over the out-of-transit light-curve. In my implementation of the BLS, the number of epochs, N_e , at each

iteration depends only on the trial period. Thus substantial computational speed is achieved because the χ^2 statistic of subsequent iterations is obtained simply by adjusting for the number of bins N_e at different trial periods. The minimisation of χ^2 yields simple arithmetic weighted averages over the corresponding in-transit (L) and out-of-transit (H) phases and are given by:

$$\hat{L} = \frac{s}{r} \quad \text{and} \quad \hat{H} = \frac{-s}{t-r} \quad (3.6)$$

where $s = \sum_{i \in L} w_i \tilde{m}_i$, $r = \sum_{i \in L} w_i$, and $t = [\sum_j \sigma_j^{-2}]$, summing over the full dataset. Thus the numerator in the equation 3.6 for \hat{H} is obtained as $-s = \sum_{j=1}^n -\sum_{i \in H} w_i \tilde{m}_i$. \hat{L} and \hat{H} are the mean light levels inside of, and outside of transit.

To obtain equation 3.6 I write the sum over H as $\sum_{i \in H} w_i = t - \sum_{i \in L} w_i = t - r$. The variances for \hat{L} and \hat{H} are:

$$Var(\hat{L}) = \frac{1}{r}, \quad Var(\hat{H}) = \frac{1}{t-r}. \quad (3.7)$$

It is straightforward to show that the square sum of the deviations D calculated in Kovács et al. (2002) has the dimensions of χ^2 , once I multiply it by t , the sum of the weights over the full dataset. I use the estimated values of \hat{L} and \hat{H} to replace the parameters in the expression for χ^2 and obtain:

$$\chi^2 = \sum_{i=1}^n w_i \tilde{m}_i^2 - \frac{s^2 t}{r(t-r)} \quad (3.8)$$

The improvement on the fit (χ^2) to the data is defined as:

$$\Delta\chi^2 = \chi_0^2 - \chi^2 \quad \text{where} \quad \Delta\chi^2 = \frac{s^2 t}{r(t-r)} \quad (3.9)$$

and $\chi_0^2 = \sum_{i=1}^n w_i \tilde{m}_i^2$ represents an intrinsic measure of the spread of the data. This implies that $\Delta\chi^2$ is proportional to the square of the S/N value of the transit event.

Thus I can write $\Delta\chi^2 = (S/N)^2$ where S/N is given by:

$$S/N = \frac{\delta}{\sqrt{Var(\delta)}} \quad (3.10)$$

where the transit depth δ is given by $\delta = \hat{L} - \hat{H}$, that is:

$$\delta = \frac{st}{r(t-r)} \quad \text{where} \quad Var(\delta) = \frac{t}{r(t-r)} . \quad (3.11)$$

The χ^2 computation is repeated for all epochs \mathbf{e} in order to find the minimum of χ^2 for each trial period.

Planetary detections are strongly affected by the signal-to-noise value of the transit event. Good photometry is not always sufficient to ensure the detection of a transit; and in particular, for signals dominated by noise structure correlated on the same time scale as the transit (see Pont et al. 2006). Therefore, a S/N criterion has to be satisfied in order to confirm a transit detection.

From consideration of pure random Gaussian noise I can derive an estimate for the expected signal-to-noise SN_E of a transit event on the basis of the a priori knowledge of the expected depth of the signal (see Figure 3.2 lower-panel) and the quality of SuperWASP data at different magnitudes.

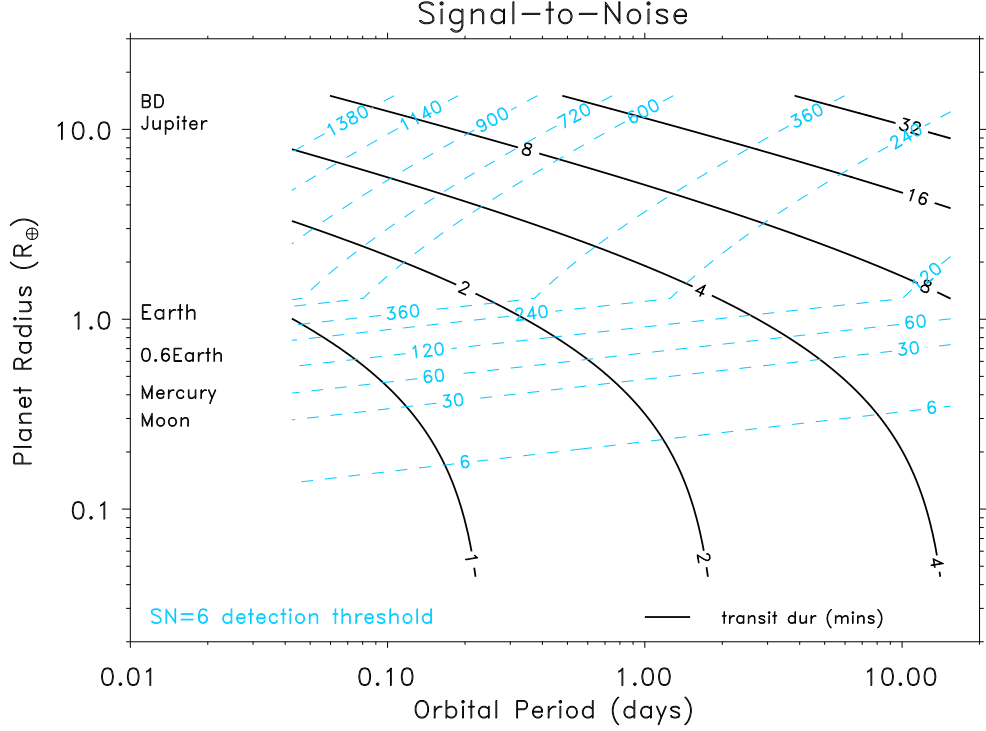


Figure 3.6: Estimated signal-to-noise for transit signals of the systems investigated in this work (Blue dashed lines). I used the a priori knowledge of the quality of SuperWASP data at different magnitudes and the expected depth of the transit signals as illustrated in Figure 3.2-lower panel. I have considered light-curves of 3000 photometric points of photometric accuracy $\sigma = 1\%$ ($V \sim 12$). The threshold for detection is $SN_E > 6$. This limit corresponds to the signal-to-noise limit that minimises statistical false positives seen in Kovács et al. (2002). Black-solid line indicates the transit duration in minutes.

3.3 Estimating SN_E

I describe the quality of the light-curves using the individual photometric errors σ_i as obtained from the SuperWASP archive. I then calculate the mean error as $\langle \sigma \rangle$ which is used to describe the accuracy of each measurement in a white noise light-curve. For a transiting planet the signal-to-noise is given by:

$$S/N = \frac{\delta}{\sigma} \sqrt{N_{tr}} \quad (3.12)$$

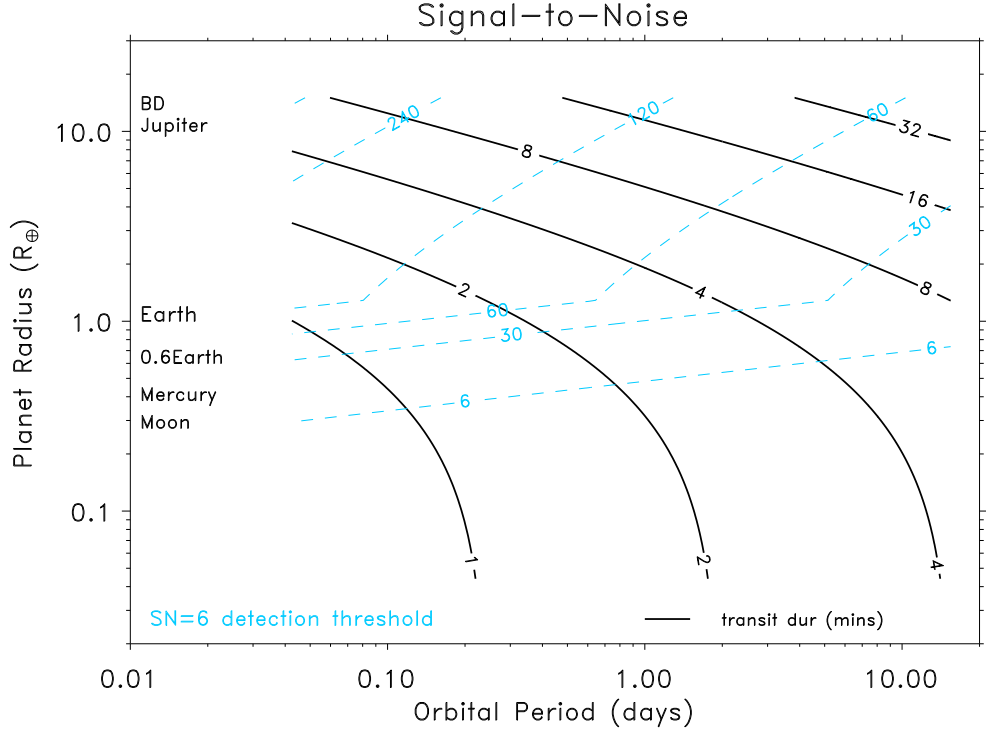


Figure 3.7: Same as Figure 3.6 but for $\sigma = 5\%$ ($V \sim 13$).

where δ is the depth of the eclipse, and N_{tr} is the number of points in-transit. Using equation 3.12 I can investigate the expected signal-to-noise values (SN_E) for my transiting planets in SuperWASP light-curves. I explored the SN_E values in the parameter space defined by companions from Moon size to Jupiter or brown dwarf sizes (which have similar radii), system orbital periods between 2 hour to 15 day and SuperWASP magnitudes of $V \sim 12, 13, 15$ (which correspond to mean light-curve photometric accuracies of $\sigma \sim 1\%, 5\%$ and 10%). A typical light-curve of about 3000 photometric points was considered. For each trial period P and transit duration D_{tr} the fraction, N_{tr} , of photometric points falling in the transit bin is defined as:

$$N_{tr} = 3000 \times \frac{D_{tr}}{P} . \quad (3.13)$$

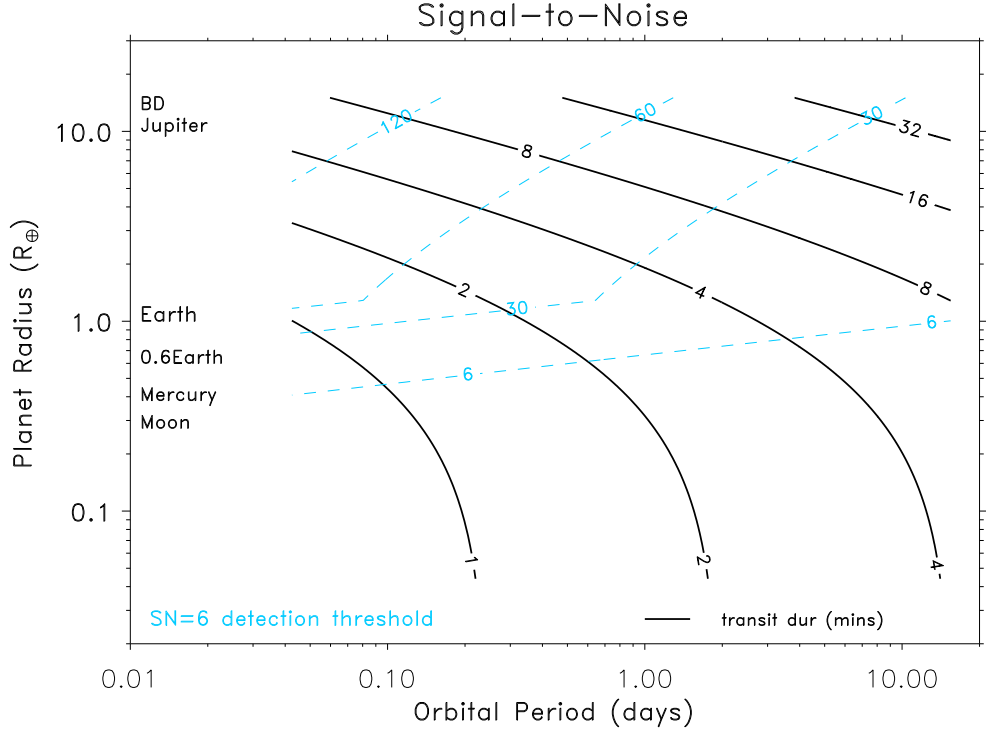


Figure 3.8: Same as Figures 3.6 and 3.7 for $\sigma = 10\%$ ($V \sim 15$).

Then the expected signal-to-noise SN_E is given by:

$$SN_E = \frac{\delta}{\sigma} \sqrt{N_{tr}} \quad (3.14)$$

where $\sigma/\sqrt{N_{tr}}$ represent the standard deviation of the average of all measurements within the transit bin. Following equations 10–11 from Kovács et al. (2002) I consider a detection threshold of $SN_E > 6$. This corresponds to the $SDE = 6$ limit that minimises statistical false positives seen in Kovács et al. (2002). The SDE is a measure of the statistical significance of transit detection (more details on SDE statistics are also given in § 3.2). Figures 3.6, 3.7 and 3.8, show the results obtained for the SN_E . Blue-dashed lines are contours of constant values of SN_E .

The behaviour of the SN_E contours is due to the change between two different

regimes: 1) when the planetary radius is smaller than the stellar radius ($R_{pl} < R_*$) and 2) for $R_{pl} > R_*$. The knees in Figures 3.6, 3.7 and 3.8, appear at the transition between the two regimes when $R_{pl} = R_*$.

This becomes clearly visible if equation 3.14 is written in terms of the R_{pl} , R_* and the orbital period P . Using Kepler third law the equation for the transit duration can also be written in terms of the R_{pl} , the R_* and the orbital period P as follows:

$$D_{tr} = 2(R_{pl} + R_*) \times P^{-1/3} \times (2\pi GM_*)^{-1/3} . \quad (3.15)$$

Thus equation 3.13 becomes:

$$N_{tr} = CP^{-1/3} \times P^{-1} , \quad (3.16)$$

where $C = \frac{2 \times npts}{(2\pi GM_*)^{-1/3}}$, is a constant. The transit depth is also given by $\delta = (R_{pl}/R_*)^2$. Now by using equations 3.15 and 3.16, equation 3.14 assumes the following form:

$$SN_E = k \left(\frac{R_{pl}}{R_*} \right)^2 \sqrt{R_{pl} + R_*} P^{-1/3} , \quad (3.17)$$

where k is a new constant defined as $k = C/\sigma$. Finally in equation 3.17, the stellar radius(R_*) is also constant and for $R_{pl} = R_*$ the depth of the transit event becomes constant too. Therefore in the limit of $R_{pl} < R_*$ equation 3.17 becomes: This becomes:

$$SN_E \simeq R_{pl}^2 P^{-1/3} , \quad (3.18)$$

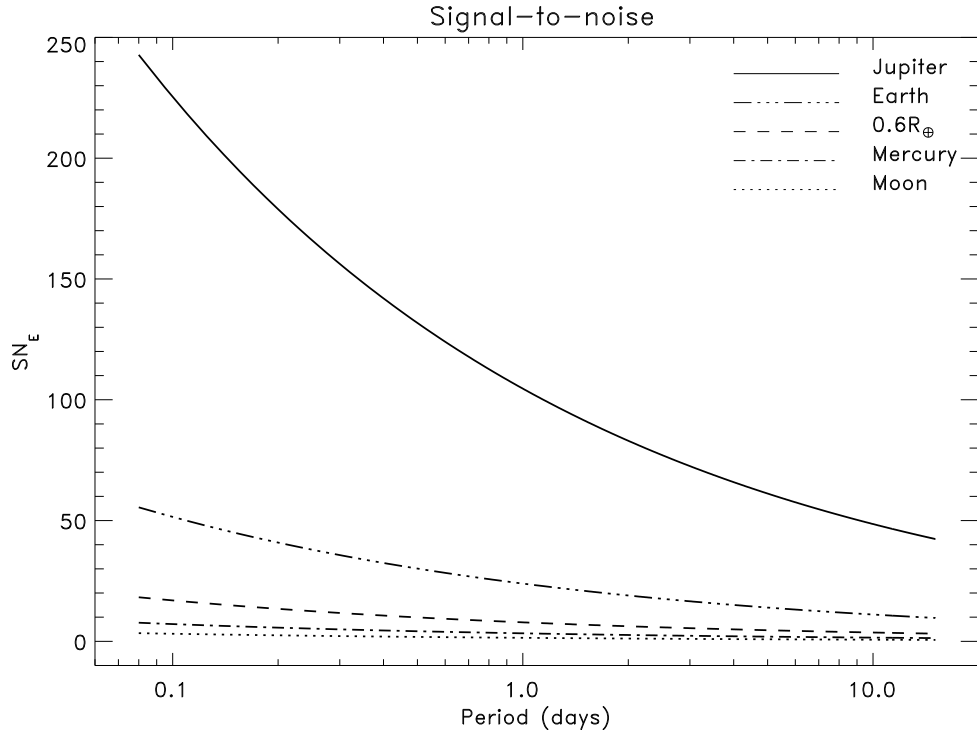


Figure 3.9: SN_E values for five different companions: Jupiter, the Earth, $0.6R_{\oplus}$, Mercury and the Moon. The estimated S/N is plotted versus the system orbital period P .

this implies that at each constant SN_E value the R_{pl} is proportional to the $P^{1/6}$. On the other hand, in the limit where $R_{pl} > R_{\star}$ I obtain:

$$SN_E \simeq R_{pl}^{1/2} P^{-1/3} , \quad (3.19)$$

so for a constant SN_E value the R_{pl} is proportional to the $P^{2/3}$. This explains the SN_E contours in Figures 3.6, 3.7 and 3.8. Figure 3.9 shows the trend of the SN_E values with respect to the orbital period P , for five fixed companion sizes: the Moon, Mercury, $0.6 \times$ Earth, the Earth and Jupiter.

From the calculations above I find that for bright stars ($V \sim 12$) companions of sizes

even smaller than the Moon should have S/N values greater than $6SN_E$, and should be detectable in SuperWASP light-curves (Figure 3.6). For fainter white dwarfs only bodies of increasingly larger sizes are detectable (Figure 3.7 and 3.8). If SuperWASP light-curves were not affected by residual correlated noise my estimate could have been considered a realistic description of SuperWASP detection limits. However, the presence of red noise reduces the BLS power of the detected signal thus reducing my detection rate. As discussed by Pont et al. (2006) in the presence of residual correlated noise the S/N of a transit signal is described by:

$$(S/N)^2 = \frac{\delta^2}{\frac{\sigma_w^2}{N_{tr}} + \frac{\sigma_r^2}{n_t}} \quad (3.20)$$

where σ_w is the standard deviation of the differential magnitudes in the transit bin for white noise, σ_r is the red noise contribution, N_{tr} is the number of points in transit and n_t is the number of observed distinct eclipses. Therefore, I expect my simulations to show lower detection rates and higher S/N detection thresholds for red noise when compared to white noise simulations. Before testing my prediction I have tested the BLS algorithm performance in the case of model light-curves of pure random Gaussian noise with no injected transit signals. I have interpreted the BLS power spectra in terms of the Signal Detection Efficiency (SDE) (see also Kovács et al. 2002), which is a measure of the S/N at the highest peak in a periodogram (more details are given in the next paragraph). This allowed me to test the algorithm false detection rate and therefore to set a SDE threshold value for the detection of a transit signature. In the following discussion I give a detailed explanation of the different steps used in my approach.

3.4 Characterisation of the BLS response

As discussed in paragraph §3.2.3 the Box-fitting routine first selects the highest S/N value at each trial period and secondly the highest S/N value over the whole grid of trial periods investigated (e.g. see equations 3.9 and 3.10). Because the detection of a transit signature is strongly dependent on the S/N value (see equations 3.10 and 3.20), I want to be able to identify significant peaks in a BLS periodogram. Thus, I define the *Signal Detection Efficiency* (SDE) (see Kovács et al. 2002) as:

$$SDE = \frac{S/N_{peak} - \langle S/N \rangle}{\sigma_{S/N}} \quad (3.21)$$

where S/N_{peak} is the S/N at the highest peak, $\langle S/N \rangle$ is the average S/N , and $\sigma_{S/N}$ is the standard deviation of the S/N over the frequency band tested. A Detection is then represented by the peak with the highest SDE . Because the BLS algorithm uses a finite bin size, the BLS power spectra strongly depend on the position of the transit within the folded time series. For unevenly sampled data there is a large dispersion in $D_{tr}/P = N_{tr}/N_{tot}$ at different epochs (see Gaudi et al. 2005). So that the SDE values strongly depends on the duration of the transit event. The BLS algorithm performs better when the bin size matches the duration of the transit event. Thus, the higher the number of bins used to partition the phased light-curve the higher and more stable the SDE values. Lower numbers of bins may yield lower SDE values due to occasional partial coverage of the transit event and larger bin sizes (see e.g. Kovács et al. 2002). For each trial period P my implementation of the BLS uses a bin dimension equal to the phase width of the expected transit at that period. One consequence of this is that in cases for which

the periods are multiples or sub-multiples of P , a fraction of in-transit points can be distributed over different bins, resulting in poor BLS performance. In such cases higher BLS power might be allocated to those periods.

In order to test the BLS response and to investigate the dependence of the SDE on the transit duration I have modelled the set of simulated transit light-curves to account for one hundred random phases offsets for each injected transit signal, orbital period and transit duration. As a consequence the results of my simulations should be equally effected by the above trend.

To assign a statistical significance to the highest peak in a BLS power spectrum (indicating a detection) I have tested the algorithm performance in the case of pure white noise data with no injected transit signals. By testing the algorithm false detection rate I have identified a SDE threshold that allows me to distinguish signals arising from real transits from those simply due to noise. This approach can be compared to the false alarm probability (FAP) test, extensively used in Fourier analysis (see for example the Lomb-Scargle algorithm, Scargle 1982; Press et al. 1992, and chapter 5).

3.4.1 BLS response to pure noise: testing the algorithm false detection rate

I derive the Probability Distribution Functions (PDFs) of the SDE in the case of data with no injected transits and only random Gaussian noise. Figure 3.10 shows an example of the BLS response in the case of a white noise light-curve with no injected transit signals. In Figure 3.10 the highest BLS power (y-axis) is chosen as

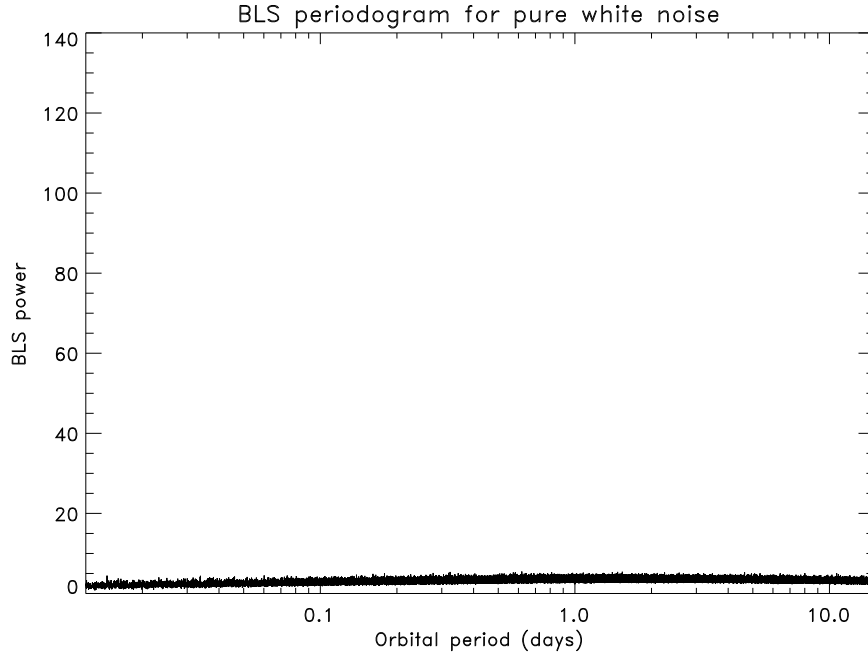


Figure 3.10: BLS power spectrum for a light-curve of pure Gaussian random noise with no injected transit signals.

in Figure 3.14 which shows for comparison the BLS response in the case of a transit signal due to an Earth-sized body, injected in the same light-curve with a period of ~ 5 h.

I performed extensive numerical tests to calculate the PDFs for different numbers of sampled frequencies, $n_f/2$, $n_f/5$, $n_f/7$, $n_f/10$, where n_f is defined as in equation 3.2. If these frequency samples are statistically independent I expect the probability of finding significant peaks in a noisy periodogram to increase as the number of trial frequencies increases. I tested this assumption by fitting a semi-theoretical model which estimates three different parameters: n_f that identify the real number of frequencies sampled, and a and b which account for the shape of the normal distribution describing the *SDE* (see Kovács et al., 2002, equation 7). In the following I derive the theoretical model used to fit the PDFs; I refer the reader to Kovács

et al. (2002) for a full discussion. Using equation 3.21 I can express the probability that SDE exceeds a generic value X as follows:

$$P(SDE > X) = P(S/N_{peak} > x) . \quad (3.22)$$

I define p as the probability that S/N has a value $> x$ over the N_e bins at a trial frequency f . The probability that SDE is exceeding X over all possible realisations \tilde{n} is then obtained as:

$$P(SDE > X) = P(S/N_{peak} > x) = 1 - (1 - p)^{\tilde{n}} , \quad (3.23)$$

the probability p can be estimated in the case of white noise light-curves with no signal injected. In this case, the photometric errors of the data points are all equal to σ (where σ is the average of the individual errors (σ_i) of the photometric points in the real SuperWASP light-curve). Then the S/N becomes a zero-mean random Gaussian variable with variance σ^2/n . The distribution describing the probability for the S/N is the Gaussian normal distribution. Thus I can write $\sigma_{S/N} = a\sigma/\sqrt{n}$ and $\langle S/N \rangle = b\sigma/\sqrt{n}$ where $a = \sqrt{1 - 2/\pi} = 0.60$ and $b = \sqrt{2/\pi} = 0.80$. The value for a and b are obtained by calculating the standard deviation and the mean using the definition of the Gaussian function. Then by replacing the variable S/N by a normalised random variable $\xi = S/N(\sqrt{n}/\sigma)$, I can write p as:

$$\begin{aligned} p &= P(S/N > x) \\ &= P(\xi > (x\sqrt{n})/\sigma) \\ &= 2(1 - \Phi(x\sqrt{n}/\sigma)) \\ &= 2(1 - \Phi(aX + b)) \end{aligned} \quad (3.24)$$

where Φ is the cumulative distribution function of the normalised Gaussian variable. I used a Levenberg-Marquardt algorithm (Marquardt, 1963) to fit the above model to the data. Figure 3.11 displays the fit of the empirical PDFs (black lines) to the models (colour lines), obtained for different n_f . Figure 3.11 shows, as expected, that the larger the number of sampling frequencies used, the higher the probability of getting significant high SDE values, thus the false detection probability increases for a given SDE threshold. I note that my implementation of BLS uses a finer frequency sampling (of the order of 10^6), about two orders of magnitude larger than the one used in Kovács et al. (2002), due to the short duration of the transits sought in this work.

Figure 3.11 shows the selected detection threshold of $SDE > 7.3$ (dashed line). This choice corresponds to 10% false alarm probability due to noise. My choice is justified by the relatively small size of the sample of white dwarfs investigated in this work (see chapter 4). However, this false alarm rate might be too high in the case of main-sequence stars where the sample size is considerably larger (millions).

I used the knowledge of the algorithm false alarm rate to define a set of empirical criteria for a transit detection. These criteria allow me to investigate the detection efficiency for my set of synthetic light-curves with injected transit signals. A transit is considered successfully recovered if a peak in the periodogram is within 0.003d of the correct (inserted) period, or is identified as one of its harmonics, and in addition has a value of $SDE > 7.3$.

I used the above criteria to characterise the real detection rate of my implementation of the BLS algorithm in the case of the set of synthetic light-curves containing

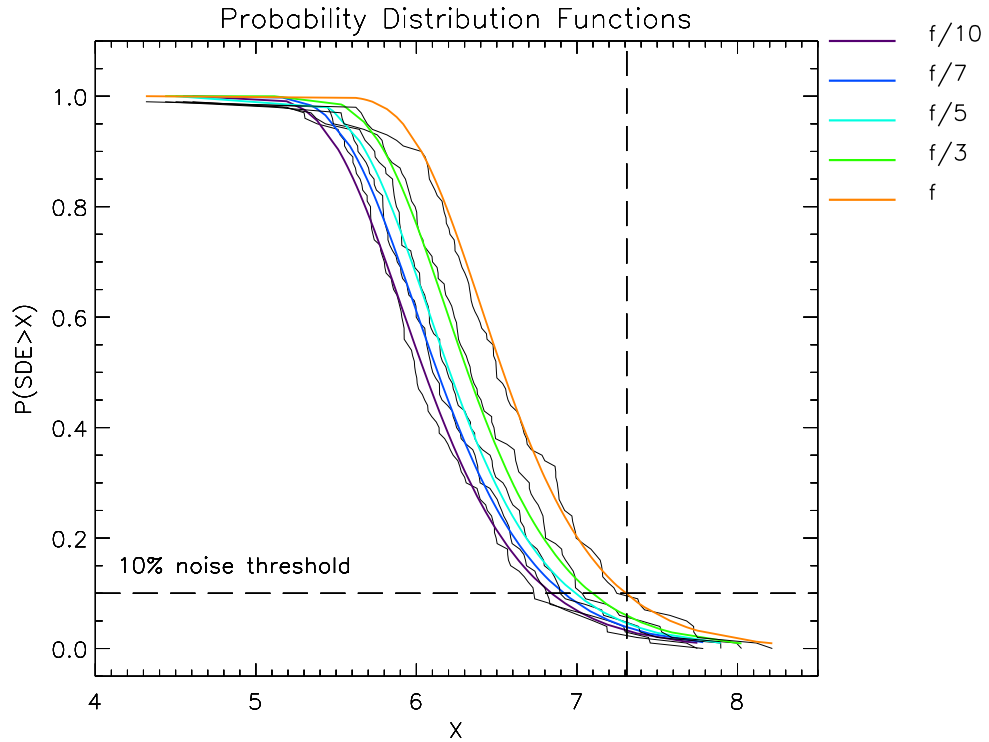


Figure 3.11: Probability distribution functions for different values of the trial frequencies (solid coloured lines) and the relative semi-theoretical fitted models (solid black lines), for light-curves of just random white noise. The y-axis indicates the probability that SDE exceed a given value X , where X (x-axis) is defined by equations 3.22 and 3.21. The number of trial frequencies, n_f defined in equation 3.2, is indicated in the top right corner for each model (colour). For statistically independent frequencies, the larger the frequency band tested the higher is the probability of getting a high SDE value, i.e. a high peak in the BLS power spectrum. The dashed line shows the detection threshold, here set at $7.3SDE$.

injected transit signals covering the parameter space defined in paragraph § 3.2.2.

3.5 Results

I summarise my results in the case of a bright $V \sim 12$ star for transit signals injected into Gaussian random noise data, and red noise data. I show the detection recovery rate for five companion sizes: BD/Gas giant ($10\text{--}12 R_{\oplus}$), the Earth, $0.6 R_{\oplus}$, Mercury ($0.34 R_{\oplus}$) and the Moon ($0.28 R_{\oplus}$), at three randomly chosen, orbital periods in my period window (2h - 15d). Table 3.5 shows from left to right: companion size in R_{\oplus} , orbital period P in (days), transit duration D_{tr} (minutes), d the detection rate of systems with $SDE > 7.3$ (%), d_{bt} the rate of injected systems recovered with SDE values below the detection threshold (%), and d_{notr} , the number of simulated light-curves for which no points were found in transit (%). d_{notr} quantifies in percent the number of synthetic light-curves that, for a given transit zero-point, orbital period and time coverage, happen to have no photometric points covering the transit phase (see the previous discussion concerning the BLS power spectral dependence on the transit phase zero point).

I note that in Table 3.5, for long orbital periods (e.g. > 3.6 days) the BLS detection rates for red noise simulations are higher compared to the white noise case. In addition, in the case of the Moon the detection rate, d , is higher at $P \sim 3.6$ days compared to $P \sim 0.22$ days. This is contrary to expectations. I rather expected to have lower detection rates in the case of red noise. This anomaly is explained by analysing my implementation of the BLS algorithm in more detail.

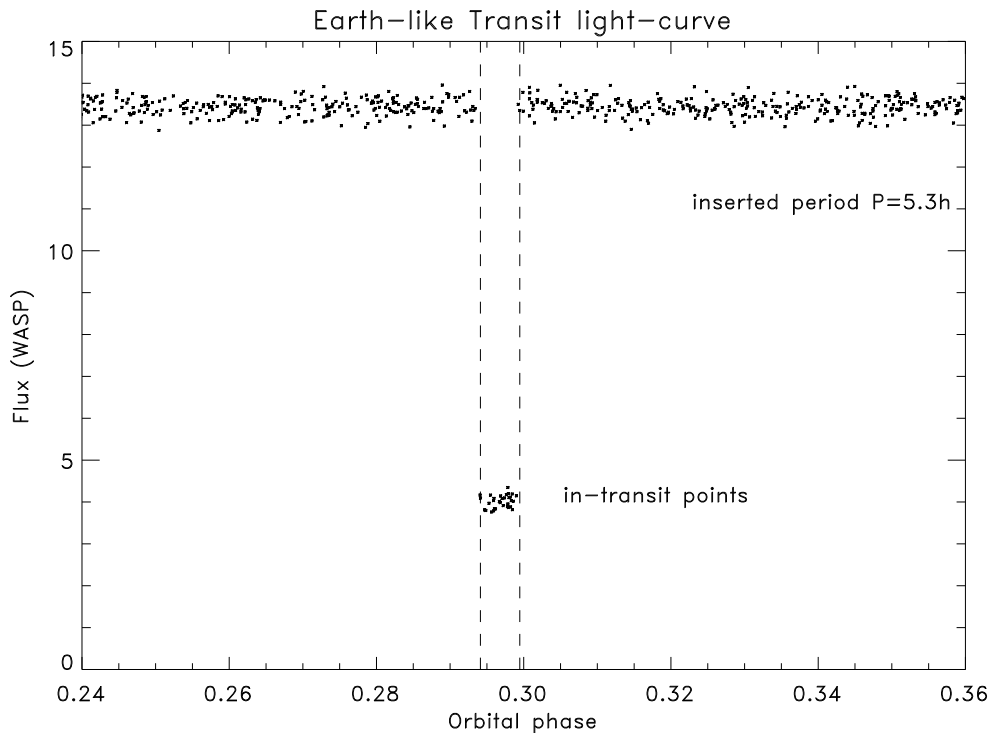


Figure 3.12: Phase folded light-curve for the transit of Earth in ~ 5 h orbit. When the trial period correspond to the inserted period all the in-transit points fall in the transit bin yielding high S/N values. The vertical dashed lines show the bin size for the correct orbital period.

The behaviour of the BLS fitting routine is dominated by effects induced by large signal amplitudes and by my choice to use a fixed grid of transit durations. Consequently, a large number of additional peaks (aliases) of high power are introduced into the BLS power spectra, which can result in false detections.

The expected appearance of a simulated light-curve folded on the right (injected) orbital period is shown in Figure 3.12 for an Earth-sized companion in ~ 5 h orbit. However, when a trial period is not the correct inserted period or one of its harmonics, Figure 3.13 shows the form assumed by the phased light-curve. Although the *in-transit* points are rearranged over the entire phase interval $[0,1]$, they can not be hidden in the scatter of the out-of-transit light-curve. In the case of extra-solar

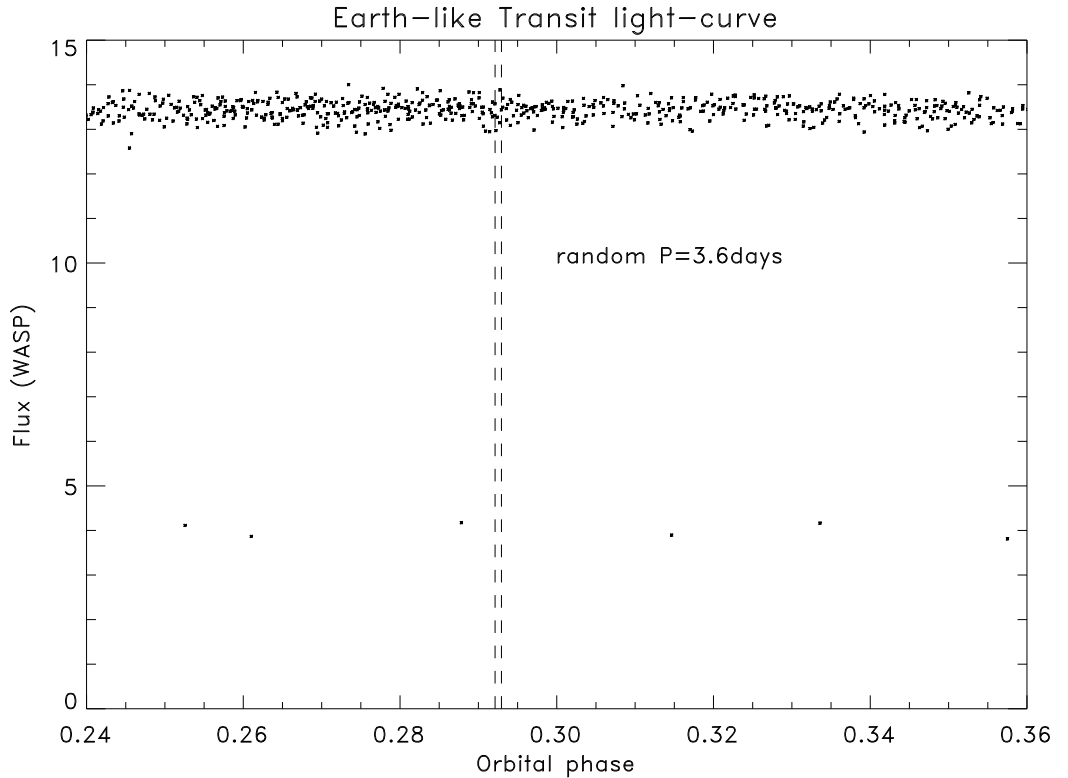


Figure 3.13: Phase folded light-curve for the transit of Earth in ~ 5 h orbit, phased at a random period. Because of the large depth of the transit signal ($\sim 70\%$) multiple bins share some of the in-transit points. This results in non-zero S/N values allocated at wrong periods. The vertical dashed lines show the bin size.

planets around solar-type stars, which have very shallow transits compared to WDs, folding at the *wrong* orbital period produces a flat permutation of the original data resulting in an approximately zero χ^2 value (for my simulations only in the case of Moon-sized objects the transit depth, $\sim 1\text{--}3\%$, is comparable to that of a Hot Jupiter planet around a solar-type star, $\sim 1\%$). For the signals investigated in this work, it is clear from Figure 3.13 that every *wrong* trial period searched, will yield positive χ^2 values corresponding to a non-zero S/N in the periodogram. In addition my implementation of the BLS routine searches for transits of short durations over a fixed grid of $D_{tr} = 1, 2, 4, 8, 16, 32$ minutes, which results in large numbers of bins

partitioning the phase folded light-curve (where $n_{bins} = P/D_{tr}$) (see Figure 3.13). Because the number of points in the transit bin decreases with increasing orbital period for the same transit duration, the χ^2 evaluations over bins containing no points in-transit, will have increasingly higher statistical significance. This increases the value of the S/N allocated to intermediate and long (hour to day) trial periods (see Figure 3.14), and explains the sometimes higher detection rates observed at long orbital periods for the red noise simulations listed in Table 3.5). At the far end of the period range searched, the numbers of bins becomes so high ($n_{bins} = P/D_{tr}$) that individual bins contain only a few points. The step-like structure which appears at long periods in the BLS periodogram as shown in Figure 3.14, is due to subsequent in-transit points jumping out of a bin. Thus, different permutations of the phased light-curve may have equal numbers of bins containing the same number of in-transit points, resulting in equal S/N values. In the limit at which as little as 2 points fall within a bin the χ^2 calculations are no longer reliable, with instabilities arising for bins containing less than 5 points (Wall & Jenkins, 2003).

In addition to the problems highlighted above, SuperWASP red noise light-curves have a residual correlated noise component. Consequently spurious periods can achieve even higher statistical significance, in particular for periods which are in any way correlated to one day and its harmonics (SuperWASP data are severely affected by the day-night alternation). Last but not least, I note that to simulate the effect of red noise I have used a set of real SuperWASP light-curves in which I injected simulated transit signals. As a result, small differences in the time baseline of individual light-curves and differences in the data quality also play a rôle in adding extra noise components. This might be important for the transits of rocky bodies of sizes similar to the Moon, for which the number of detections strongly depends

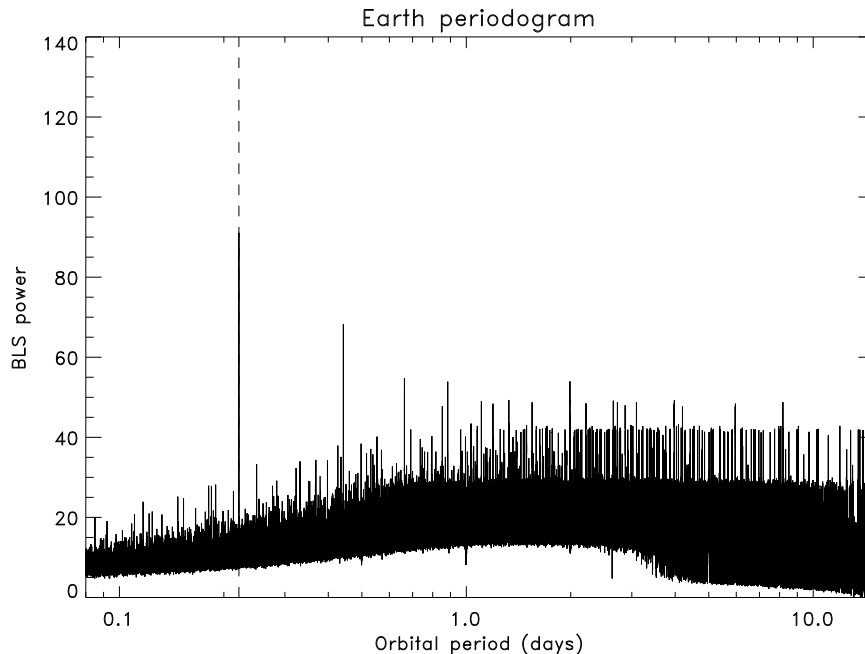


Figure 3.14: BLS power spectrum for the transit signal of an Earth in orbit with ~ 5 h period. While the correct (inserted) period is recovered, strong aliasing and noise structure are present, particularly at long periods, see text for a detailed discussion.

on the χ^2 values near the detection threshold. In these cases even a change in χ^2 of 5% can have significant effects on the inferred detection probability. Table 3.5.1 shows the detection rate for a rocky body, with a radius similar to the Moon, but with a change of 5% in the value of the detection threshold. I define O_{TH} to indicate the detection rates (d , d_{bt} , d_{notr} as defined in Table 3.5) obtained with the original threshold of $SDE > 7.3$ and I define M_{TH} to indicate the modified detection rates obtained when using a threshold of $O_{TH} \times 1.05$. Table 3.5.1 shows that the change in χ^2 is sufficient to drastically reduce the BLS detection sensitivity.

;

Table 3.1: Results from simulations using the first implementation of the BLS routine, for five companion sizes: BD/Gas giant, the Earth, 0.6×Earth, Mercury and the Moon, for three, randomly chosen, orbital periods in the period window, for white and red noise simulations. In both cases d is the detection rate of systems with $SDE > 7.3$ (%), d_{bt} is the rate of injected periods with SDE below the detection threshold (%) and d_{notr} the number of simulated light-curves for which no points were found in transit (%).

<i>Size</i>	R_{pl} R_{\oplus}	P (days)	D_{tr} (min)	White noise			Red noise		
				d	d_{bt} (%)	d_{notr}	d	d_{bt} (%)	d_{notr}
BD-Gas Giant	10-12	0.08	6.65	100	0	0	99	1	0
”	”	3.60	19.88	100	0	0	99	1	0
”	”	14.72	32.18	78	22	0	83	17	0
Earth	1	0.22	1.70	100	0	0	98	2	0
”	”	3.60	4.21	77	22	1	81	19	0
”	”	14.72	6.82	5	93	2	21	47	2
0.6Earth	0.6	0.22	1.42	100	0	0	64	36	0
”	”	3.60	3.51	69	27	4	27	73	0
”	”	14.72	5.69	3	88	9	7	84	9
Mercury	0.45	0.22	1.32	100	0	0	8	92	0
”	”	3.60	3.25	63	34	3	5	94	1
”	”	14.72	5.26	2	89	9	3	88	9
Moon	0.27	0.22	1.19	80	20	0	0	100	0
”	”	3.60	2.94	3	94	3	2	98	0
”	”	14.72	4.76	0	89	11	0	86	14

3.5.1 Optimised BLS implementation

In order to improve the performance of my implementation of the BLS algorithm I have developed a modified version of the previous routine. I used the same grid of frequencies as defined in equations 3.1 to 3.3, but I adopted a logarithmic frequency step compared to the fixed step used before. The difference between the frequencies sampled is chosen such that the accumulated phase difference between successive trial frequencies, over the full dataset, corresponds to the width of the transit at the longest period searched. This accounts for the oversampling at short periods and allows me to match more closely the model box-function to the expected transit signal for each orbital period searched. For the χ^2 evaluation I used only phase-bins which contain at least five photometric points. In addition, I have only selected transits for which at least five distinct eclipses were observed over the entire observations (~ 120 – 150 days per season for a typical SuperWASP light-curve). Because the majority of the spurious structure in the BLS periodogram is due to the large amplitude of the transit signals, I have introduced an additional down-weighting method applied on a per bin base. The down-weighting is performed at the time of the calculation of the $\Delta \chi^2$ (see equation 3.9) in the transit bin and consists of:

$$S/N = \frac{\delta}{\sqrt{\text{Var}(\delta) + \tilde{w}^2}}, \quad (3.25)$$

where \tilde{w} is the root mean square (*rms*) of the differential magnitudes inside the transit bin. The down-weighting adds an extra term in the calculation of the signal-to-noise value (see e.g. equation 3.10) of the transit event and reduces the S/N allocated to bins which contain a mixture of in-transit and out-of-transit points.

This should account for the spread of the in-transit points over different bins in the folded time series in the case of periods which are not the correctly inserted period (see Figure 3.13). At the correct orbital period all the in-transit points should be found in the same bin resulting in higher values of S/N . In order to investigate the sensitivity of this version of the BLS routine I tested the algorithm response for pure white noise light-curves. I found that my optimisation of the BLS can achieve lower SDE threshold values for detection when using the same sample of trial frequencies as before. Figure 3.15 shows the PDFs (black curve) from data and in colour the fitted model as derived in § 3.3.2. The detection threshold indicated by the dashed line is reduced to $6.3SDE$ (compared to $7.3SDE$ before). I have analysed the set of simulated transit light-curves using the same empirical criteria for detection as derived in § 3.4 but now using the detection threshold obtained above. The optimised BLS implementation yields much cleaner periodograms where the structure seen in Figure 3.14 is significantly suppressed. In addition, the SDE values of detected transit signals have higher statistical significance. Figure 3.16 shows the BLS power spectrum for the same transit of Figure 3.12. I recover the same transit signal, the periodogram is clean, and the detection has a much higher S/N value. However, because I have more stringent requirements on the number of points per bin (≥ 5) and the number of observed transits per light-curve (≥ 5) the probability of detecting long periods transits is strongly reduced.

I summarise the results obtained using the optimised version of the BLS algorithm in Table 3.3. Table 3.3 shows the cut-off in the detection rate at long periods and for small companion sizes. Indeed, companions as small as the Moon can have very short transit durations (Figure 3.2), and this may result in not enough in-transit points in a synthetic light-curve. This is also illustrated in Figures 3.17 and 3.18 which show

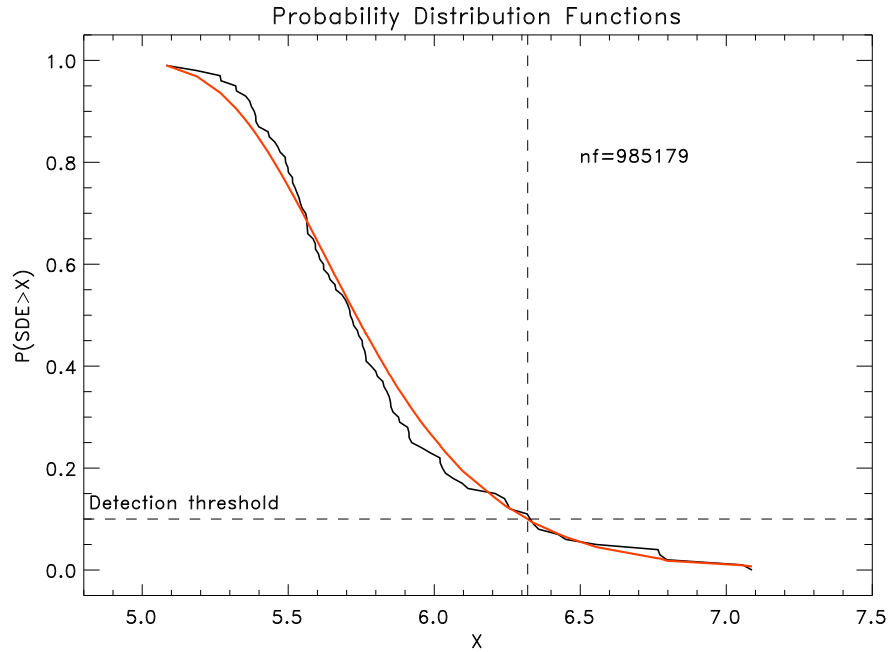


Figure 3.15: PDF function for the modified-optimised BLS routine. The dashed-line shows the new detection threshold $6.3SDE$ for a 10% noise contribution.

the SDE values for the transiting system recovered using my implementation of the BLS algorithm, plotted against the orbital period of the recovered systems. Figure 3.17 shows the detection limits for sub-stellar and planetary companions to a white dwarf of magnitude $V \sim 12$. Figure 3.18 illustrates the same for a white dwarf of $V \sim 13$ and $V \sim 15$. Small planetary companions in long period systems have SDE values below the selected detection threshold of $6.3SDE$ and consequently are not detected.

Finally, I note that the SDE values for the transit signals of the simulated systems in the case of red noise are more than three times lower than the one estimated using the naïve assumption of Gaussian random noise, as expected from the discussion in paragraph § 3.3.

The results obtained from my simulations show that in the case of Gaussian random noise my implementation of the BLS routine is sensitive to the transit of a Moon-

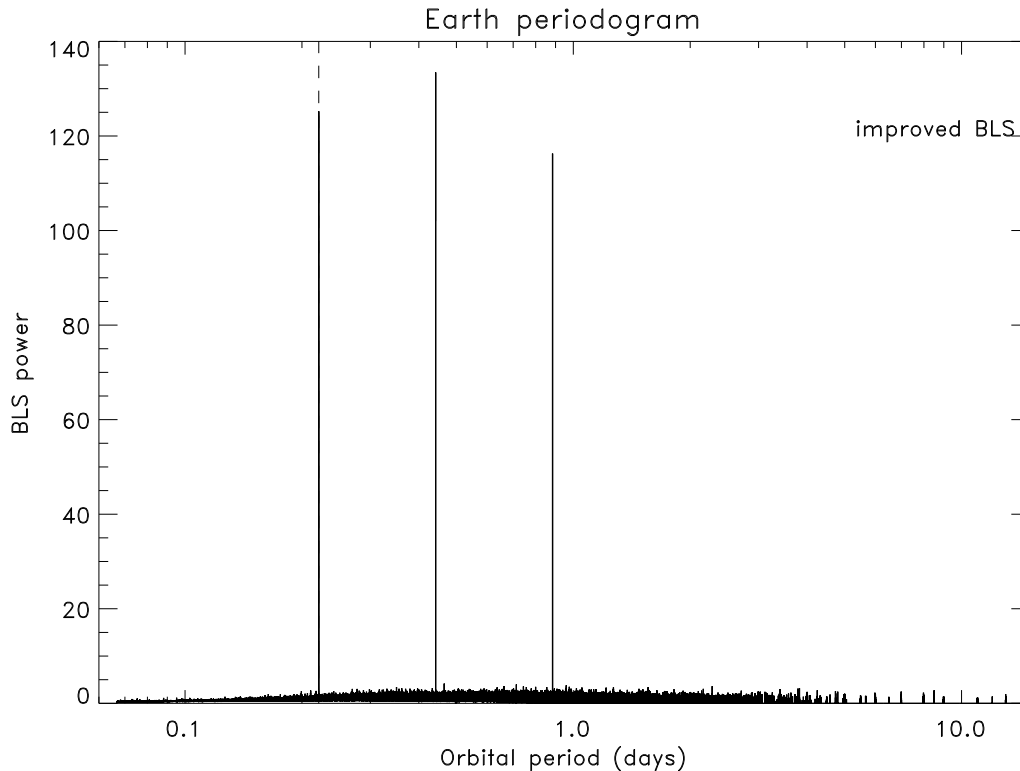


Figure 3.16: BLS power spectrum as in Figure 3.14 obtained with the improved BLS routine. I show that for the same transit signal I achieve higher S/N values and higher statistical significance (i.e. higher SDE values). The noise structure present in Figure 3.14 is importantly reduced.

sized companion orbiting a $V \sim 12$ white dwarf. For fainter stars only increasingly larger rocky bodies can be detected. The improvements I have obtained upon the BLS routine, allows me to achieve high detection rates of higher S/N values, even in the case of correlated noise in the data. However, as expected in the presence of red noise I obtained lower detection rates compared to the case of uncorrelated (white) noise. This is in agreement with the prediction based on white noise data (see e.g. § 3.3). Nevertheless, even in the presence of residual noise I find that Earth-sized companions remain readily detectable even in low signal-to-noise light-curves. For good quality data in the case of bright white dwarfs ($V \sim 12$) Mars-sized companions and even smaller Mercury-like planets could be detected in SuperWASP

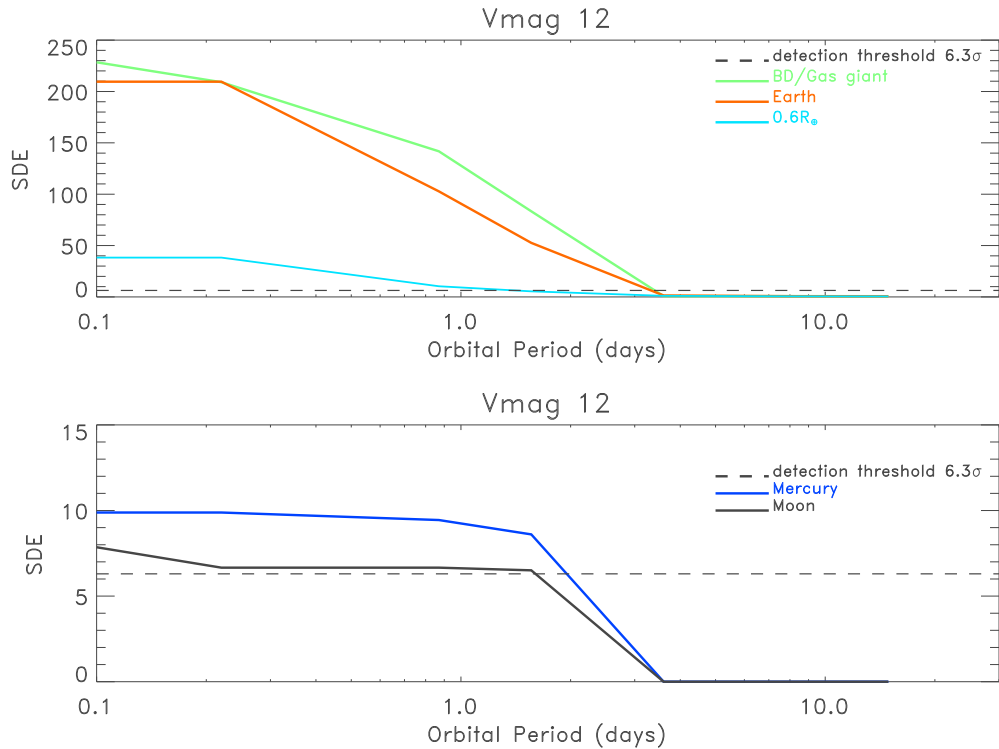


Figure 3.17: SDE values for the simulated transit signals recovered by my BLS algorithm in the case of red noise simulations. The Simulations cover companions ranging from the Moon size to Jupiter or brown dwarf sizes orbiting a $V \sim 12$ white dwarf. The lower-panel shows that for a bright $V \sim 12$ WD bodies as small as Mercury and even the Moon can have transit signals detectable in good S/N light-curves.

light-curves as shown from the results of my simulations (Table 3.3). In addition, my results have been obtained simulating transit light-curve with a time span of a typical SuperWASP season (120–150 days). Thus, an analysis of light-curves covering multiple SuperWASP season might increase S/N values of transit signals and thus my detection rate, as more distinct eclipses can be observed (see also Smith et al. 2006).

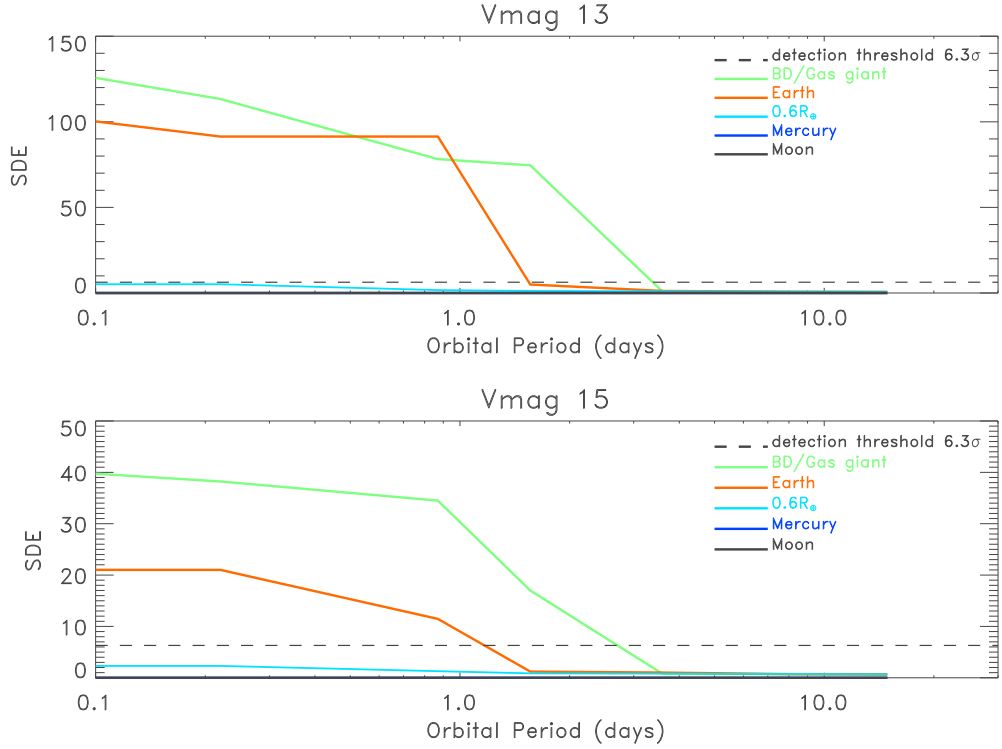


Figure 3.18: SDE results as in Figure 3.17 but for a white dwarf of magnitude $V \sim 13$ and $V \sim 15$. For fainter magnitudes WDs increasingly higher radius rocky bodies are detectable. However, the Figure shows that Earth size companions and even smaller bodies remain readily detectable.

Table 3.2: The detection rate for a transit of a Moon-sized rocky body when 5% change in the detection threshold is considered. This results in a drastic reduction of the BLS detection sensitivity. O_{TH} indicates the detection rates (d , d_{bt} , d_{notr}) obtained with a detection threshold of $7.3SDE$, M_{TH} indicates the detection rates obtained when using a modified detection threshold of $1.05 \times O_{TH}$. d , d_{bt} and d_{notr} are defined as in Table 3.5.

$Size$	R_{pl} R_{\oplus}	P (days)	O_{TH}			M_{TH}		
			d	d_{bt} (%)	d_{notr}	d	d_{bt} (%)	d_{notr}
Moon	0.27	0.08	80	20	0	37	63	0
"	"	3.48	3	94	3	0	97	3
"	"	14.72	0	89	11	0	89	11

3.6 Conclusions

I have investigated the characteristics and detection limits for sub-stellar and terrestrial companions to white dwarfs in the SuperWASP survey. I have used SuperWASP photometric data to create a set of synthetic light-curves for simulations performed in the case of white and red noise. Using my first implementation of the BLS algorithm I found that the behaviour of the BLS was compromised by the characteristics of the signals simulated here. In order to better account for the large amplitudes and very short durations of the transit events I have modified the BLS algorithm. The new optimised version of the BLS allowed me to obtain higher signal-to-noise values by reducing importantly the red noise and the large signal depths contribution to aliases in the BLS periodograms. My final results show that in the case of white Gaussian noise my modified BLS code is sensitive to rocky bodies of sizes comparable to the Moon. Although the BLS detection sensitivity is reduced for red noise data, nevertheless, I find that Earth-sized companions to white dwarfs are readily detectable and even Mercury sized bodies are detectable, at an acceptable level, in good quality data from current ground-base photometric surveys such as SuperWASP.

In the work carried out here I have pushed the BLS algorithm to its limit of applicability. Kovács et al. (2002) firstly developed the routine to detect the transit signals of Hot Jupiter planets orbiting solar-type stars. The characteristics of the transit light-curves of known extra-solar planets cover a different set of parameters compared to the signals of the systems subject to my investigation. I have modified the routine by introducing a down-weighting scheme that helps account for the

shape of the phased time series of my dataset (see Figure 3.13). However, I suggest that more than one algorithm should be used to certify a transit detection. A suitable alternative solution may be offered by the “Rayleigh test” (see Kruger et al. 2002, and references therein) which could account for the large depth of the signal simulated in this work.

The Rayleigh test searches for periodicities in time series by detecting a preferred direction in circular data spanning angles from 0 to 2π . For a light-curve of m photometric points recorded at arrival times t_i with $i = 0, \dots, m$ the Rayleigh test evaluates the phase value of each point for a trial frequency f as follows:

$$\phi_i = 2\pi ft_i. \quad (3.26)$$

Each event is considered to identify a unit vector of components $(\cos\phi_i, \sin\phi_i)$, then the sum of all vectors (mR) will line up if there is a preferred phase in the data. The Rayleigh power is calculated as:

$$R(f_i) = \frac{1}{m} \left[\sum_{i=1}^m \sin(2\pi ft_i) \right]^2 + \frac{1}{m} \left[\sum_{i=1}^m \cos(2\pi ft_i) \right]^2. \quad (3.27)$$

If the analysis of $R(f_i)$ has a large magnitude for a particular trial period, a periodic signal maybe present at that period. The Rayleigh test has been extensively used to search for periodic signals, an example of its application is the analysis of time-tagged event data from observations of gamma-ray bursts (Kruger et al. 2002).

The key argument of the Rayleigh test is to look for periodicities in the light-curve arrival times, whereas the BLS algorithm identifies periodicities related to detectable

changes in the values of the light-curve flux. A different approach would be to first isolate the hypothetical points in-transit by σ -clipping the mean light-curve points to identify all the outliers. Then, the Rayleigh test can be used to look for periodicities in the arrival times of these outliers. This approach could be applied to identify the presence of transit signals of large depths appropriate for this work. However, the BLS routine remains a very powerful algorithm for the detection of the signature of very shallow transits as in the case of extra-solar planets around solar-type stars. Finally, for the shape and characteristics of the transit signals studied in this work, a combined approach which uses the above idea and the BLS algorithm may yield higher detection rates.

Table 3.3: Detection efficiency for the new optimised implementation of the BLS algorithm. From left to right I list the companion size, the SuperWASP magnitude V_{mag} , the orbital period P and the results obtained for red noise simulations compared to the white noise case. The detection rate d, d_{bt} and d_{notr} are described in Table 3.5.

size	V_{mag}	P (days)	White noise			Red noise		
			d	d_{bt}	d_{notr}	d	d_{bt}	d_{notr}
			(%)			(%)		
BD	12	0.08	100	0	0	100	0	0
”	”	0.22	100	0	0	100	0	0
”	”	0.87	100	0	0	100	0	0
”	”	1.56	99	1	0	98	2	0
”	”	3.60	24	25	0	21	32	0
”	”	8.30	0	0	0	0	0	0
”	”	14.7	0	0	1	0	0	1
BD	13	0.08	100	0	0	100	0	0
”	”	0.22	100	0	0	100	0	0
”	”	0.87	100	0	0	100	0	0
”	”	1.56	95	2	0	98	0	0
”	”	3.60	24	25	0	6	31	0

Continued on next page

Table 3.3 – continued from previous page

size	V_{mag}	P (days)	White noise			Red noise		
			d	d_{bt}	d_{notr}	d	d_{bt}	d_{notr}
			(%)			(%)		
”	”	8.30	0	5	0	0	7	0
”	”	14.7	0	0	1	0	1	0
BD	15	0.08	100	0	0	100	0	0
”	”	0.22	100	0	0	100	0	0
”	”	0.87	100	0	0	100	0	0
”	”	1.56	98	0	0	91	3	0
”	”	3.60	4	33	0	8	44	0
”	”	8.30	0	5	0	0	8	2
”	”	14.7	0	0	1	0	2	0
Earth	12	0.22	100	0	0	100	0	0
”	”	0.87	76	5	0	67	10	0
”	”	1.56	48	19	0	37	30	0
”	”	3.60	5	7	0	2	4	0
”	”	8.30	0	0	7	0	0	7
”	”	14.7	0	0	6	0	0	6
Earth	13	0.22	100	0	0	100	0	0
”	”	0.87	74	11	0	64	6	0
”	”	1.56	37	30	0	21	17	0

Continued on next page

Table 3.3 – continued from previous page

size	V_{mag}	P (days)	White noise			Red noise		
			d	d_{bt}	d_{notr}	d	d_{bt}	d_{notr}
			(%)			(%)		
”	”	3.60	2	34	0	3	36	0
”	”	8.30	0	4	7	0	5	7
”	”	14.7	0	0	6	0	2	6
Earth	15	0.22	100	0	0	100	0	0
”	”	0.87	65	11	0	66	8	0
”	”	1.56	37	30	0	6	43	0
”	”	3.60	2	34	0	1	49	0
”	”	8.30	0	4	7	0	7	8
”	”	14.7	0	0	6	0	1	6
0.6Earth	12	0.22	98	2	0	96	4	0
”	”	0.87	44	14	0	41	6	0
”	”	1.56	31	17	3	20	19	3
”	”	3.60	3	2	1	2	1	1
”	”	8.30	0	0	15	0	0	15
”	”	14.7	0	0	12	0	0	12
0.6Earth	13	0.22	84	1	0	55	29	0
”	”	0.87	42	11	0	16	26	0
”	”	1.56	15	20	0	4	53	3

Continued on next page

Table 3.3 – continued from previous page

size	V_{mag}	P (days)	White noise			Red noise		
			d	d_{bt}	d_{notr}	d	d_{bt}	d_{notr}
			(%)			(%)		
”	”	3.60	3	35	1	2	37	1
”	”	8.30	0	5	16	0	4	15
”	”	14.7	0	2	15	0	0	12
0.6Earth	15	0.22	10	18	0	0	9	0
”	”	0.87	7	17	0	0	27	0
”	”	1.56	4	44	0	0	52	3
”	”	3.60	1	50	1	0	36	1
”	”	8.30	0	7	20	0	4	15
”	”	14.7	0	1	13	0	0	12
Mercury	12	0.22	86	6	0	78	2	0
”	”	0.87	25	26	0	24	19	0
”	”	1.56	12	14	3	8	9	3
”	”	3.60	2	0	1	0	0	1
”	”	8.30	0	0	17	0	0	17
”	”	14.7	0	0	15	0	0	15
Mercury	13	0.22	22	19	0	0	8	0
”	”	0.87	16	15	0	0	26	0
”	”	1.56	13	22	0	0	51	3

Continued on next page

Table 3.3 – continued from previous page

size	V_{mag}	P (days)	White noise			Red noise		
			d	d_{bt}	d_{notr}	d	d_{bt}	d_{notr}
			(%)			(%)		
”	”	3.60	1	35	2	0	35	1
”	”	8.30	0	4	19	0	4	17
”	”	14.7	0	2	17	0	0	15
Mercury	15	0.22	5	8	0	0	8	0
”	”	0.87	5	18	0	0	26	0
”	”	1.56	3	45	0	0	50	3
”	”	3.60	0	49	1	0	35	1
”	”	8.30	0	6	21	0	4	17
”	”	14.7	0	1	14	0	0	15
Moon	12	0.22	38	13	0	4	26	0
”	”	0.87	12	24	0	1	30	0
”	”	1.56	4	33	3	1	37	3
”	”	3.60	0	0	1	0	0	1
”	”	8.30	0	0	21	0	0	21
”	”	14.7	0	0	18	0	0	18
Moon	13	0.22	12	8	0	0	8	0
”	”	0.87	8	15	0	0	26	0
”	”	1.56	3	23	0	0	50	3

Continued on next page

Table 3.3 – continued from previous page

size	V_{mag}	P (days)	White noise			Red noise		
			d	d_{bt}	d_{notr}	d	d_{bt}	d_{notr}
			(%)			(%)		
”	”	3.60	0	35	5	0	35	1
”	”	8.30	0	4	20	0	4	21
”	”	14.7	0	2	19	0	0	18
Moon	15	0.22	4	7	0	0	8	0
”	”	0.87	4	18	0	0	26	0
”	”	1.56	1	43	0	0	49	3
”	”	3.60	0	49	4	0	35	1
”	”	8.30	0	6	24	0	4	21
”	”	14.7	0	0	17	0	0	18

Chapter 4

Data analysis

Abstract

The simulations explored in chapter 3, show that sub-stellar objects and even smaller planetary companions to white dwarfs have eclipses and transit signals detectable in SuperWASP light-curves. Encouraged by my results I have investigated the possibility of detecting the signal of any such system in a sample of nearby white dwarfs brighter than $V \sim 15$ for which I have SuperWASP data. I have searched for eclipses and transits signals in my sample of 194 white dwarfs, resulting from the cross-correlation of the McCook & Sion catalogue and the SuperWASP data archive. I used my own implementation of the Box-fitting routine as describe in chapter 3. In addition, I visually inspected the light-curve of each star in the sample. This study found no evidence for transits due to sub-stellar or terrestrial companions to stars in my sample. I used this key result to obtain an upper limit to the frequency of sub-stellar and planetary companions around white dwarfs.

WD sample sky coverage

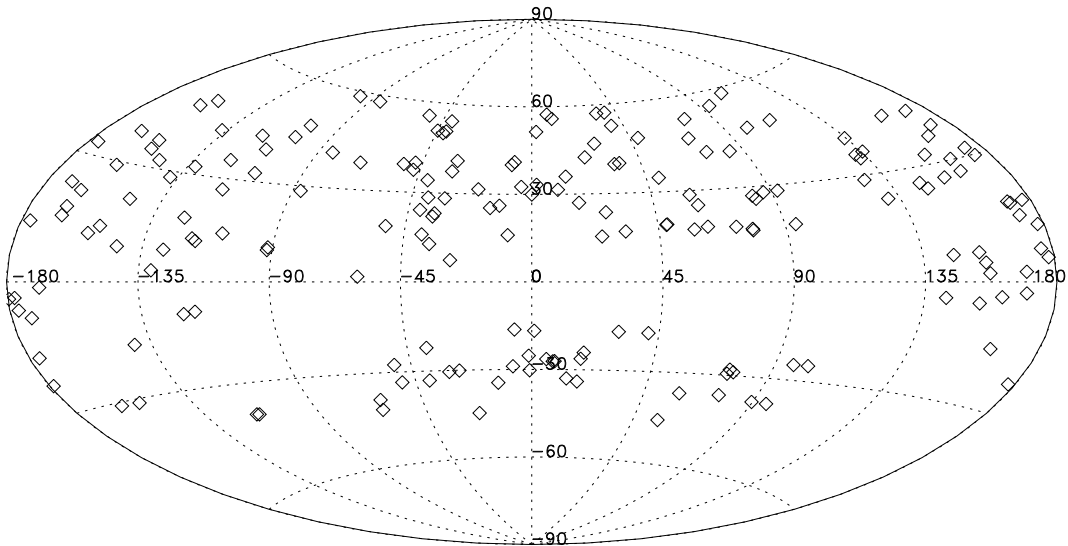


Figure 4.1: Sky coverage for the 194 stars in my sample of white dwarfs observed by SuperWASP.

In the following I describe the selection method used to identify the white dwarf sources incorporated in the final target sample, the results obtained from the transit search by means of my BLS routine and the visual inspection of the light-curves. I finally discuss the implications of my null result and estimate an upper limit for the frequency of sub-stellar and terrestrial companions to white dwarfs.

4.1 White Dwarfs in the SuperWASP archive

My sample of white dwarf targets consists of all objects resulting from a cross-correlation of the McCook & Sion catalogue (McCook & Sion, 2003) and the Su-

perWASP data archive. The total number of matched sources is 347. In order to maximise my detection probability I have used light-curves de-trended by means of the Tamuz algorithm (Tamuz et al. 2005). As described in chapter 2, the Tamuz algorithm is very efficient in removing sources of systematic errors from the data (red noise), thus increasing the signal-to-noise of a transit signal. Of the 347 SuperWASP objects I only considered sources with more than ~ 600 photometric data points per light-curve. This is equivalent to a minimum of ~ 11 observing nights, for a night of ~ 8 hours and a sampling cadence of ~ 8 – 10 minutes. In this way, all selected sources, have sufficient numbers of observations to allow the successive observations of individual planetary eclipses. This selection reduces the number of SuperWASP targets to 213. In addition, I have analysed each individual light-curve and applied a data quality test to reject data of very poor quality. Because of the very large signal amplitudes of the systems investigated here, chapter 3, § 3.2.1, I do not remove the light-curve outliers by sigma-clipping, instead I identify and reject bad quality observations. These photometric points have large associated errors and only contribute to the residual noise component. The quality test used evaluates the value q_i for every photometric measurement in a light-curve using the individual magnitude errors $\tilde{\sigma}_i$ added in quadrature to the estimated systematic errors $\sigma_{t(i)}$ introduced into individual frames by for example, passing clouds, Sahara-dust and other transient phenomena which degrade the extinction correction (see e.g. Collier Cameron et al. 2006). Thus q_i is obtained as:

$$q_i = \sqrt{(\sigma_{t(i)}^2 + \tilde{\sigma}_i^2)} \quad (4.1)$$

where $\tilde{\sigma}_i$ are individual magnitude errors calculated as:

$$\tilde{\sigma}_i = \frac{2.5}{\ln(10)} \left(\frac{F_i}{\sigma_i} \right), \quad (4.2)$$

where F_i are the individual flux measurements and σ_i are the relative photometric errors. SuperWASP magnitudes are calculated as:

$$\text{mag}_i = -2.5 \text{Log}_{10} \left(\frac{F_i}{10^6} \right), \quad (4.3)$$

where the denominator in the log function gives the magnitude zero-point in μVega . Visual inspection of the 213 light-curves shows that points with $q_i \geq 0.3$ can be rejected and are associated with nights in which the observational conditions are poor (e.g. bright sky due to Moon light, poor seeing, etc.). For each light-curve I have selected only photometric points for which q_i is ≤ 0.3 . As a result the number of SuperWASP targets with more than 600 photometric points is further reduced to 200. Among the 200 stars, I find six duplicate SuperWASP counterparts to the same McCook & Sion targets. This can be related to the characteristics of the USNO-B1 catalogue (Monet et al., 2003), used by the SuperWASP pipeline to perform the fields astrometric solution (see chapter 2, § 2.4; and Pollacco et al. 2006). Firstly, the USNO-B1 catalogue contains spurious entries caused by optical artifacts related to diffraction spikes and reflection halos in the original imaging data (for more details see Barron et al. 2008). Secondly, because of the large SuperWASP pixel size ($13.7'' \text{ pixel}^{-1}$), in some cases the duplicate SuperWASP sources can be due to real individual entries in the USNO-B1 catalogue. In such cases both stars are detected in the same SuperWASP pixel and can not be separated. Here I have selected the brightest of the two SuperWASP entries and/or the one which had either the longest duration or the greatest number of points. I considered, where possible, data with

multi-season observations ranging from 2004 up to 2008. This allows me to increase the *signal-to-noise* (see equation 3.10 from chapter 3) and thereby increase my detection probability. My final sample contains 194 SuperWASP unique matches to the McCook & Sion catalogue white dwarfs. The stars in the sample are distributed over both hemispheres, north and south, with the majority in the north. Figure 4.1 shows the sky coverage for the 194 stars in my sample.

My sample covers magnitudes in the range $V \sim 9$ to $V \sim 15$. SuperWASP can achieve high photometric precision $< 1\%$ for sources brighter than $V \sim 12$ while for increasingly fainter sources the photometric precision becomes increasingly lower. Figure 4.2 shows the quality of four SuperWASP light-curves for magnitudes $V \sim 10, 12, 13, 15$. Figure 4.2 illustrate the data quality after de-trending with the Tamuz algorithm and after I applied my quality test. However, residual systematic trends can still be present in the data in particular at periods connected to the day-night alternation and/or connected for example to residual Moon-light variation. This is the case of star 1SWASP J0222440.83+400823.0, Figure 4.2 top-left panel ($V \sim 10$). The star light-curve shows brightness variations and low photometric points, outliers, however, a detailed analysis of the light-curve by means of the BLS algorithm and by visual inspection did not find evidence of companions. SuperWASP photometric precision decreases for fainter magnitude stars and for white dwarfs close to the SuperWASP faint magnitude limit ($V \sim 15$) SuperWASP photometric precision is $\sim 10\%$, see for example Figure 4.2 lower-right panel. The scatter in the data around the mean light-curve is $\sigma = 0.12 \simeq 12\%$. This is roughly equivalent to the amplitude of a transit signal due to a body of size comparable to or greater than Mercury (see chapter 3, Figure 3.2, lower panel), and in some cases

can preclude transit detection.

I present the entire list of 194 sources in Table 4.1. I have used the BLS implementation described in chapter 3, § 3.4.1 to search for eclipses and transit signals. To date I find no evidence for transiting sub-stellar or planetary companions for the stars in my sample. Table 4.1 summarises my results. For each entry I quote the SuperWASP identifier (1SWASP), the WD name (McCook & Sion, 2003), the SuperWASP magnitude (as from equation 4.3) and the number of photometric points in the light-curve (N).

4.2 Visual inspection of SuperWASP light-curves

As well as using the Box-fitting algorithm I also visually inspected each individual light-curve in the sample. The transit signal of systems subject to this study are expected to have very short transit durations (as short as ~ 1 minute, see Figure 3.2). This might be equivalent to one individual photometric point, periodically dropping in a light-curve. Therefore, visual inspection of individual light-curves can help to identify the signature of a transit event from a non-detection. Figure 4.3 shows an example of a simulated transit event. The top-left panel shows the simulated transit light-curve of an Earth-sized companion injected with an orbital period of ~ 3.6 days. The top-right panel shows a magnified version of this Figure, in the vicinity of a transit event (highlighted in red). Bottom-left and right panels, as above but in this case plotting fluxes versus integer numbers, which allows removal of time gaps in the light-curve due to the day and night alternation, bad weather etc. In this way I can easily identify light-curves which might have interesting features. For example, eye-

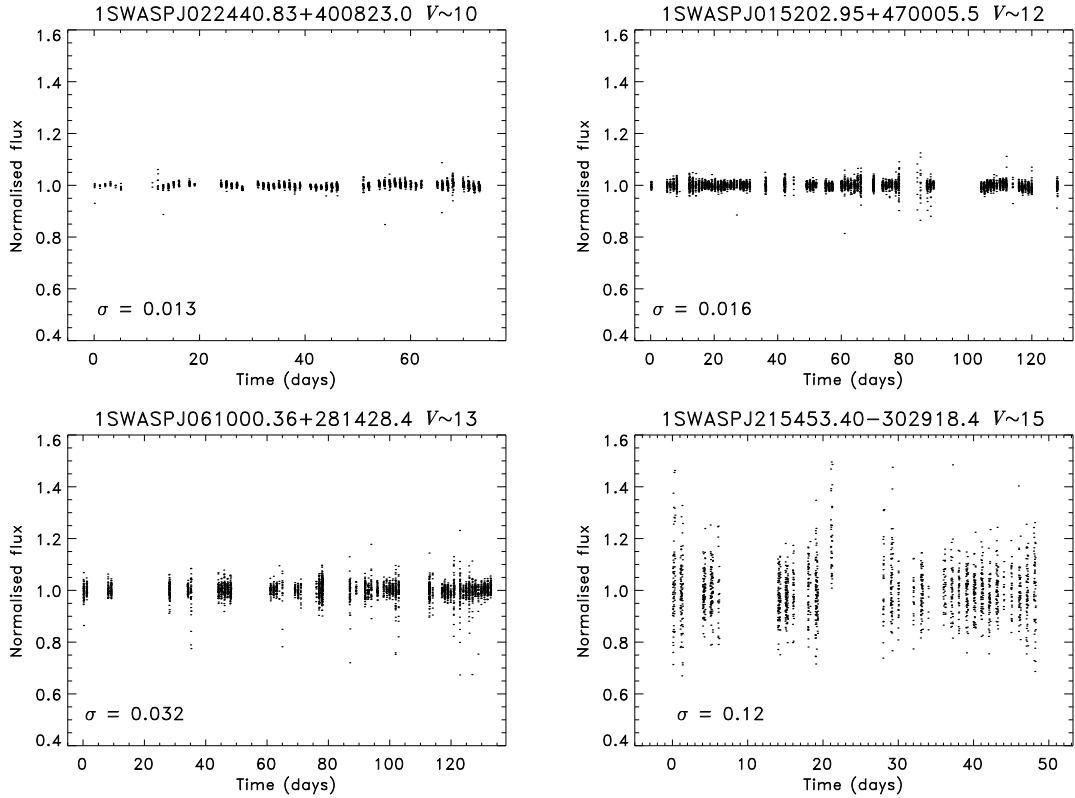


Figure 4.2: Four examples of white dwarf targets among the sample of 194 stars. From top-left to bottom-right I plot the sources 1SWASP J022440.83+400823.0 ($V \sim 10$), 1SWASP J015202.95+470005.5 ($V \sim 12$), 1SWASP J061000.36+281428.4 ($V \sim 13$), 1SWASP J215453.40-302918.4 ($V \sim 15$). The four panels illustrate SuperWASP photometric precision for four magnitudes ranges covering the magnitudes of white dwarfs in the SuperWASP archive. The light-curves are plotted after de-trending by means of the Tamuz algorithm and after the application of my data quality test. Nevertheless, residual are still present in the data as illustrated in the top-left panel. These residuals can be due to the day-night alternation and/or residual Moon-light variations. I note that outliers are present in the plotted light-curves. However, a detailed analysis of these targets (BLS + visual inspection) found no evidence of companions.

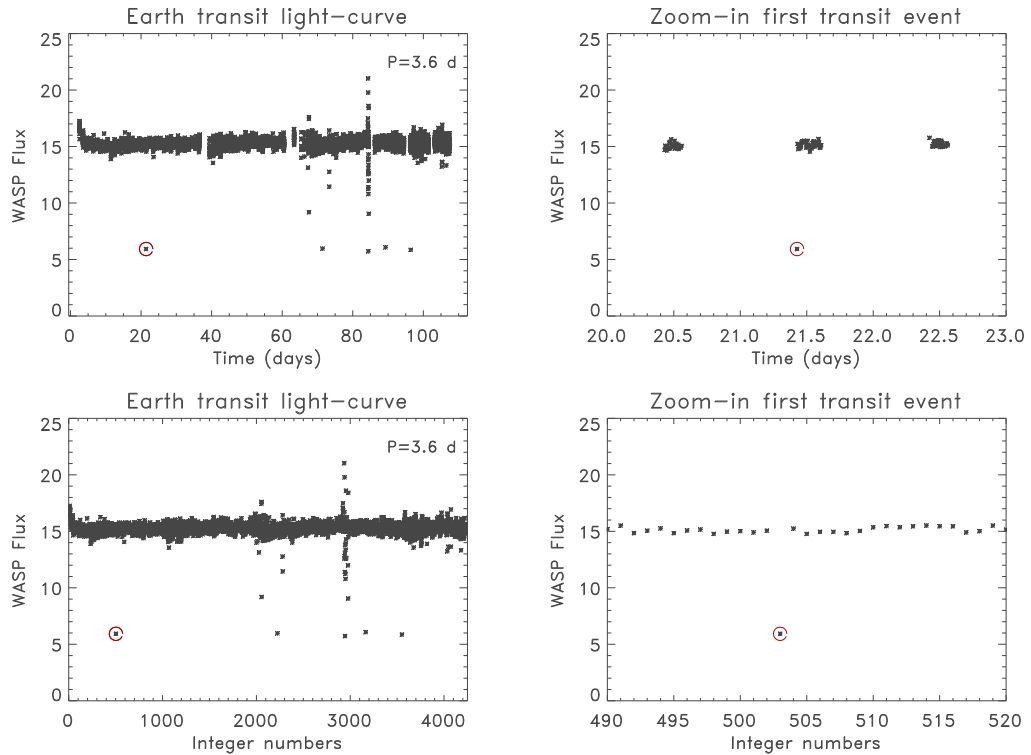


Figure 4.3: Top panels: left shows the synthetic transit light-curve for an Earth-sized body in orbit with period ~ 3.6 days. Right shows a magnified view of the region of the first transit event. Lower panels show the same light-curve by plotting fluxes versus integer numbers. This eliminates time gaps and may help to identify individual, periodically dropping points, transits, that were not detected by the BLS algorithm.

balling might help in the case of long period systems which can remain undetected because of the period cut-off (at long orbital period) used by my implementation of the BLS algorithm. I used a cut in the number of photometric points in-transit (>5) and on the number of individual observed eclipses over the time of observation (>5). Therefore, eye-balling can identify targets for which further analyses might be warranted (for example, when more data become available in the archive).

4.3 Results

To date I find no evidence for transiting sub-stellar or planetary companions for the stars in my sample. The data quality and more importantly, the relative small size of the white dwarf sample, do not allow me to definitively conclude on planetary survival to post main-sequence stellar evolution. The detection sensitivity of each individual star in the sample depends on numerous factors such as the stars magnitude, the light-curve photometric accuracy, the time sampling and the presence of long gaps in the observations. Different observing seasons and fields may be more or less affected by the presence of correlated noise (red noise), and different SuperWASP cameras might be affected by residuals due to different sources of distortion (e.g. vignetting, flat fielding, background subtraction). Some SuperWASP fields may be more crowded than others. Moreover, my simulations only cover SuperWASP magnitudes of $V \sim 12, 13, 15$. The sample of stars analysed here covers magnitudes ranging from $V \sim 9$ to $V \sim 15$. Thus, the detection limits for the 194 white dwarf targets might be slightly different from the limits obtained from my simulations. Thus to obtain detection limits related to the sample of white dwarfs I have combine the results obtained from simulations with the results of the analysis of the 194 white dwarfs. This allowed an estimate of my detection sensitivity for each individual star in the sample.

As discussed above, the response of the BLS algorithm depends on many different factors. For example, for a given orbital period and transit duration the BLS ability to recover the transit crucially depends on the coverage of the transit event in the light-curve. Thus it is not possible to make definitive statements about individual

objects. However, it is possible using my results on various system configurations to make statements about the population as a whole, or probabilistic statements about individual objects. When the BLS algorithm is used to analyse the 194 light-curves, the majority of the WDs are detected with periods within 0.02d (~ 30 minutes) from one day period and its harmonics, suggesting that a large number of stars just show periodical variations due to the SuperWASP observational window function. The analysis of SuperWASP light-curves is in general affected by the presence of these periodic features which show real power in the BLS power spectrum due to the day and night alternation in the observations (see chapter 5 for more details on this point). In fact the detection of any extra-solar planet with orbital period within 1.5% from 24h, and interger multiple or sub-multiples of 24h, would be extremely difficult to detect for SuperWASP.

It is worth mentioning that some well known variable objects are present in my sample, for example V471 Tau (Kamiński et al., 2007) and MS Peg (Schmidt et al., 2005). Both systems consist of a WD in a close binary system with a low-mass stellar companion of late spectral type (K and M respectively). Both systems are detected by my own implementation of the BLS algorithm and have power spectra peaked at the correct orbital period of 12.5h and 4.16h, respectively. The signal detection efficiency SDE values for the detection are of $SDE = 13.66$ and $SDE = 11.77$ respectively, in either case, significantly above the detection threshold (of $6.3SDE$). This confirms my ability to detect the presence of periodic signals in the light-curves of the stars in my sample.

4.4 Limits to companions' frequency

In order to estimate an upper limit to the frequency of sub-stellar and terrestrial companions to white dwarfs, I used the detection limits derived from my simulations and the results obtained from the analysis of the sample of 194 stars.

I first used a binomial distribution to describe the probability ($P_{\text{ROB}}(n; N, f)$) of finding n transiting companions for a given sample of N stars, with a true companion frequency f (eg. see McCarthy & Zuckerman 2004; and Appendix of Burgasser et al. 2003) as follow:

$$P_{\text{ROB}}(n; N, f) = \frac{N!}{n!(N-n)!} f^n (1-f)^{N-n} \quad (4.4)$$

The binomial distribution describes exactly n successes with probability f^n , and $N-n$ failures with probability $(1-f)^{N-n}$. When the two quantities N and n are known equation 4.4 can be used to derive the distribution (P_{ROB}^1) describing the probability of f , where f is the frequency of transiting companions. The probability $\text{Prob}^1(f; n, N)$ is proportional to $P_{\text{ROB}}(n; N, f)$ for f in the interval $[0, 1]$. I obtain P_{ROB}^1 by normalising :

$$\int_0^1 P_{\text{ROB}}^1(f; n, N) df = 1 \quad (4.5)$$

which yields $P_{\text{ROB}}^1 = (N+1) P_{\text{ROB}}$. The evaluation of the integral of equation 4.5 implies the use of the Beta and Gamma functions. Because my results have been obtained for simulations of transiting companions I can use the transit probability P_{tr} (Figure 3.3, chapter 3) to evaluate the number of stars in the sample which may

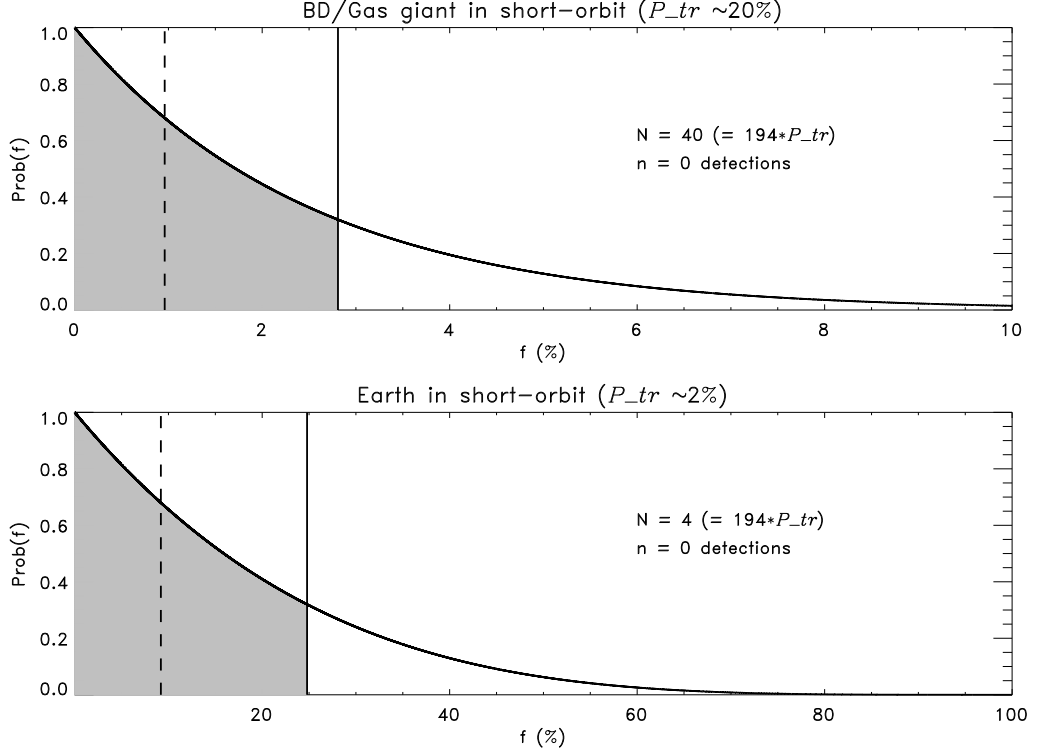


Figure 4.4: Probability distribution (PD) for the frequency f of companions to white dwarfs. I report the range in f that delimits the 68% of the integrated probability function. Top panel shows the PD for a sub-stellar companion in orbit with period ~ 2 h, for which the transit probability is $P_{tr} \sim 20\%$ (sample size $N = 40$ and $n = 0$ detected companions). Lower panel shows the PD for a terrestrial companion in orbit with ~ 5 h period and $P_{tr} \sim 2\%$ ($N = 4$ and $n = 0$). Solid line and y axis (shaded region) delineate a region that contains the 68% of probability. Dashed line and y axis delineate a region that contains 32% of probability.

have transits visible from Earth. Thus, the number of stars N (originally 194) in the sample is reduced accordingly to the transit probability as follow:

$$N = 194 \times P_{tr}(R_{pl}, P_{orb}) , \quad (4.6)$$

where the transit probability depends on the planetary radius R_{pl} and on the orbital period P_{orb} . In this way, the bias due to the choice of the detection method can be eliminated and the evaluation of the frequency upper limits assume a generic

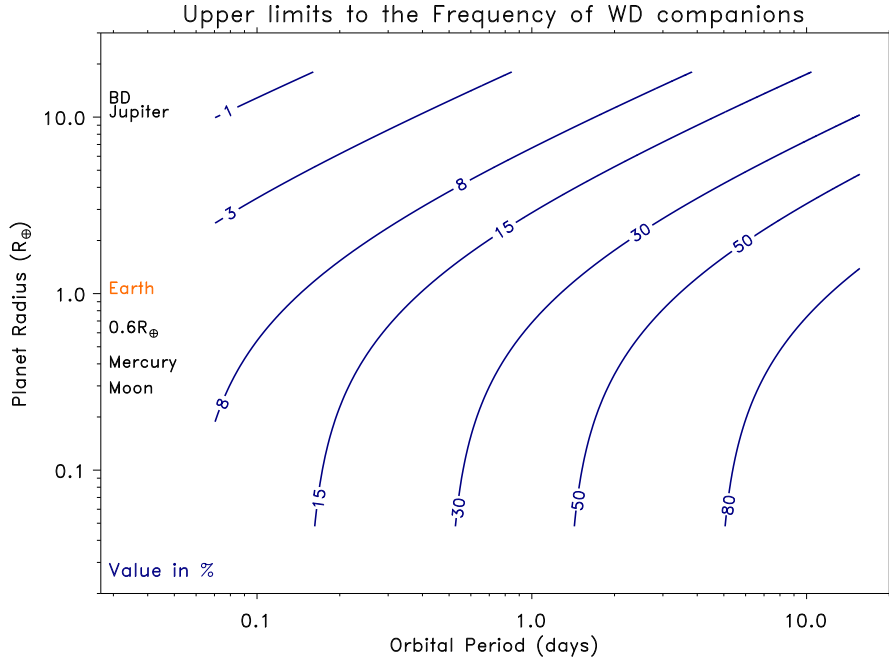


Figure 4.5: Contours of constant values for the estimated upper-limits to the frequency of sub-stellar and terrestrial companions to white dwarfs (values in percent). Estimated under the assumption of 100% detectability. The upper limits are derived for f that delimits the 68% of the integrated probability function.

significance. Since the binomial probability distribution is not symmetric about its maximum value, I report the range in f that delimits the 68% of the integrated probability function. Figure 4.4 shows the probability distribution for f as determined for a brown dwarf or a gas giant planet orbiting a white dwarf with a period of ~ 2 hours for which the transit probability is $P_{tr} \simeq 20\%$, top panel. In the lower panel, I show the same for an Earth-sized companion with orbital period of ~ 5 hours ($P_{tr} \simeq 2\%$).

I consider all possible companions sizes spanning the size of the Moon to Jupiter-sized objects with orbital periods between ~ 2 hours and 15 days. Figure 4.5 shows the upper limits for the frequency of companions to white dwarfs (blue solid lines are contours of constant values in %) obtained using equation 4.4 and equation 4.6.

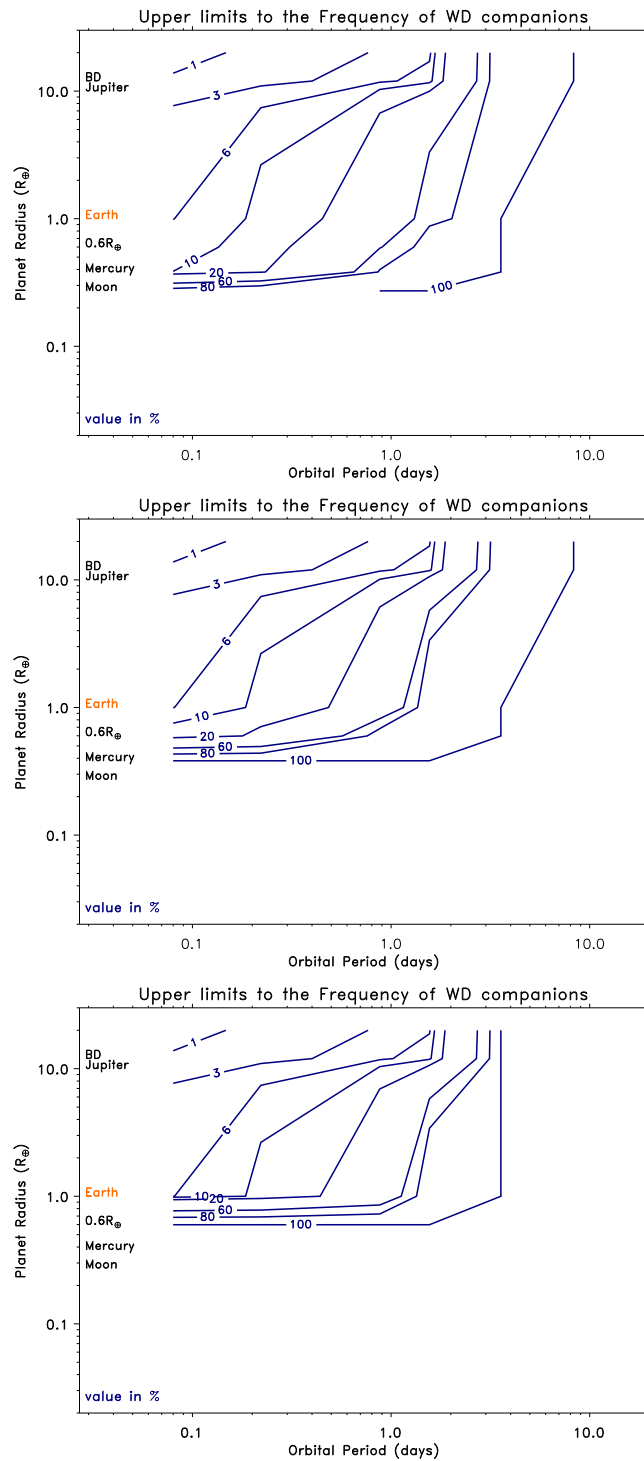


Figure 4.6: Same as Figure 4.5 but when I consider my detection sensitivity as derived from simulations for a white dwarf of $V \sim 12$ top-panel, for a white dwarf of $V \sim 13$ and $V \sim 15$ middle and lower panel respectively.

In this particular case I have assumed the transit signals to be detectable for every planetary body and at every orbital distance from the star (100% detectability). This ideal situation is shown to emphasise the changes in the frequency upper limits when the results from my simulations are taken in to account. To consider my results I introduced the detection probability P_{det} in equation 4.6 as follow:

$$N = 194 \times (P_{tr} \times P_{det}) . \quad (4.7)$$

The detection probability is obtained from my simulations as described in chapter 3, see also Table 3.3. In equation 4.7 the transit probability P_{tr} and the detection probability P_{det} are independent. The probability of detecting a transiting system is given by the probability of the system transiting \times my probability of detecting the transit signature. Indeed, the set of synthetic transit light-curves used in my simulations all contain simulated transit signals injected at different orbital periods and for different companion sizes. Thus the detection probability represents the rate of detection (over many hundreds of simulations) of a simulated transit recovered with my BLS implementation.

I show in Figure 4.6 the estimated upper limits to the frequency of companions to white dwarfs when results from my simulation are considered. Figure 4.6 top panel shows my results for a white dwarf of magnitude $V \sim 12$. The middle and lower panel show my results for a white dwarf of $V \sim 13$ and $V \sim 15$ respectively.

The sample of white dwarfs investigated in this study has magnitude spanning from $V \sim 9$ to $V \sim 15$, see for example the target list in Table 4.1. Because the time needed to perform exhaustive simulations covering the entire magnitude range for

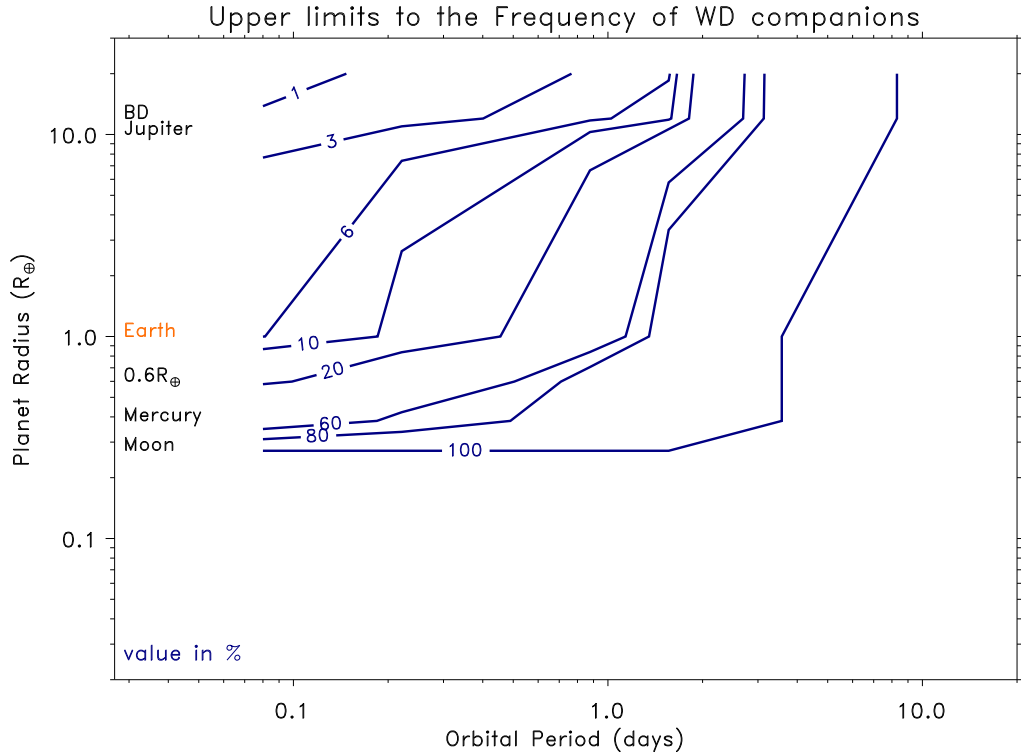


Figure 4.7: as for Figure 4.6 but with the detection probability P_{det} estimated over the range of magnitudes of the 194 stars in my sample.

all the stars in my sample is prohibitive, my results only cover three magnitude ranges ($V \sim 12, 13, 15$). Thus to obtain detection limits covering the magnitudes spanned by the white dwarfs in my sample I have used the detection probabilities derived from my simulations and I have extrapolated and interpolated over the entire magnitude range (9–15 in V). I subsequently calculated a weighted mean to account for the probabilities P_{det} so obtained. Thus, the values of P_{det} finally contains the information relevant to my sample.

Finally, I used the values for P_{det} to calculate the upper limit to companions frequency this time based on the estimated values of the detection probability for the whole white dwarf sample. Figure 4.7 shows my results.

4.5 Conclusion

Encouraged by the results obtained from my simulations I have searched for transit and eclipse signals in a sample of 194 white dwarfs for which I have SuperWASP data. I have used my implementation of the box-fitting BLS routine details of which are given in chapter 3. To date, I do not find any evidence of sub-stellar or smaller planetary rocky bodies transiting the 194 stars. I have used this null result to derive an upper limit to the frequency of companions to white dwarfs given my sample size and my detection sensitivity as estimated from simulations.

Although my attempt to find planetary companions to white dwarfs proved fruitless, I emphasise the importance of searching for sub-stellar and planetary companions to white dwarfs. Theoretical studies on post main-sequence stellar evolution and in particular studies focusing on the crucial phase of common envelope suggest that planetary survival is not beyond possibility (see e.g. Villaver & Livio 2007). The results obtained from my research are far from conclusive as very large samples are needed in order to test sub-stellar and planetary survival to the later stages of stellar evolution. We know that about 2% of isolated white dwarfs have infra-red excesses due to the presence of dust discs (Farihi et al., 2009). Because of the very low transit probability of rocky planetary companions to white dwarfs (less than a few percent, see Figure 3.3, chapter 3), a much larger sample of white dwarfs is needed (5 to 10 times larger) in order to test planetary survival to the later stages of stellar evolution.

Table 4.1: Results for 194 white dwarfs in the SuperWASP archive. From left to right I list the SuperWASP ID, the corresponding McCook & Sion ID, the SuperWASP V_{mag} and the number of observations.

1SWASP	WD	V_{mag} (WASP)	N
J000007.24+295700.6	2357+296	12.24	15825
J000331.62−164358.4	0000−170	14.87	10446
J000732.24+331727.7	0004+330	13.95	21067
J000818.17+512316.7	0005+511	13.42	4876
J002130.72−262611.0	0018−267	13.92	7305
J003112.96−271253.7	0028−274	14.99	6961
J003145.95+571817.1	0029+571	10.50	2511
J003353.90−270823.6	0031−274	14.30	7293
J003952.15+313229.3	0037+312	15.03	9429
J004121.46+555009.1	0038+555	13.47	6202
J005317.46−325956.6	0050−332	13.45	9316
J005340.53+360118.4	0050+357	14.54	14264
J011011.78+270104.8	0107+267	15.61	4702
J011018.59−340025.5	0107−342	14.27	10151
J011211.65−261327.7	0109−264	13.14	10038
J011547.45−240651.0	0113−243	15.03	29846
J012942.57+422817.1	0126+422	13.51	18136

Continued on next page

Table 4.1 – continued from previous page

1SWASP	WD	V_{mag} (WASP)	N
J013856.85+152742.5	0136+152	14.37	2251
J014754.80+233943.8	0145+234	14.19	4653
J015202.95+470005.5	0148+467	12.08	4362
J020253.98–165303.5	0200–171	11.41	8756
J021255.35+170356.5	0210+168	14.32	3082
J021616.34+395125.5	0213+396	14.11	7608
J021733.49+570647.3	0214+568	13.29	2279
J022440.83+400823.0	0221+399	10.02	13621
J023530.74+571524.8	0231+570	13.68	2223
J023619.55+524412.4	0232+525	13.76	6096
J024502.37–171220.5	0242–174	15.54	7672
J031149.19+190055.7	0308+188	14.46	2711
J031315.18+190824.5	0310+188	16.20	2547
J031445.95+481206.1	0311+480	14.33	4908
J031942.73+344223.8	0316+345	14.37	7868
J034329.01–454904.2	0341–459	15.19	15506
J035024.96+171447.4	0347+171	9.47	2515
J035630.59–364119.7	0354–368	12.66	9400
J035705.82+283751.5	0353+284	11.67	5606
J040434.12+250851.8	0401+250	13.58	3841
J041010.32+180223.8	0407+179	14.50	2303

Continued on next page

Table 4.1 – continued from previous page

1SWASP	WD	V_{mag} (WASP)	N
J044321.26+464205.7	0441+467	12.76	4283
J045013.52+174206.1	0447+176	12.09	3155
J045535.93–292900.0	0453–295	15.58	9872
J045713.22–280752.8	0455–282	13.90	9869
J045722.55+415556.6	0453+418	11.98	5475
J050003.17–362346.4	0458–364	13.33	13986
J050355.38–285436.0	0501–289	13.58	8629
J050530.60+524951.9	0501+527	11.72	3288
J051233.54+165209.6	0509+168	13.47	2931
J051302.56+162246.8	0510+163	14.15	2930
J052906.46+271257.6	0526+271	15.17	9014
J053244.82+261200.7	0529+261	14.14	7321
J053620.20+412955.7	0532+414	13.46	5935
J054748.47+280311.6	0544+280	13.04	5246
J055814.64–373426.1	0556–375	14.64	10756
J061000.36+281428.4	0606+282	13.00	3538
J061518.70+174341.9	0612+177	13.37	2676
J061934.22+553642.9	0615+556	13.40	3258
J062312.60–374127.9	0621–376	12.09	11875
J062702.01–252249.7	0625–253	12.98	9502
J064112.82+474419.8	0637+477	14.52	2673

Continued on next page

Table 4.1 – continued from previous page

1SWASP	WD	V_{mag} (WASP)	N
J064856.08–252347.0	0646–253	13.74	9658
J071736.26+582420.4	0713+584	12.03	2993
J073427.45+484115.6	0730+487	14.96	5327
J082705.14+284402.6	0824+288	14.27	9142
J084253.04+230025.6	0839+231	14.45	3552
J084644.40+353833.7	0843+358	14.72	7568
J084909.48+342947.8	0846+346	15.47	6769
J085730.45+401613.2	0854+404	15.16	11310
J090148.65+360708.1	0858+363	14.87	9274
J092921.28–041005.9	0926–039	14.57	1030
J094159.32+065717.1	0939+071	15.11	1621
J094250.60+260100.1	0939+262	14.88	4173
J094846.64+242126.0	0945+245	14.47	4244
J101628.64–052032.8	1013–050	13.21	1362
J101801.63+072123.9	1015+076	15.59	1179
J102405.90+262103.7	1021+266	9.33	7073
J102459.84+044610.5	1022+050	14.16	3186
J102712.01+322329.8	1024+326	13.51	9985
J102909.80+020553.7	1026+023	14.05	2885
J103936.73+430609.2	1036+433	11.17	4800
J104616.19–034033.4	1043–034	14.14	1913

Continued on next page

Table 4.1 – continued from previous page

1SWASP	WD	V_{mag} (WASP)	N
J105220.53–160804.3	1049–158	14.59	7601
J105443.32+270657.2	1052+273	13.73	4875
J105709.94+301336.8	1054+305	14.69	5270
J110432.58+361049.1	1101+364	14.87	5109
J111912.41+022033.1	1116+026	14.82	2222
J111934.60–023903.1	1117–023	14.61	3512
J112542.87+422358.3	1122+426	13.25	6053
J112619.09+183917.2	1123+189	14.20	4600
J112910.93+380850.1	1126+384	15.22	9645
J112918.04+181645.8	1126+185	14.10	2932
J113227.35+151731.0	1129+155	14.26	2853
J113423.42+314605.9	1131+320	14.94	10834
J113705.10+294758.1	1134+300	12.64	9241
J114359.35+072906.1	1141+077	14.47	2810
J114803.16+183046.6	1145+187	14.38	7930
J115006.09–231613.8	1148–230	14.56	14440
J115119.30+125359.8	1148+131	14.15	3680
J115154.20+052839.7	1149+057	15.37	5172
J120145.98–034540.6	1159–034	15.04	2630
J120526.70–233312.3	1202–232	12.90	14521
J120936.01–033307.6	1207–032	13.69	2636

Continued on next page

Table 4.1 – continued from previous page

1SWASP	WD	V_{mag} (WASP)	N
J121229.13–062206.8	1209–060	13.39	2608
J121233.90+134625.0	1210+140	14.78	3027
J121356.28+325631.6	1211+332	14.93	11489
J121410.52–171420.2	1211–169	10.15	19365
J122747.36–081438.0	1225–079	16.06	1347
J123515.36+233419.4	1232+238	13.63	8160
J124428.57–011858.1	1241–010	13.51	3307
J125217.16+154444.2	1249+160	15.00	10250
J125223.56+175651.6	1249+182	15.43	10340
J125514.83+373229.3	1253+378	15.58	8160
J125702.33+220152.9	1254+223	13.67	18254
J131341.59–305133.5	1310–305	14.92	14136
J131621.95+290556.3	1314+293	12.77	8381
J132115.12+462324.0	1319+466	14.97	8291
J133601.94+482846.7	1333+487	13.89	8310
J133741.51+363903.8	1335+369	14.51	9836
J133913.55+120831.0	1336+123	14.89	3770
J134117.94+342153.6	1339+346	14.93	8492
J134307.26–310151.4	1340–307	13.25	11366
J135153.93+140945.6	1349+144	14.77	3288
J141026.96+320836.1	1408+323	14.22	7984

Continued on next page

Table 4.1 – continued from previous page

1SWASP	WD	V_{mag} (WASP)	N
J141329.93+213730.0	1411+218	13.86	5943
J142439.16+091714.2	1422+095	14.90	2935
J143545.65–163818.1	1432–164	14.58	13190
J144814.07+282511.6	1446+286	14.71	16402
J145156.24+422142.9	1450+425	15.57	8167
J151127.61+320417.9	1509+322	13.10	3865
J151714.27+031028.0	1514+033	13.79	4115
J152950.39+085546.3	1527+090	14.72	3552
J154419.46+180643.9	1542+182	15.08	4373
J155501.99+351328.6	1553+353	14.74	12136
J155804.76–090807.3	1555–089	13.37	3793
J160521.18+430436.6	1603+432	15.32	1353
J160532.09+122542.8	1603+125	15.91	3148
J161053.25+114353.6	1608+118	14.61	3466
J161419.14–083326.4	1611–084	13.43	3792
J161623.83+265310.7	1614+270	14.82	14663
J161928.99–390711.5	1616–390	14.63	11944
J162333.83–391346.1	1620–391	11.09	12748
J163339.30+393053.6	1631+396	13.88	31052
J164539.13+141746.3	1643+143	15.69	3436
J164718.40+322833.0	1645+325	13.90	27543

Continued on next page

Table 4.1 – continued from previous page

1SWASP	WD	V_{mag} (WASP)	N
J170033.62+441024.3	1659+442	13.27	43025
J170530.69+480311.4	1704+481	13.93	20729
J172643.19+583732.0	1725+586	13.44	10838
J175255.81+094751.9	1750+098	9.53	1425
J175332.27+103724.3	1751+106	14.15	4268
J181140.81+282939.5	1809+284	14.06	5172
J182029.78+580441.2	1819+580	14.23	3511
J182337.00+410402.2	1822+410	14.63	18410
J191858.65+384321.8	1917+386	11.58	1700
J194740.52−420026.3	1944−421	10.30	23397
J195219.66−384613.8	1948−389	13.34	32011
J200039.25+014341.9	1958+015	12.48	2948
J202706.23+553415.0	2025+554	12.98	6313
J202956.18+391332.3	2028+390	12.45	2902
J203202.39+183139.6	2029+183	12.20	12648
J203454.59−273449.2	2031−277	15.28	6762
J203838.16−332635.0	2035−336	14.25	12714
J204808.16+395137.8	2046+396	14.94	2942
J204906.71+372813.2	2047+372	12.74	2989
J210031.30+505118.0	2058+506	15.93	3907
J211244.06+500618.1	2111+498	12.93	3354

Continued on next page

Table 4.1 – continued from previous page

1SWASP	WD	V_{mag} (WASP)	N
J211652.86+241214.9	2114+239	12.39	4421
J211708.29+341227.6	2115+339	12.33	2117
J211717.80+504407.3	2115+505	11.55	3392
J211856.30+541241.4	2117+539	11.99	6914
J212146.78–331048.0	2118–333	14.27	7625
J212454.89+155903.8	2122+157	13.80	12929
J212458.14+282603.5	2122+282	14.60	2969
J212743.10–221148.4	2124–224	14.94	11028
J213636.12+220433.5	2134+218	14.53	13813
J213652.94+124719.5	2134+125	13.35	11732
J213846.20+230917.6	2136+229	12.28	14626
J214954.57+281659.8	2147+280	15.04	16920
J215202.73+372617.9	2149+372	12.59	9941
J215453.40–302918.4	2151–307	15.05	7776
J215618.25+410245.5	2154+408	14.61	3191
J220714.40+072232.3	2204+071	14.91	7675
J221029.22–300543.7	2207–303	13.61	11058
J222919.42–444138.4	2226–449	14.48	10279
J223822.75+313418.4	2236+313	14.75	11464
J225848.13+251544.0	2256+249	12.63	13430
J230740.13–342753.4	2304–347	14.86	10752

Continued on next page

Table 4.1 – continued from previous page

1SWASP	WD	V_{mag} (WASP)	N
J231219.65+260419.7	2309+258	14.57	9279
J232606.58+160019.4	2323+157	13.63	4815
J232715.83+400124.7	2324+397	15.41	21231
J233135.65+410130.6	2329+407	14.18	17476
J233149.93–285252.6	2329–291	14.29	10859
J233536.58–161743.8	2333–165	13.57	5660
J234350.87+323247.2	2341+322	13.28	11404
J235530.18–251612.7	2352–255	13.61	10780
J235644.76–301631.6	2354–305	15.01	10635

Chapter 5

Monitoring variable white dwarfs with SuperWASP

Abstract

In previous chapters I mainly focused on the identification of photometric variability due to transits and eclipses of sub-stellar and planetary companions to white dwarfs. Here I present a more complete search for extrinsic and intrinsic variable white dwarfs in my sample. I have employed the modified Lomb-Scargle periodogram, the CLEAN algorithm and the Phase Dispersion Minimisation (PDM) techniques to search for photometric variability in my sample of 194 white dwarfs with $V > 15$. Each individual light-curve was analysed and periods were considered successfully detected when they could be recovered by more than one period-searching method. I have tested my detection ability against well known variable sources such as the close binary (WD+dM) MS Peg. When a period was detected I fitted a Gaussian

function to it in order to obtain an error estimate on the period. I discard WDs with periods within 1.5% of 1 day and its harmonics. I discuss a few of the interesting variable sources in my sample and refine my previous error estimate of their period by means of the Schwarzenberg-Czerny post-mortem method. When available, I also report the period listed in the SuperWASP Table ‘*Period-ajns3*’ of variable objects found in the SuperWASP database.

5.1 Introduction

The majority of white dwarfs are considered photometrically stable and are often used as flux calibration standards for optical and ultra-violet observations (Holberg 2007; and Holberg & Bergeron 2006). However, a few white dwarfs are intrinsically variable. For example ZZ Ceti stars are non-radial pulsators with variability time scales of a few hundred seconds. The detection of multi-periodic luminosity variations and the identifications of the pulsation’s modes can reveal the properties of the stellar interiors, e.g. the core composition (Fontaine & Brassard, 2008). ZZ Ceti stars are DA(H-atmospheres) white dwarfs showing pulsations in a very narrow temperature interval ($10,000 \leq T_{\text{eff}} \leq 12,000\text{K}$) around the hydrogen recombination temperature ($T_{\text{eff}} \simeq 12,000\text{K}$). By direct analogy with ZZ Ceti stars, DB(He-atmosphere) white dwarfs show non-radial pulsations albeit at higher temperatures ($T_{\text{eff}} \simeq 25,000\text{K}$, the He recombination temperature, see e.g. Winget et al. 1981; for a review see Winget & Kepler 2008). A third class of pulsators is represented by the pre-white dwarf PG 1159 stars (DOVs), around $75,000 \leq T_{\text{eff}} \leq 170,000\text{K}$. These objects have carbon and oxygen in their atmosphere and pulsations are driven by their cyclic ionisation (Fontaine & Brassard 2008 and references therein). If this

behaviour is true in general it means that every white dwarf will become a non-radial pulsator as it cools during its lifetime. Therefore, it is important to certify the purity of the, so called, instability strips.

About 2% of the total white dwarf population consists of isolated magnetic white dwarfs (Brinkworth et al., 2005). These rare stars often display star-spots which rotate in and out view, causing photometric variability the amplitude of which is dependent on the spot's size. Magnetic white dwarfs are extremely important as they can reveal the rotation period of the star, hard to measure in non-magnetic white dwarfs due to heavy gravitational broadening of their spectral lines (Brinkworth et al., 2005). A few very highly magnetic white dwarfs also display photometric variability as they rotate due to changes in the magnetic field connected to changes in the opacity in the outermost layers of the stellar atmosphere, as in the case of RE J0317-853 (Barstow et al. 1995 magnetic dichroism, see Ferrario et al. 1997). The detection and characterisation of variability connected to the star's magnetic field may help us to understand the physical origin of the phenomenon. Maybe connected to the progenitor star's magnetic field (e.g. Ferrario & Wickramasinghe 2007).

White dwarfs in close binaries often display optical variability such as eclipses, or the effects of reflection and irradiation on a low-mass companion. The detection of the orbital period of these binary systems is extremely important to constrain post-main sequence stellar evolution and in particular the most important process of Common Envelope interaction (Paczynski 1976; and Willems & Kolb 2004). In addition, detailed studies of systems orbital periods, masses and ages, can help us to better understand the physics of cataclysmic variable stars and Type Ia supernovae, possibly shedding light on physical phenomena such as angular momentum loss via

gravitational wave versus magnetic breaking radiation (King 1988; Parthasarathy et al. 2007). Moreover, a detailed analysis of the light-curve of any such system can help reveal the effects of tidal and rotational distortions as well as the irradiation and reflection due to mutual heating and radiative interaction of the binary components. The temperature changes and the reprocessed emitted light have the effect of raising the detected flux from the facing hemisphere of the secondary. The effects of irradiation and in particular the detection of reflected light from low-mass companions is also important for the study of the secondary atmosphere (e.g. Peraiah 1983).

I have searched for periodicities in my sample of 194 WDs for which I have SuperWASP data. I have analysed each target using multiple period-searching techniques: the Lomb-Scargle modified periodogram and the CLEAN algorithm are designed to detect weak periods in unevenly spaced datasets showing sinusoidal variability. The Phase Dispersion Minimisation (PDM) technique can be very efficient in identifying non-sinusoidal variability. The structure of this chapter is as follow: in § 5.1 I briefly describe my period-searching approach, in § 5.2 I tested my method using the known variable system MS Peg (Schmidt et al. 1995). In § 5.3 I report my results for the variability search of the 194 white dwarfs in my sample, and I discuss a few of the more interesting variable targets in the sample. My conclusions presented in § 5.4.

5.2 Data Analysis

For the analysis of the white dwarf sample I have used the set of light-curves described in chapter 4. The set of light-curves were previously de-trended by means of

the Tamuz algorithm (see §2.5, Tamuz et al. 2005). Although light-curve de-trending is necessary to remove linear systematics from the data (thus increasing the detection probability for transit searches), I also found that some intrinsic variability had also been removed during this step. This effect has been also observed in some of the light-curves of SuperWASP planets, which show larger transit amplitudes in the raw data (more about this later).

The period search I performed utilises multiple period-finding techniques. A Lomb (1976)-Scargle (1982) modified periodogram (L-S hereafter) was used to investigate the presence of any sinusoidal variation in each star's light-curve. This method is equivalent to a least-square fit of sinusoids to the data and allows the recovery of weak periodic signals in unevenly sampled data, as is found for SuperWASP data. Because the Lomb-Scargle algorithm requires $10^2 N^2$ operations to analyse N data points, I used the fast version of the algorithm described by Press et al. (1992) which requires less computations (order of $10^2 N \text{Log} N$). I used an implementation of the algorithm written in the programming language IDL (Interactive Data Language) available at (<http://idlastro.gsfc.nasa.gov>) which I customised to my needs. The routine uses a fixed number of trial frequencies (N_{freq}) evaluated using the Horne & Baliunas empirical formula (Horne & Baliunas 1986). That is :

$$N_{freq} = -6.362 + 1.193N_0 + 0.00098N_0^2 \quad (5.1)$$

where N_0 is the number of observations in a light-curve. The frequency grid is chosen such that:

$$F_{max} = 0.016666 \text{sec}^{-1} (= 1 \text{mins}) \quad \text{and} \quad F_{min} = \frac{1}{4 \times \Delta T} \quad (5.2)$$

where ΔT is the length of the dataset. The frequency step is chosen to be:

$$\delta F = \frac{(F_{max} - F_{min})}{N_{freq} - 1} \quad (5.3)$$

However, these parameters F_{max} ; F_{min} , N_{freq} and δF can be easily modified in the IDL routine. In my case and more generally for any SuperWASP light-curve, I have to deal with uneven sampled data with observational gaps. Therefore the Nyquist frequency and the Shannon sampling theorem lose their meaning. SuperWASP telescopes take 30 second exposures every ~ 8 -10 minutes. Thus, the Fourier transform of the data could eventually carry information about frequencies higher than the minimum spacing in the data (Roberts et al. 1987). I decided to set the maximum sampling frequency to 0.0166 sec^{-1} , which corresponds to a minimum period of one minute. The amplitudes of the periodograms are normalised according to the formulation of Horne & Baliunas (1986) by scaling to the total variance of the data. For each periodogram I estimated the power detection threshold corresponding to a false alarm probability (FAP) of 0.01, according to the number of independent frequencies N_{freq} used (see Scargle 1982). I have investigated the significance of the highest peak in the Lomb-Scargle periodogram performing simulations over a set of five hundred simulated white noise light-curves, free from astrophysical periodic signals, modelled using real SuperWASP light-curves. Figure 5.1 shows the probability distribution function (PDFs) for the set of 500 simulations performed. In Figure 5.1 the black-line represents the PDF of the data and the red-solid line is the best fit model. The dashed line correspond to a FAP of 0.01. I calculated the significance Sg of the highest peak in the L-S power spectrum as follows:

$$Sg = \frac{\mathcal{P}_{max} - \langle \mathcal{P} \rangle}{\sigma_{\mathcal{P}}} \quad (5.4)$$

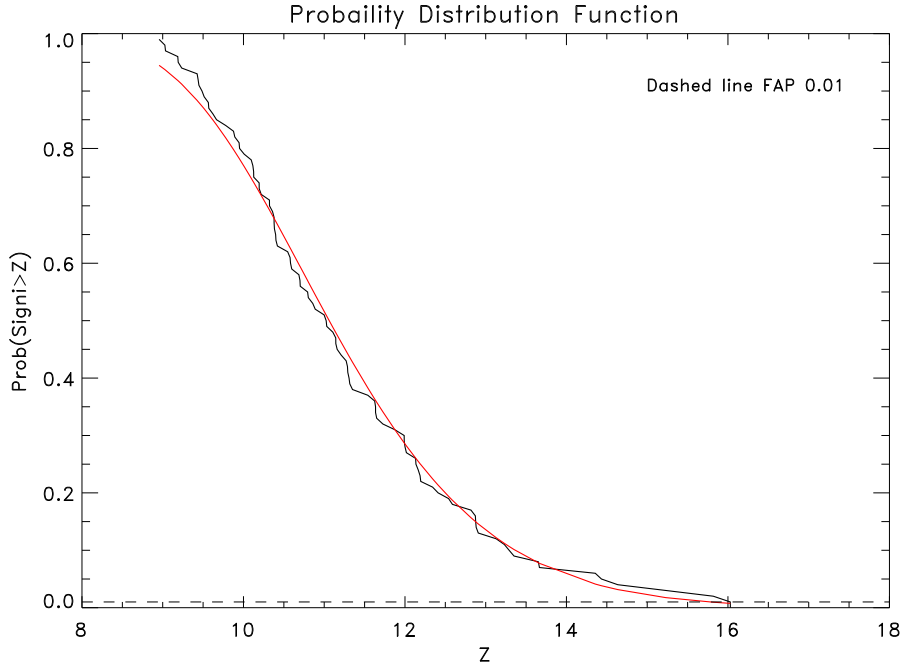


Figure 5.1: Probability Distribution Function derived for 500 simulated light-curve modelled using SuperWASP data and for Gaussian random noise. Black-line is the PDF as obtained from the data, the red-line is the best fit model. Dashed line correspond to FAP of 0.01.

where \mathcal{P} is the intensity of the power spectrum, \mathcal{P}_{max} is the intensity at the highest peak in the periodogram, $\langle \mathcal{P} \rangle$ is the average intensity and $\sigma_{\mathcal{P}}$ is the standard deviation over the frequency band tested. I found that periods with power $> 16Sg$ should be caused by real periodic signals. A $FAP = 0.01$ corresponds to a detection significance of 99%. This method implies Gaussian random noise in the data and the statistical significance of the highest peak in the periodogram can be lower for datasets dominated by covariant noise structure (red noise). SuperWASP data show real power at one day ([d]) and at periods of $n[d]$ and $n/k[d]$, with n and k small integers. The strength of signals arising from the SuperWASP window function can differ from light-curve to light-curve, and also from season to season. Thus I expect that sources can be differently affected by variation occurring at periods arising from

the window function (e.g. in the case of gaps occurring at one day or at its sub-harmonics) resulting in false detections. In such cases, visual inspection of the target folded light-curve is sufficient to reject the period. When a period was detected by the L-S routine a Gaussian function was fitted to the peak in order to obtain an estimate of the period confidence interval. I used the width of the Gaussian best fit function (e.g. Figure 5.5), which corresponds to a 1σ confidence interval. Other approaches may also be used. For example, the period confidence interval could be estimated using half-size of the frequency bin ($1/2$ the frequency step, $\frac{\delta F}{2}$), centred on the highest peak in the periodogram, then converting this to units of period (for example the Starlink routine PERIOD98). However, because the calculation of the period confidence interval can be statistically incorrect (see Schwarzenberg-Czerny 1991), the width of the best-fit Gaussian function represents a more conservative estimate. For the interesting variable objects found in my sample, I subsequently refined the period error using the post-mortem analysis described in Schwarzenberg-Czerny (1991). This technique evaluates the mean noise power level (MNPL) in the vicinity of the highest peak in a periodogram, avoiding features arising from the window function. The period confidence interval is then equal to the width of the line at the peak minus the MNPL level. Figure 5.2 shows the principle of the Schwarzenberg-Czerny (1991) post-mortem test. This procedure can be performed graphically (see Schwarzenberg-Czerny 1991).

The sub-sample of white dwarfs for which I found a period with the L-S periodogram, were subsequently analysed by means of the CLEAN algorithm. The majority of the targets in my sample are fainter than $V \sim 12$, the magnitude limit at which Super-WASP can achieve good photometric precisions. Thus, because the periodogram of noisy data is noisy, the use of a second detection technique will allow me to confirm

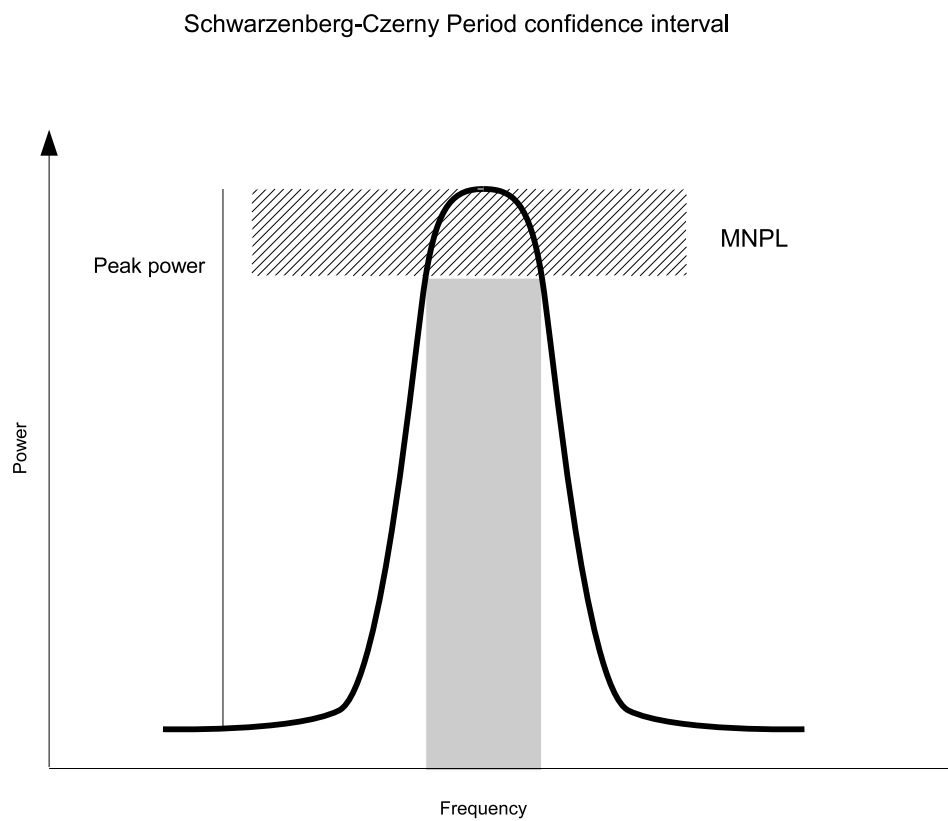


Figure 5.2: Illustration of the post-mortem analysis described by Schwarzenberg-Czerny (1991). The period confidence interval is shown in light grey. The mean power of the noise is shown by the hatched region.

or disprove any identified period. The CLEAN algorithm (Roberts et al. 1987; Foster 1995) is designed to remove spurious features from a periodogram, by performing a deconvolution of the Fourier spectrum of the data with the window function, possibly revealing the presence of additional signals. The Fourier convolution theorem states that the Fourier Transform (FT) of the product of two functions in the time domain is equivalent to a convolution of the FTs in the frequency domain. In practice the algorithm identifies the highest peak in the Fourier spectrum and creates an impulse response, spike-like, function of power equal to a reduced fraction of the maximum. The amount subtracted is governed by the *gain*, an adjustable quantity. It then convolves this component with the window function and subtracts it from the spectrum to obtain a *residual* spectrum. The above procedure is repeated until a stop condition is met: in this instance when the residual spectrum is below a desired noise value or the requested number of iterations has been reached. In Figure 5.3 I compare the Lomb-Scargle periodogram and the CLEAN periodogram for the known variable binary system MS Peg (more later) for which I can detect the system orbital period (more in § 5.1). Figure 5.3 highlights the ability of the CLEAN algorithm to remove the majority of the spurious features present in the Lomb-Scargle periodogram thus confirming and also improving the signal detection.

Finally, I have performed a visual inspection of each folded light-curve to identify periods due to residual systematic effects such as gaps due to the day-night alternation and/or to residuals affecting groups of targets in a field (for example residual Moon-light variation). The folded light-curves that on visual inspection appeared to show non-sinusoidal variations were also analysed by means of the Phase Dispersion Minimisation (PDM) technique (Stellingwerf, 1978). The PDM can be a powerful

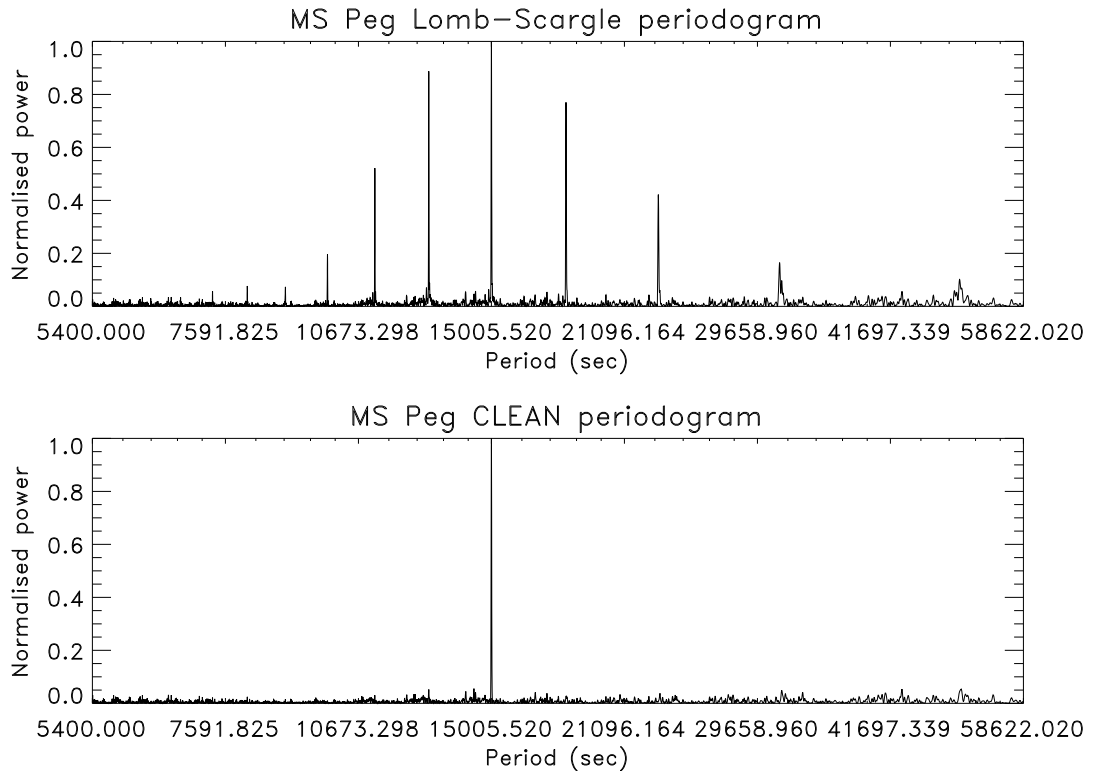


Figure 5.3: Comparison between the L-S and the CLEANed periodogram for the test target MS Peg. My approach considered a period successfully detected if was identified in both periodograms and with 0.003d tolerance.

tool for detecting non-sinusoidal photometric variability. The PDM technique performs a least-squares fit where the model function is the “average” curve obtained by averaging the points of each of the light-curve bins. As such the PDM includes all harmonics in the fitted function, reducing the effect of power leakage encountered in Fourier methods due to the use of a finite frequency interval.

I considered a period successfully detected if it was recovered using two of the methods described above within an interval of 0.003d from each other. The use of the CLEAN algorithm and the PDM technique also allowed me to test the light-

curve for the presence of multi-periodic signals in the data (see Roberts et al. 1987; Stellingwerf 1978).

Among the stars in my sample there are some notable known variable objects such as MS Peg (Schmidt et al., 1995) and V471 Tau (Kamiński et al., 2007). Here I used the well known binary system MS Peg, a white dwarf primary and a main-sequence red dwarf secondary, to test my approach and to verify my ability to detect and characterise photometric variability using SuperWASP data.

5.3 MS Peg

The binary system MS Peg (1SWASPJ225848.13+251544.0, WD2256+249) is a close-detached binary system which consists of a white dwarf primary and a low-mass main sequence red dwarf secondary of spectral type M3-5 (Schmidt et al., 1995). The system shows variability due to the reflection effect caused by the white dwarf heating the surface of the co-rotating secondary star.

The sinusoidal variability shown by the MS Peg light-curve reveals the system's orbital period (4.1679 ± 0.0003 h Schmidt et al. 1995) and characterise it as a pre-cataclysmic variable. SuperWASP routinely observed WD2256+249 between 2004 and 2006 with a total of 13337 epochs. I used the L-S algorithm to search for a periodic signal in the SuperWASP light-curve of MS Peg. Figure 5.4 top panel shows the L-S periodogram. The power spectrum peaks at a frequency of $6.6642110^{-5} \text{ sec}^{-1}$ which corresponds to the system orbital period $P_{orb} = 4.1682$ h (see also Figure 5.3). I obtained an estimate of the error by fitting a Gaussian function to the peak and

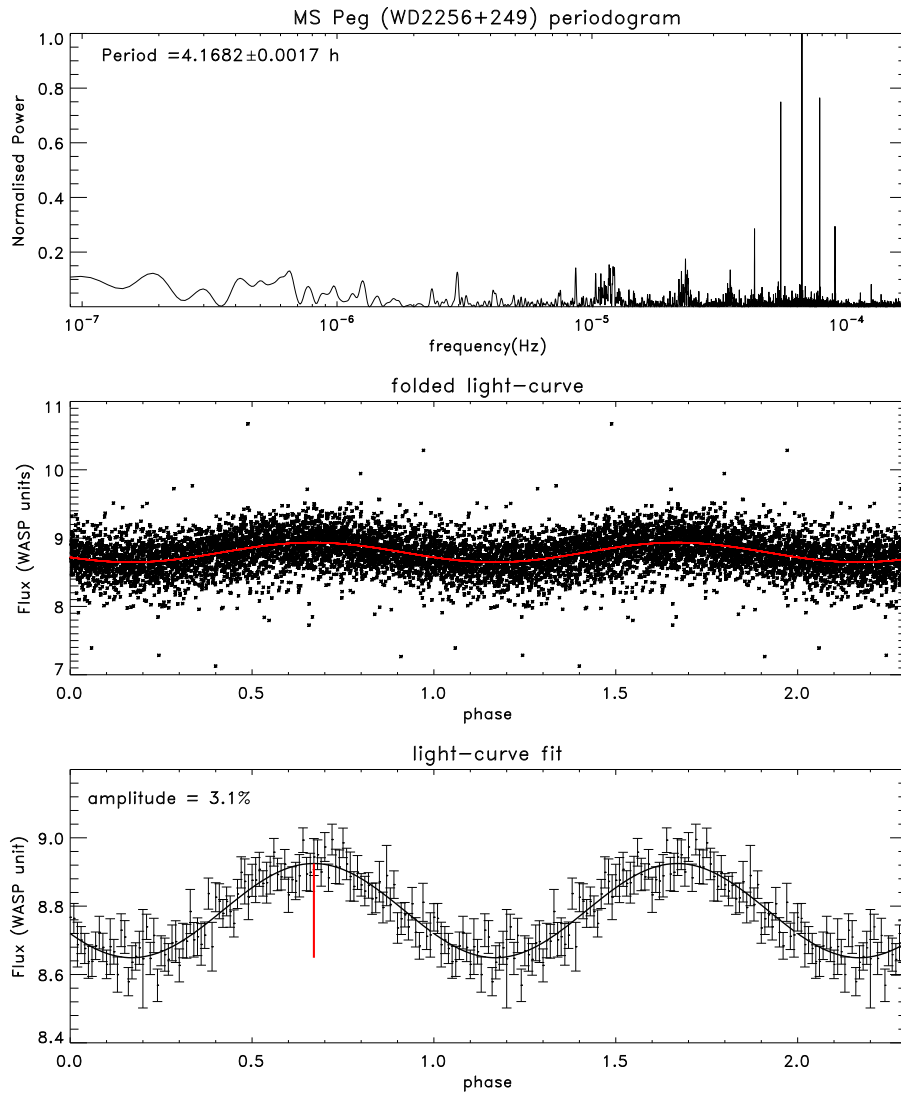


Figure 5.4: Top panel shows the CLEANed periodogram as in Figure 5.3. Middle and lower panel show the folded light-curve and the bin folded light-curve for the detected period (4.1682 ± 0.0007 h). The red curve is the best fit model sine function as by equation 5.5. The fit yields a peak-to-peak amplitude of variation of 3.1%.

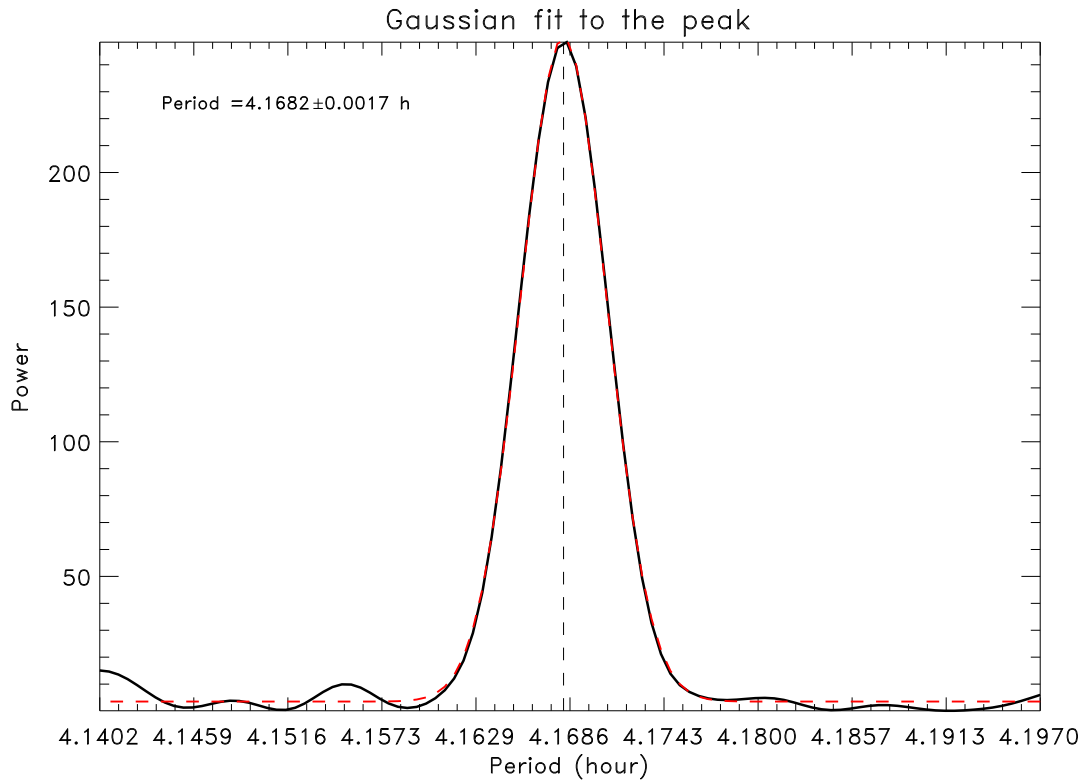


Figure 5.5: Gaussian fit to the highest peak in the periodogram. The error on the period is the width of the best fit Gaussian function.

using the width of the best fit function. This yielded an error of $\Delta P = 0.0017\text{h}$. Figure 5.5 shows the best Gaussian fit to the highest peak.

Once the period was correctly identified I refined the period-search by using a small frequency interval centred around the peak and I performed a new search using a finer frequency step. The period confidence interval was calculated by means of the Schwarzenberg-Czerny (1991) post-mortem analysis and I obtained $P = 4.1682 \pm 0.0007\text{h}$ which is consistent with the published period $P = 4.1679 \pm 0.0003\text{h}$, previously found by Schmidt et al. (1995). The light-curve of the binary MS Peg folded on the above period reveals sinusoidal variability which is due to the pres-

ence of the low-mass secondary showing a reflection effect. The estimate for the amplitude of the sinusoidal variation was obtained by fitting a sine-wave model of the form:

$$Y_{fit} = A_0 + A_1 [\sin(2\pi ft - \phi)] \quad (5.5)$$

where A_0 gives the y-zero-point, A_1 is the amplitude and ϕ is the phase given by the time-zero-point. I found the system to vary with a peak-to-peak amplitude of $\sim 3\%$. Figure 5.4, central and lower panels show the folded light-curve and the binned folded light-curve. In red I show the fitted model. The amplitude of the variable signal is somewhat smaller than the variability observed by Schmidt et al. (1995). Schmidt et al. (1995) found Δmag variation of 5% in the B band and $\sim 10\%$ in V band. The reason for this discrepancy may reside in SuperWASP broad band filter, which covers both B and V filters (more sensitive in the B band). In addition, the data taken during the 2004 pilot season were obtained in white light with the telescope transmission response completely determined by the Earth atmosphere and SuperWASP optics. This may have caused the removal of some variability by the pipeline when correcting for secondary extinction, back-ground subtraction and flat fielding. In addition, SuperWASP photometry is performed using three different apertures, 1.5, 2.5, and 3.5 pixels which corresponds to ~ 20 , ~ 34 and ~ 48 arc-seconds.

Thus it is possible that other objects are found within the $48''$ radius centred on the target star. These objects may be the cause of starlight contamination which dilutes the photometric variation of the target source. In the case of MS Peg (Figure 5.6) I found two fainter objects within $48''$ radius. Information extracted from

the archive indicates that the two objects are 4.58 and 1.97 magnitudes (WASP magnitudes) fainter than MS Peg. This implies a dilution factor of 9%. Figure 5.6 shows the distances of the two fainter sources. An additional subtractive factor may also be related to the employment of the light-curve de-trending algorithm (Tamuz et al., 2005) used to remove linearly correlated noise contributions from the data. Light-curve de-trending can remove some of the intrinsic source variability, and in particular long term variability. A reduction in the amplitude of the transit signals of SuperWASP planets has indeed been observed. Figure 5.7 shows the raw SuperWASP light-curve of MS Peg folded on the period identified in this study. The amplitude variation of $\sim 3.63\%$, of the raw data, is found to be larger than the amplitude of 3.1% for de-trended data (Figure 5.4). The above effects, acting alone or in combination may explain the somewhat smaller variation in the signal amplitude found by this study.

5.3.1 Variability results

The results obtained from this study are presented in Table 5.1. My search method identified periods for a large number of white dwarfs in the sample. However, the majority of sources were detected at the 1-day and n/k [d] harmonics (where n and k are small integer). I only list objects for which variability was confirmed by visual inspection of the folded light-curve. In Table 5.1 from left to right I list the SuperWASP ID, the white dwarf ID (McCook & Sion 2003), other names from SIMBAD, the period (P) detected from this study, the period confidence interval (δP), and the amplitude (A) of the photometric variation obtained by fitting a model sine-wave to the light-curve. Finally, I also list the closest period found in

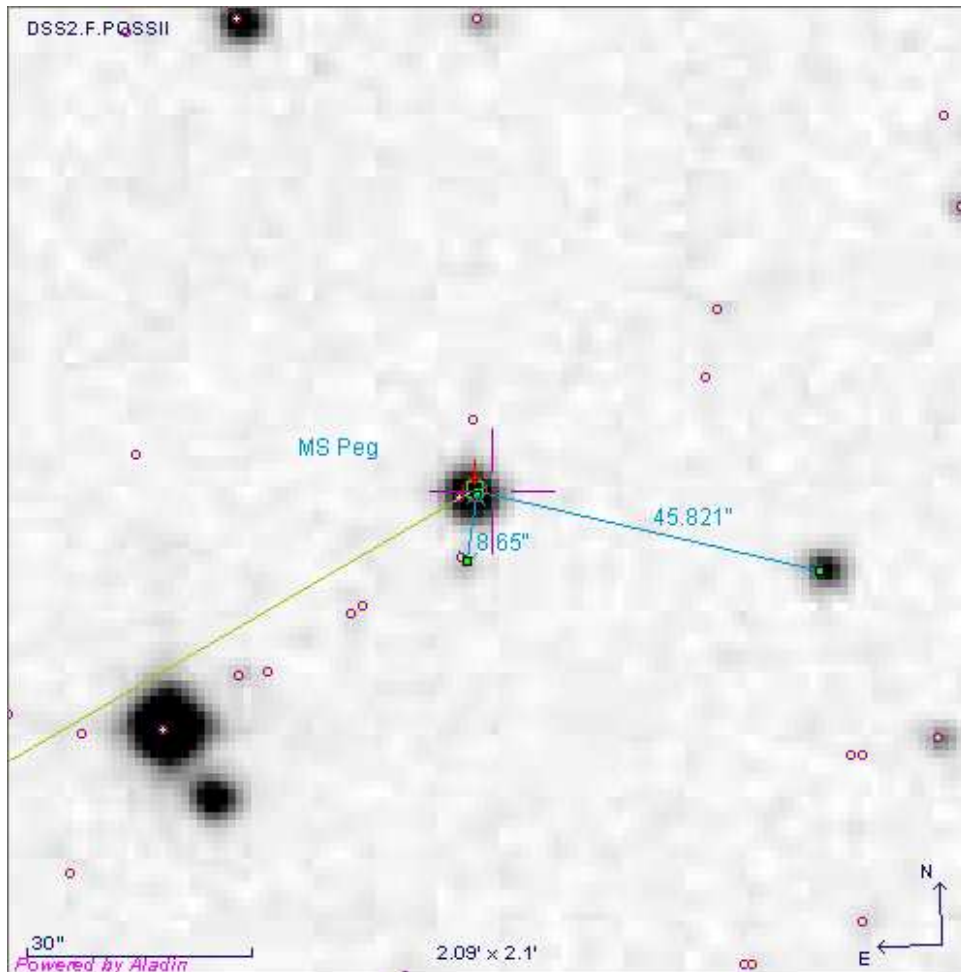


Figure 5.6: Image obtained from Aladin. The image show the presence of two fainter stars within 2.5 pixel radius from MS Peg.

the SuperWASP archive Table ‘Period-ajjn3’ where available. I note that all white dwarfs but HZ 43 are also listed in the SuperWASP Table ‘Period-ajjn3’ of periodic sources found in the SuperWASP archive (see e.g Norton et al. 2007 for more details). The reason why HZ 43 is not found in the list of variable sources in table Period-ajjn3 is due to the use of a more strict FAP threshold for detection. This was necessary in order to minimise the number of sources detected with variability connected to the day and the day sub-harmonics. I also note that GD 358 was first detected by my method to vary with a period of ~ 24 h. Only after a more detailed analysis of the

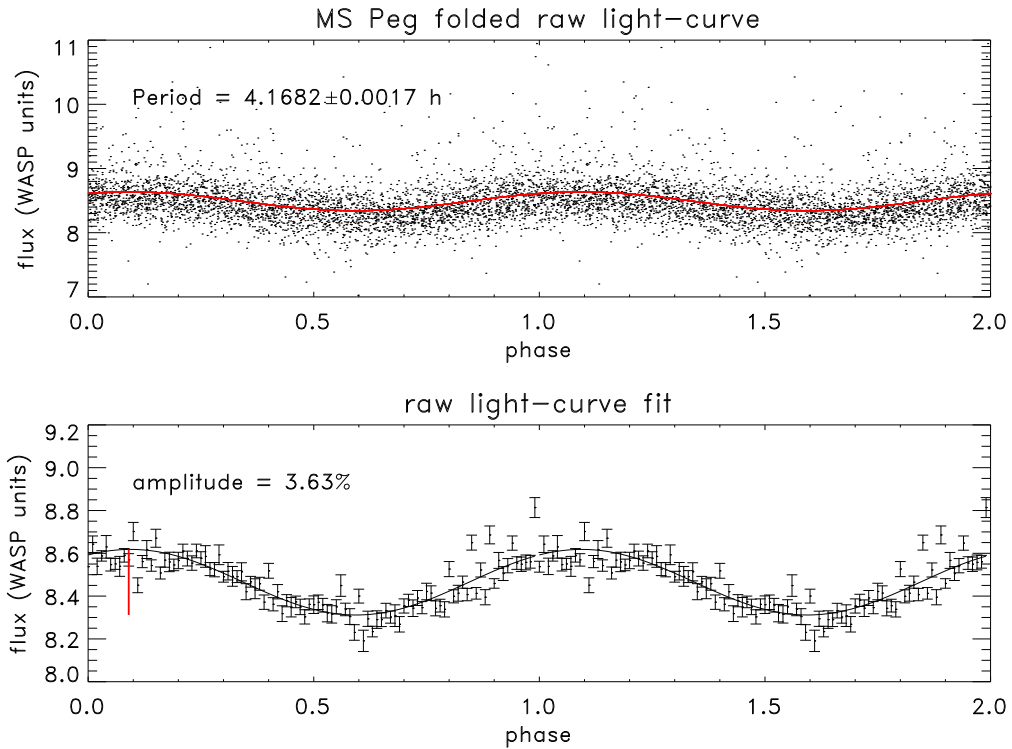


Figure 5.7: As in Figure 5.4. The fitted sine function yields a peak-to-peak variation of 3.63% somewhat bigger than in the case of de-trended data.

light-curve I could identify a large number of periodicities as discussed in § 5.3.5. Figures 5.16 and 5.17 show the CLEANed periodograms and the folded light-curves for the white dwarfs listed in Table 5.1 which are not individually discussed in the text. I also indicate the detected period and the amplitude of the observed photometric variation.

In the following I will discuss in more detail a few of the more interesting objects for which a clear period or more than one period could be detected. These consist of the binary systems WD0353+284, WD1024+326 and HZ 43, and the non-radial DB pulsator GD 358.

5.3.2 WD0353+284

The system WD0353+284 (1SWASP J035705.82+283751.5, 2RE J0357+283 Jeffries et al. 1996) consists of a hot WD and a rapidly rotating cool-star of spectral type K2V, in a wide binary. Jeffries et al. (1996) detected photometric variability due to the high magnetic activity of the rapidly rotating secondary ($P_{rot} = 0.3646 \pm 0.0002d$, $= 8.7504 \pm 0.0048h$). The system was observed by SuperWASP during 2004 and 2006 observing seasons with a total of 5606 good photometric points. I used my period-searching method and found a period of $P_{rot} = 8.755 \pm 0.008h$ which is consistent with the rotational period of the K dwarf detected by Jeffries et al. (1996). A separate analysis of the 2004 and 2006 seasons revealed the presence of a second periodicity in the 2004 data highlighted in Figure 5.8. Figures 5.8 and 5.9 show the CLEANed periodogram for the 2004 and 2006 light-curves respectively. The highest peak in Figure 5.8 corresponds to the known rotational period of $8.755 \pm 0.008h$, the second highest peak in the periodogram is found at the period $P = 5.3525 \pm 0.0038h$, while the third peak is an alias of the rotational period $P_{8.75h}$ with the P_{12h} of the window function. In order to investigate the origin of the second period in the 2004 data I pre-whitened the data by subtracting a sine-wave at the rotational period $P_{8.75h}$ and subsequently performed a Discrete Fourier Transform (DFT) of the residuals. Figure 5.10 shows the periodogram of the residuals where the highest peak is found at $P = 5.3525 \pm 0.0038h$.

The remnant peaks in the periodogram are aliases due to the window function, and can be obtained by the following calculation:

$$\frac{1}{P_{alias}} = \frac{1}{5.35h} - \frac{1}{24h} = \frac{1}{6.88h}, \quad (5.6)$$

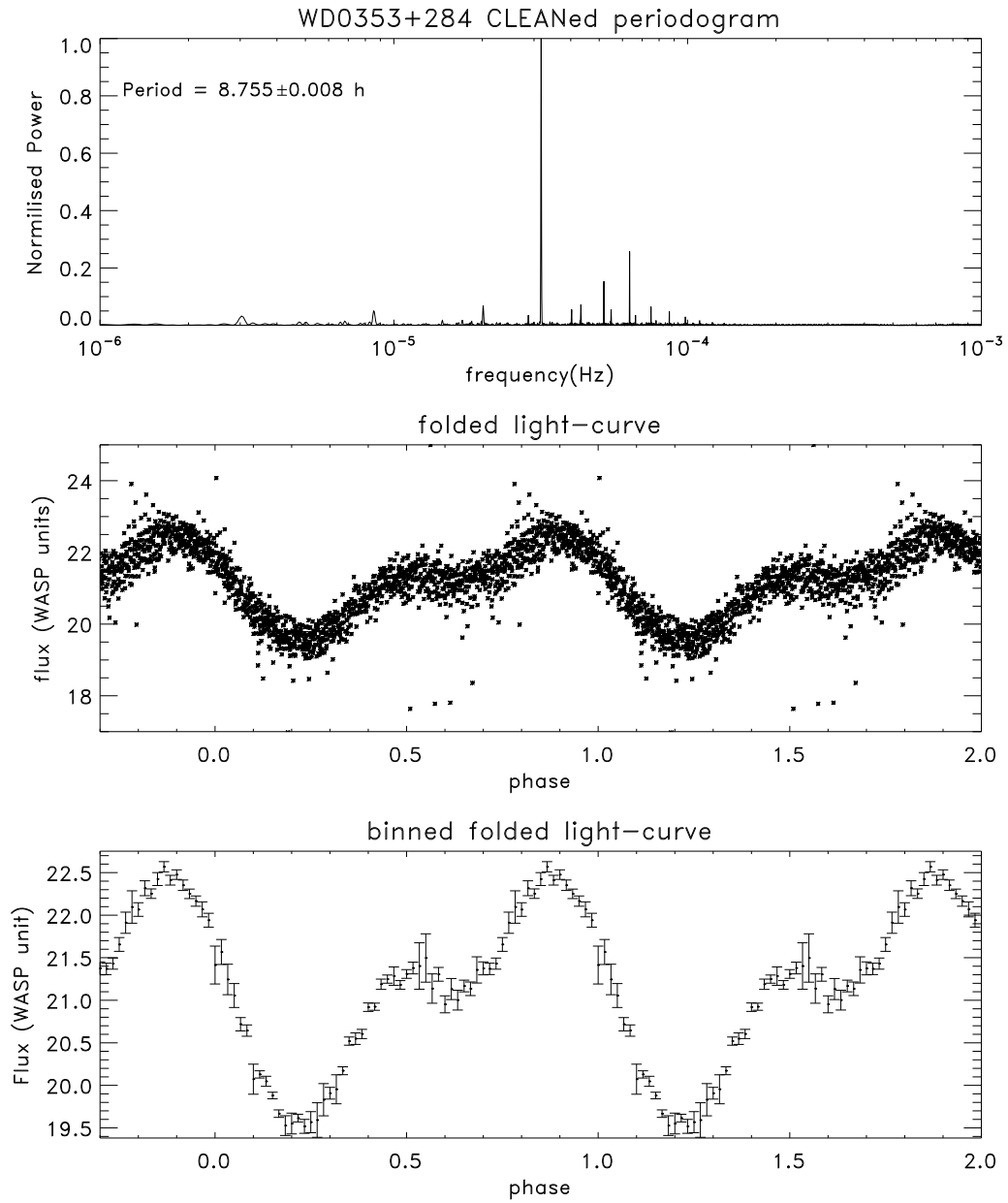


Figure 5.8: As for Figure 5.4 I show the CLEANed periodogram, and the light-curve folded on the on the rotational period of the K star (8.75h). The peculiar shape of the phase time series might be due to the presence of a second spot on the star surface rotating faster with period of 5.35h.

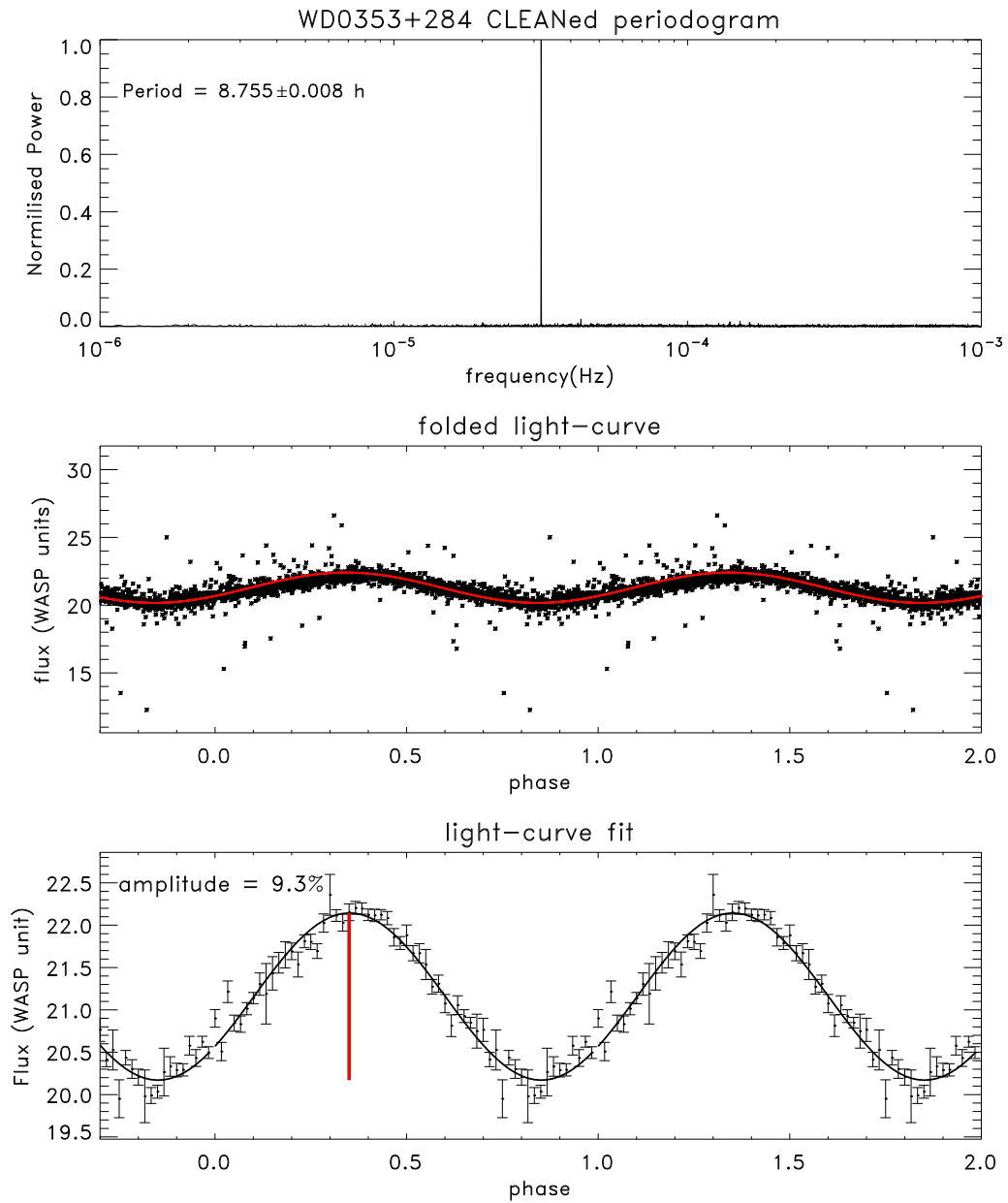


Figure 5.9: same as Figure 5.8. The separate analysis of the 2006 data do not show the presence of any periodicity other than the known rotational period of the K dwarf secondary.

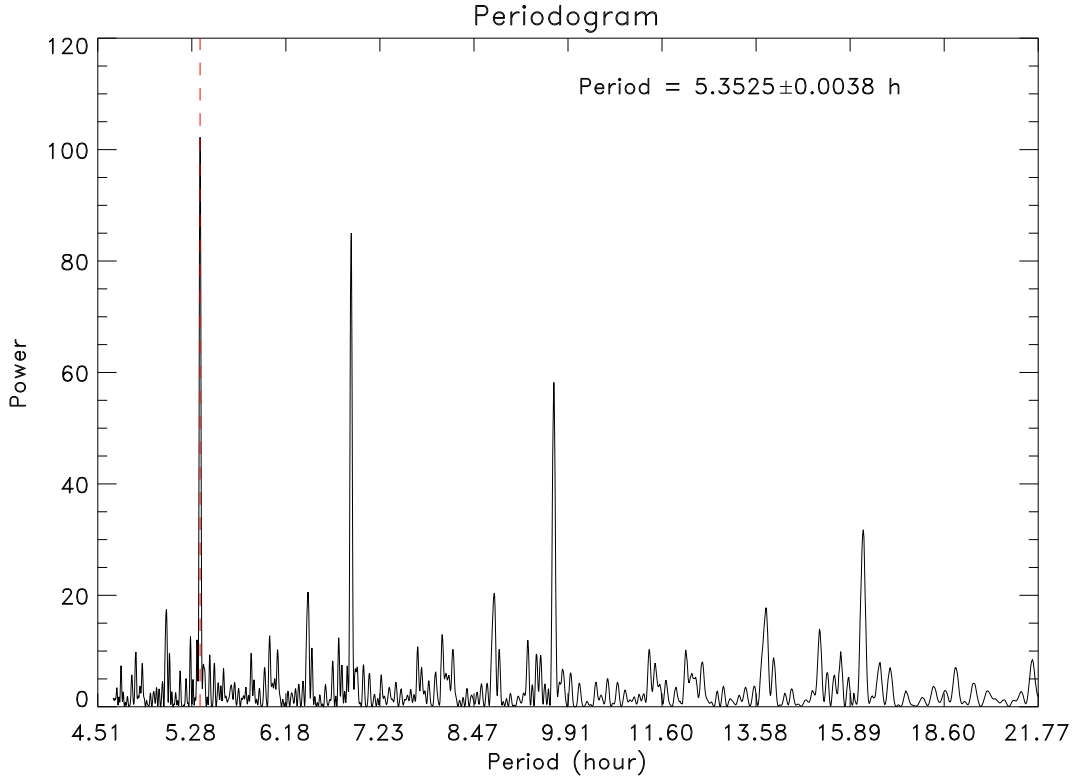


Figure 5.10: I show here the DFT of the residuals after subtracting a sine function at 8.775 hour. The highest peak in the DFT periodogram is found at the period $P = 5.353h$, suggesting the veracity of my detection.

$$\frac{1}{P_{alias}} = \frac{1}{5.35h} - \frac{1}{12h} = \frac{1}{9.66h}, \quad (5.7)$$

respectively the second and third peak in the DFT periodogram. The separate analysis of the 2006 data do not show the presence of the $P_{5.35h}$. I suggest that a possible explanation for the additional period at 5.35h in the 2004 data might be related to the magnetic activity of the secondary (fast rotating star) possibly showing large star spots and differential rotation. I note the large ΔP and the high rotational rates implied may be more plausible in close binary systems such as pre-cataclysmic variable systems (e.g. V471 Tau, $P_{rot} = 12.5h$, Kamiński et al. 2007). However, the absence of this second period in the 2006 data may be consistent with

the sporadic onset of star spots. Jeffries et al. (1996) suggest that because of the wide nature of the binary system the secondary stars could be spun up by wind accretion during the AGB phase in a detached configuration (named “wirring” star, Wind-accretion Induced Rapid Rotator). Further investigations are needed in order to exhaustively investigate the nature of the second period detected in the light-curve of WD0353+284. Future developments and analysis will be available in a forthcoming paper (Faedi et al. 2009, in prep.).

5.3.3 WD1024+326

The white dwarf WD1024+326 (1SWASPJ102712.01+322329.8, REJ1027+322) has been studied by Genova et al. (1995). They suggest the system to consist of a wide binary (angular separation less than 10 arcsec) consisting of a hot ($T_{eff} = 40,000\text{K}$) white dwarf and a main-sequence star of spectral type G2V. I have analysed the light-curve of WD1024+326 which was observed by SuperWASP in 2004 and 2006 seasons with a total of 1331 days equivalent to 9949 epochs. The analysis of the light-curve revealed the target to vary with a detected period of $P = 31.97\text{h}$ equivalent to $1.331 \pm 0.012\text{d}$. I subsequently refined the period confidence interval using the post-mortem analysis of Schwarzenberg-Czerny (1991) and found the period $P = 1.331 \pm 0.004\text{d}$. Figure 5.11 shows the CLEANed periodogram from 2004 data, in addition the period is also detected in the 2006 data and during this season in different SuperWASP cameras. Figure 5.11 middle panel shows the folded light-curve on the detected period. The lower panel shows the light-curve fit which identifies the system to have a peak-to-peak amplitude variation of $\sim 4.4\%$. A consultation of SIMBAD database and of the available literature for this target

could not find any previously recorded photometric variation. I suggest that as in the case of WD0353+284 discussed above, I can detect the rotational period of the non-degenerate component of the binary system. Despite the large separation between the two binary components, the use of wide-angle optics ($13.7''/\text{pixel}$ for SuperWASP), means that the system falls on an individual pixel (id est the system is unresolved). The detection of the period at 1.33 day could be consistent (similar order of magnitude) with the observed for WD0353+284 suggesting that WD1024+326 could be a “wirring” star too. However, further analysis of the target using data from 2007, 2008 and 2009 SuperWASP seasons will enable us to confirm the periodicity found here.

5.3.4 HZ 43

An other system similar to the two already discussed is WD1314+293 also known as HZ 43 (1SWASPJ131621.95+290556.3). The hot white dwarf ($T_{eff} = 49,000$ K) is known to be in a wide binary system (angular separation 3 arcsec; Luyten 1970) with a stellar companion of spectral type M3-5 (see Napiwotzki et al. 1993 and Margon et al. 1976). HZ 43 is a well studied white dwarf also known for its exceptional ultraviolet luminosity and was the first object to be detected as an EUV source (Margon et al. 1976). McAlister et al. (1996) studied the system and determined the magnitude of the two components to be $V_{WD} = 12.94 \pm 0.02$ and $V_B = 14.32 \pm 0.08$, SuperWASP magnitude is $V_{WASP} = 12.78 \pm 0.03$. In fact McAlister et al. (1996) found the secondary to contaminate the photometry of the WD by making it to appear 0.27 ± 0.02 magnitude brighter in V , which also explains the somewhat brighter SuperWASP magnitude (also in agreement with Margon

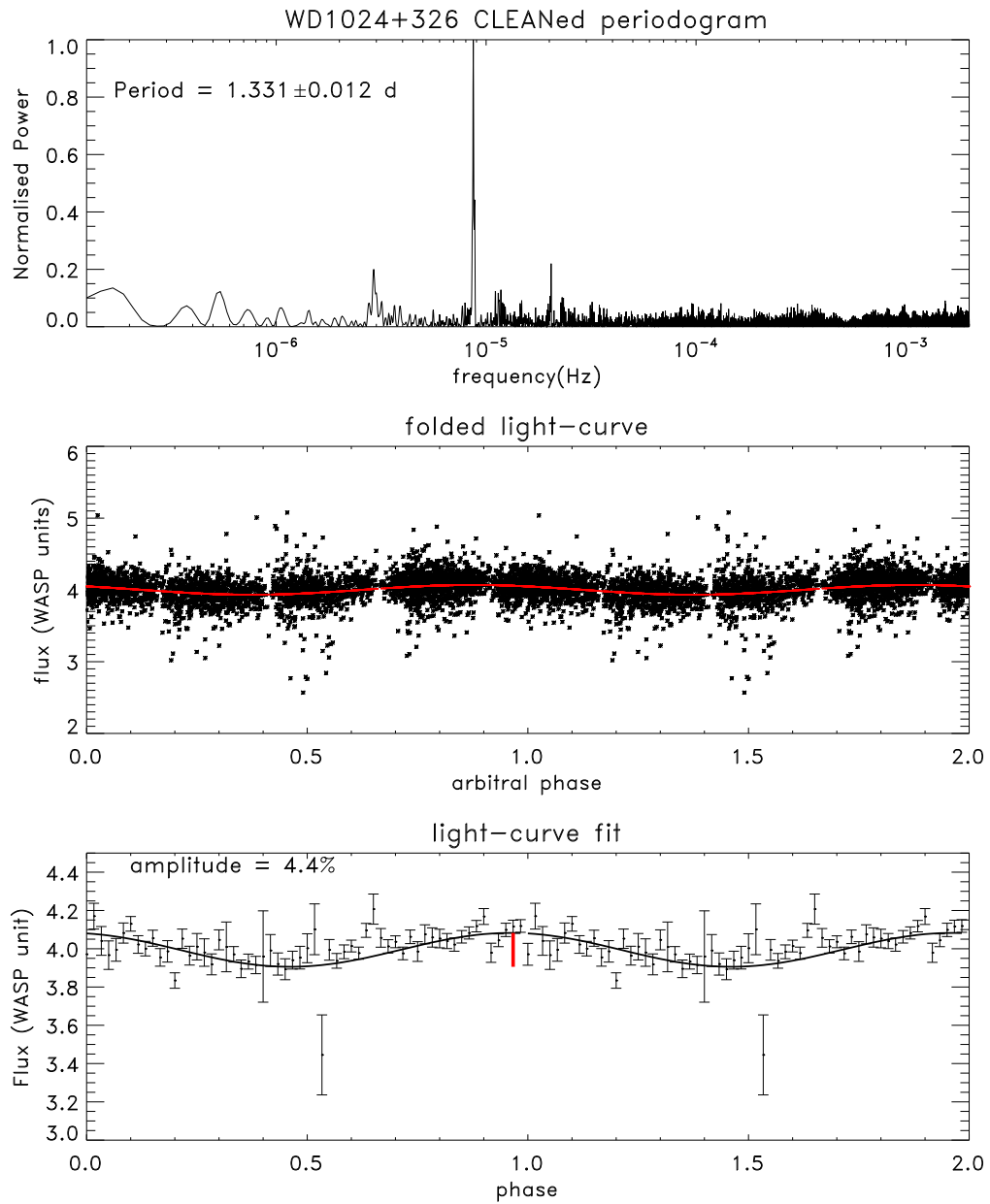


Figure 5.11: As for Figure 5.4 we show the CLEANed periodogram, top panel. Middle and lower panel show the folded light-curve and the model fit sine function. I obtain a peak-to-peak modulation of 4.4%.

et al. 1976). The object is unresolved in SuperWASP thus the observed magnitude is the sum of the magnitudes of the individual components. My analysis of the system found a modulation in the folded light-curve with a peak-to-peak variability amplitude of 1.47% at a period of $P = 3.626 \pm 0.066$ d. SuperWASP observed HZ 43 in 2004 and 2006 seasons (8381 epochs) and the period was detected in both seasons. Because HZ 43 is a very well known and well studied star and never previously seen to be variable, I think that the observed variation is most probably due to the rotational period of the active M dwarf companion, and that my detection is again connected to the large pixel size used by SuperWASP. Figure 5.12 shows the CLEANed periodogram for my detection of $P = 3.626$ d. From the Gaussian fit to the highest peak I obtained a first estimate of the period error, Figure 5.13 show the best fit to the period $P = 3.626 \pm 0.066$ d. I subsequently refined the error estimate as described by Schwarzenberg-Czerny (1991) and obtained $P = 3.626 \pm 0.036$ d. The analysis of the residuals after pre-whitening (subtracting a sine function) with the above period do not show any residual power in the periodogram.

Figure 5.12 middle and lower panels show the folded light-curve for HZ 43 and the fit to a model sine-wave with the period $P = 3.626 \pm 0.036$ d. The fit yields a signal amplitude variation of 1.47%. The white dwarf HZ 43 is a widely used calibration standard for satellite instruments in the optical, the ultraviolet and X-rays (see for example Beuermann et al. 2006 and references therein). There is no reported periodic photometric variability for HZ 43 in the literature. However, the observed small photometric variation due to the M dwarf secondary is not relevant with regards to the employment of HZ 43 as a spectroscopic calibration standard. It is not HZ 43 that varies, just the fact that both sources fall on one pixel.

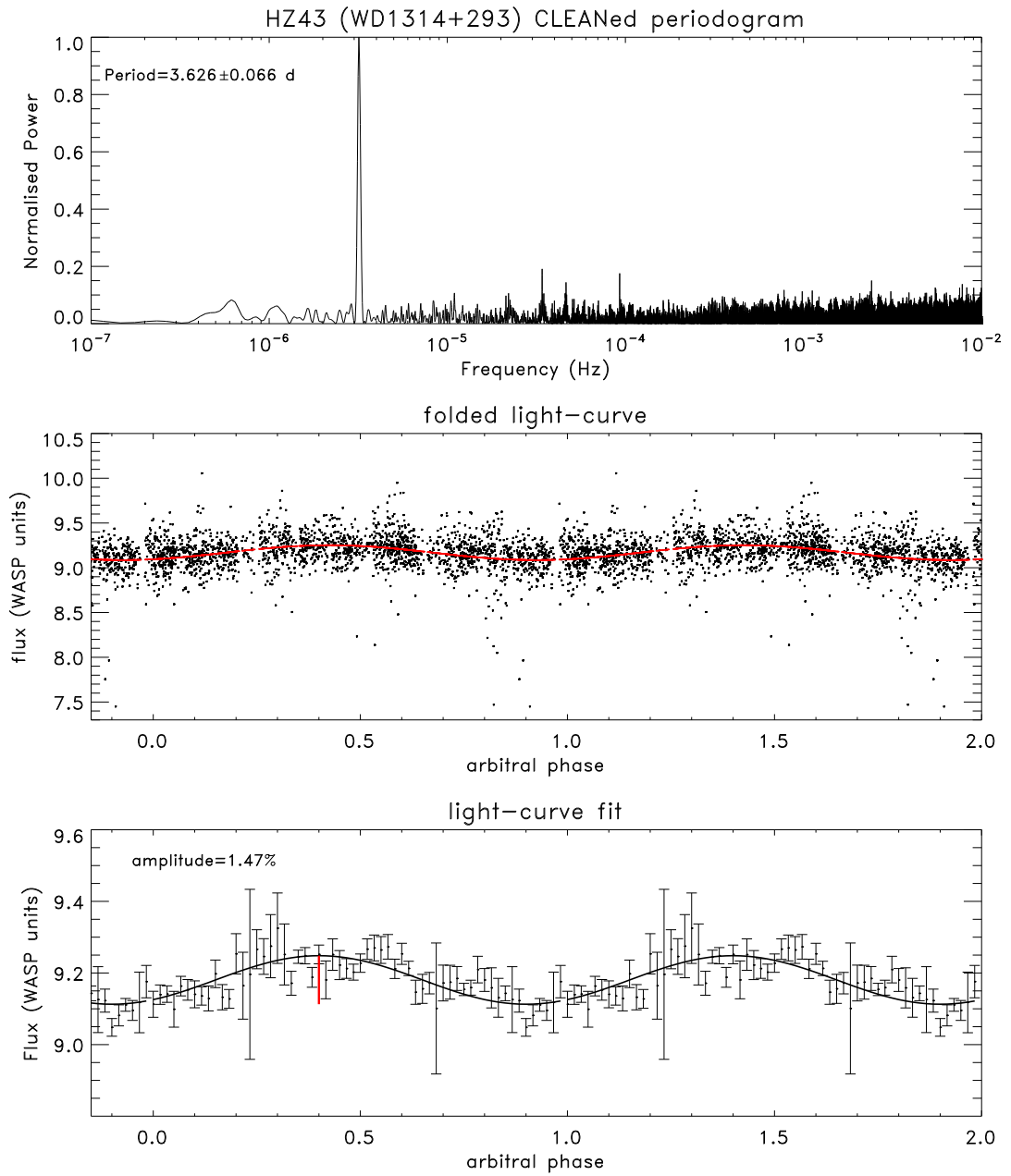


Figure 5.12: As for Figure 5.4 and 5.11. The best fit sine function yields a variation of 1.47%.

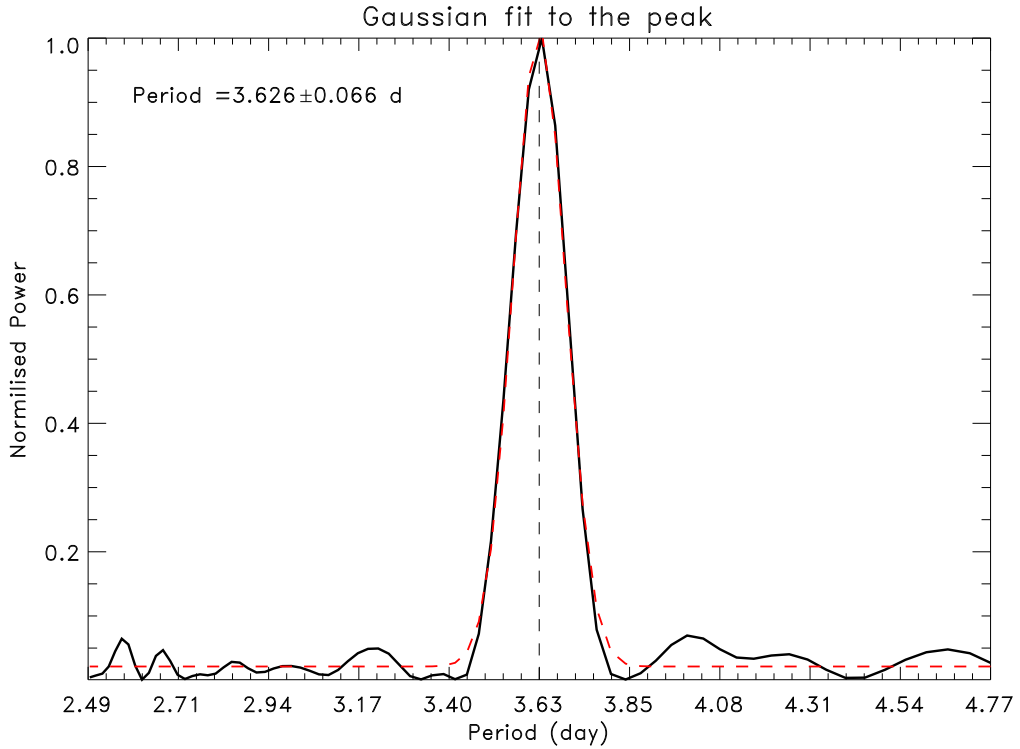


Figure 5.13: Gaussian fit to the peak. I derive the period confidence interval of $\delta P = \pm 0.066\text{d}$ as the width of the best fit function.

5.3.5 GD 358

The following example differs from the previous in that it is a single white dwarf which show photometric variability due to non-radial gravitational pulsations. GD 358 also known as WD1645+325 and 1SWASP J164718.40+322833.0, was the first pulsating star detected based on the theoretical prediction of Winget et al. (1987), of pulsating helium-atmosphere WDs (named DB) and is the star with the largest number of detected periodicities after the Sun. The analysis of stellar pulsations is extremely important to derive the mass and internal composition, which are key parameters for measuring stellar ages and thus the age of our Galaxy. Previous asteroseismological analysis found GD 358 to be variable in the range 1000-2400

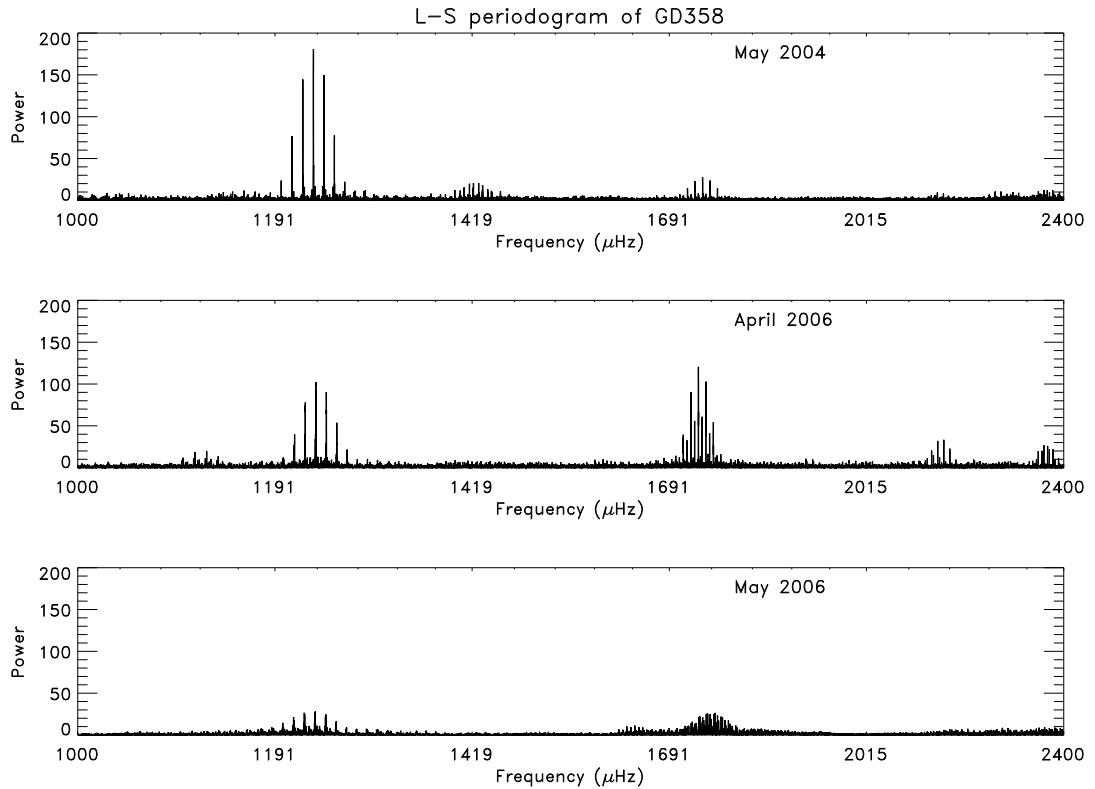


Figure 5.14: I show the L-S periodogram of the source GD 358 over the 2004 (camera 102) and 2006 season (cameras 143 and 147) top to bottom. The L-S spectrum shows the changing in the amplitude of the significant frequencies also changing over the two seasons.

μHz with more than 180 significant peaks (e.g. Kepler et al. 2003 and Winget et al. 1994) continuously changing over time. I used my method and analysed the light-curve of GD 358 over 2004 and 2006 (with 16328 epochs). Because GD 358 is known to be continuously variable I carried out a separate analysis of the 2004 and 2006 datasets. In addition, for the 2006 data I also performed a separate analysis for different cameras. Figure 5.14 shows the L-S periodograms obtained from camera 102 (2004), camera 147 and 143 (2006) in three different panels, top to bottom. Figure 5.14 shows a part of the entire periodogram for the frequency range 1000–2400 μHz . I observe a continuous change in the power of the significant

peaks in the periodogram from season to season as well as a change in the pulsation frequencies. I performed a detailed analysis of the higher peaks in each periodogram to search for previously known modes. Some of the frequencies detected by this work could be related to known oscillations from Kepler et al. (2003) and Winget et al. (1994), however my estimate for the uncertainty on the periods do not allow me to compare these values. For example, in 2006 data for camera 143 I can detect a peak at the period $P = 576.156 \pm 0.012\text{s}$ which could be related to the $k = 12$ and $l = 0$ mode detected at $P = 576.76\text{s}$ by Winget et al. (1994). However, to test for the presence of periodicities belonging to specific k and l modes (e.g. m splitting triplets for each l) requires the use of theoretical models of pulsating DB stars. Nevertheless, my analysis detects the presence of periodicities different from previously published periods over different seasons confirming the ever changing nature of GD 358. In addition, my result proves that SuperWASP telescopes and also future transiting telescopes can be used to study known pulsating white dwarfs to search for period changes, to monitor for planets by timing anomalies and finally to discover new pulsators. I show in Figure 5.15 a magnification of the highest period detected by my analysis of the 2004 data, $P = 811.098 \pm 0.032\text{s}$ (see also Figure 5.14).

5.4 conclusion

In this chapter I have analysed my sample of 194 white dwarfs to search for extrinsic and intrinsic variability. Variable isolated white dwarfs or white dwarfs in binary systems may show photometric variability due to sinusoidal variation for example irradiation or reflection on a low-mass companions, as well as non-sinusoidal variation as in the case of non-radial pulsator such as ZZ Ceti stars. I have developed a

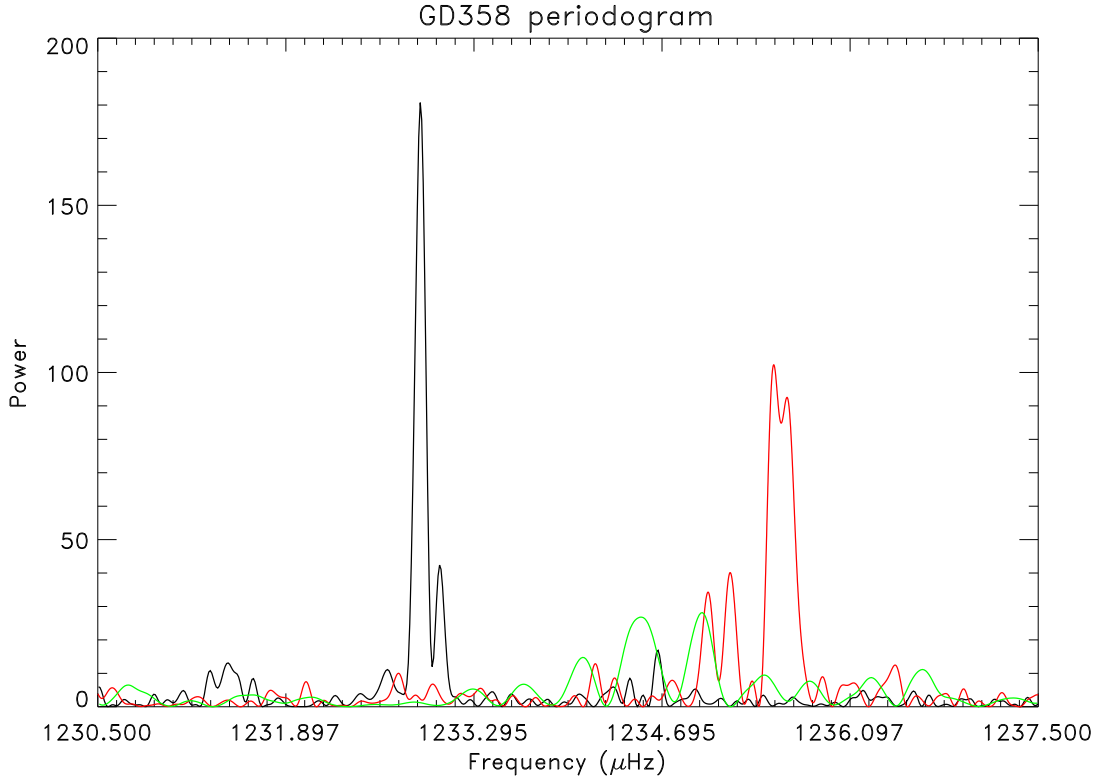


Figure 5.15: magnification around the highest peak detected in 2004 L-S periodogram. Period $P = 811.098 \pm 0.032\text{s}$. Data from the 2004 season are plotted in black. Data from 2006 April are plotted in red and data from 2006 May in green.

period-searching method suited for the characteristics of SuperWASP data (uneven time sampling and large gaps in the data), and that accounts for weak periodic signals. I demonstrated my ability to detect and characterise photometric variable systems with the known source MS Peg (Schmidt et al., 1995). I found that more than $\sim 52\%$ of stars in my sample have periods detected with a 99% confidence, however the majority of the targets are detected at periods close to one day and the day harmonics and sub-harmonic and were therefore discarded for further investigations. Table 5.1 lists the twelve sources that passed visual inspection. I discussed some of the interesting systems found by my period-searching method such as MS

Peg, HZ 43 and WD0353+284. My study found 12 white dwarfs in the sample of 194 stars to show photometric variability. Of those, 6 are known binary systems and 2 are known isolated non-radial pulsators. The remnant 4 stars are not previously known to be photometric variable sources. However, a more detailed analysis of these objects is needed to investigate the nature of their variability and will be the subject of a forthcoming paper (Faedi et al. 2009, in prep.).

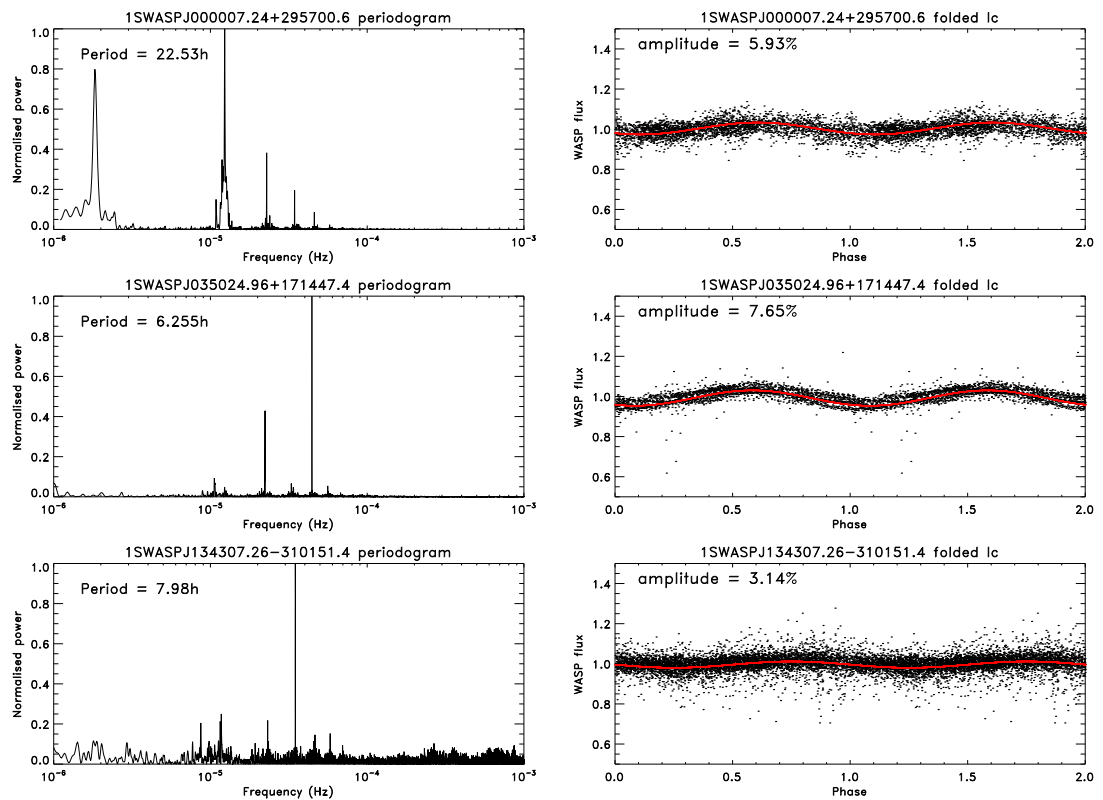


Figure 5.16: CLEANed periodograms and folded light-curves for the sources listed in Table 5.1 that were not studied individually in the chapter. The detected period is indicated in the top-left corner of the periodogram panels. In red is the model fit sine function. I also indicate the amplitude of the photometric variation (%).

1SWASP	WD	name	P (hour)	δP (hour)	A (%)	P_{ajn3} (hour)
J000007.24+295700.6	2357+296	<i>PG2357 + 296</i>	22.530	0.081	5.93	22.57
J035024.96+171447.4	0347+171	<i>V471Tau</i>	6.255	0.004	7.65	6.254
J035705.82+283751.5	0353+284	<i>V1092Tau</i>	8.755	0.008	9.3	8.755
J102712.01+322329.8	1024+326	<i>GSC02511 – 00033</i>	31.962	0.370	4.49	31.962
J131621.95+290556.3	1314+293	<i>HZ43</i>	86.700	0.810	1.47	
J134307.26–310151.4	1340–307	<i>CE356</i>	7.980	0.007	3.14	7.981
J164718.40+322833.0	1645+325	<i>V777Her/GD358</i>	¹ 0.225305	9.010^{-6}		24.14
J181140.81+282939.5	1809+284	<i>GD375</i>	5.978	0.003	7.83	7.96
J194740.52–420026.3	1944–421	<i>V3885Sgr</i>	4.971	0.00	4.37	4.972
J200039.25+014341.9	1958+015	<i>NGC6852</i>	24.912	0.102	5.22	616.65
J215202.73+372617.9	2149+372	<i>GD397</i>	22.590	0.061	6.14	
J225848.13+251544.0	2256+249	<i>MS Peg</i>	4.1682	0.0026	3.11	4.168

Table 5.1: I present the results obtained from my period search for the sample of 194 white dwarfs. From left to right I list the SuperWASP ID, the WD name, other name from SIMBAD, the period and period error from this work and the amplitude, A, of the folded light-curve. In the last column I list the period entry in Table *Period-ajn3* from the SuperWASP archive when available.

¹ GD 358 was first detected with a period of 24.011hours.

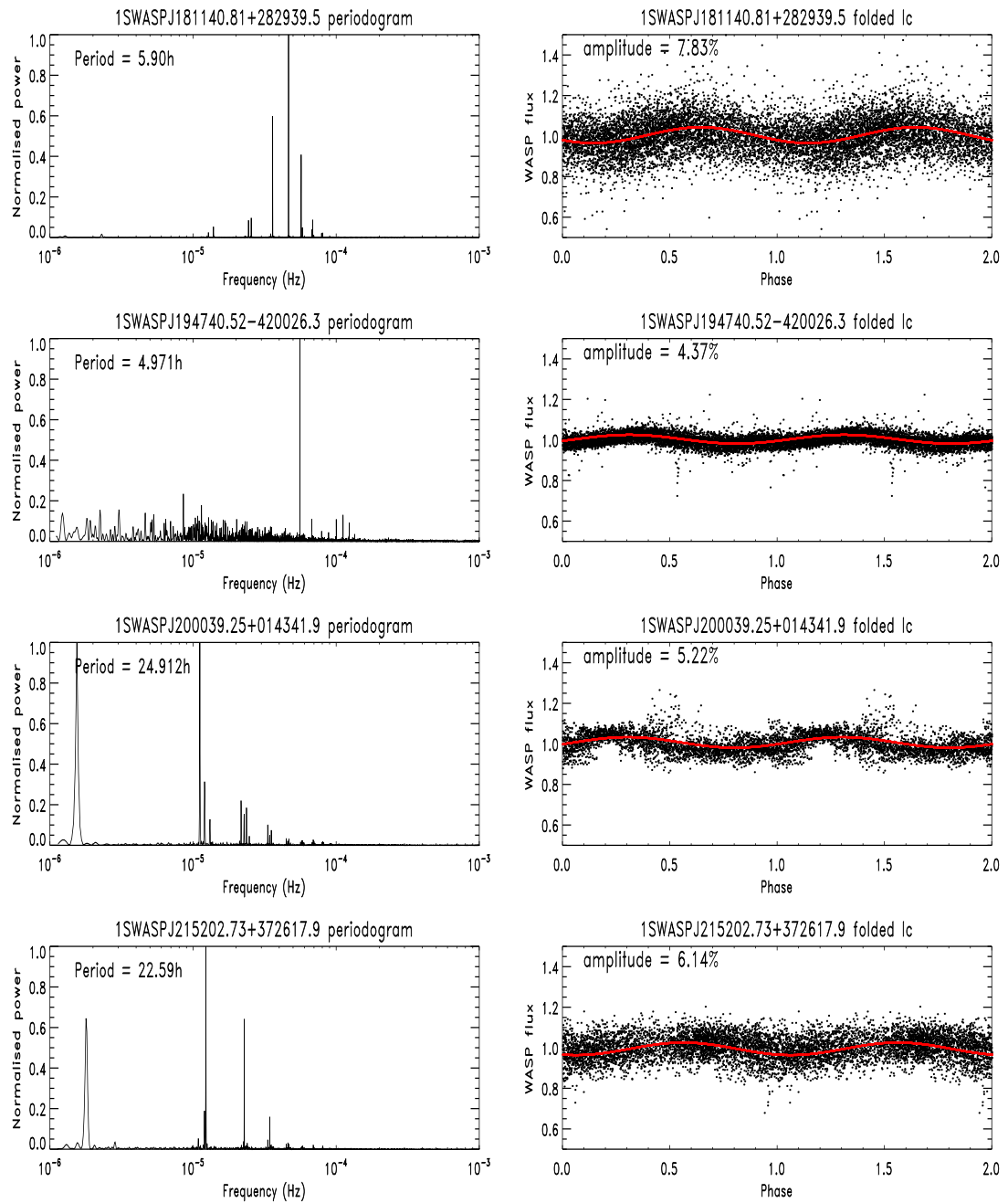


Figure 5.17: continue from Figure 5.16.

Chapter 6

Conclusions and future work

6.1 Conclusions

My thesis has focused on the study of white dwarfs variability by means of data from the ground-based photometric survey SuperWASP. White dwarf stars are known to be photometrically stable stars, however light variations in the observed brightness of these objects can be due for example to the presence of unseen low-mass stellar, sub-stellar and planetary bodies eclipsing or transiting the stellar disc. In addition low-mass stellar companions can also show light-variations due to the reflection and irradiation effects caused by the white dwarf heating the facing hemisphere of the low-mass companion. Finally, white dwarfs can also show photometric variability due to non-radial g-mode pulsations, with timescales of a few hundred seconds, and due to the sporadic onset of star spots on the surface layers of magnetic white dwarfs that rotate in and out of view revealing the star's rotation period.

6.1.1 Sub-stellar and planetary companions to white dwarfs

This work has focused on the study of sub-stellar and planetary companions around white dwarfs. The aim of my thesis was to investigate the possibility of detecting transiting brown dwarfs, gas giants and smaller rocky bodies, in close orbits around white dwarfs, by means of their eclipses and transit signatures in data from current ground-based transit surveys such as SuperWASP. Because white dwarfs have the same size as the Earth, they offer a large gain in relative sizes compared to solar-type stars. Indeed, even rocky bodies smaller than the Moon can yield large transit depths ($\sim 1\%$), detectable in good signal-to-noise light-curves. In addition, because white dwarfs are the end point of stellar evolution for every star less massive than $\sim 8 M_{\odot}$, they offer the unique possibility to investigate planetary survival to the later stages of stellar evolution for every known extra-solar planetary system. This is interesting also for us, as the fate of our own planet during the Sun's red giant phase is uncertain (Rasio et al. 1996; Duncan & Lissauer 1998; and Villaver & Livio 2007).

I have simulated a set of synthetic light-curves using the time sampling and the characteristics of SuperWASP data. I have injected fake transit signals to account for companions ranging from the Moon to a gas giant or a brown dwarf size and from orbital periods between ~ 2 hour and 15 day. I performed extensive simulations to test SuperWASP detection limits for any such system injected in SuperWASP light-curves. I have used my version of the Box-Least Square (BLS) routine to recover the transit signals from the set of simulated light-curves. My implementation of the BLS algorithm is an optimisation that takes into account the characteristics and the shape of the transit signals investigated in this work. Because SuperWASP data

suffer from the presence of residual correlated noise, red noise, even after de-trending by means of powerful techniques such as the Tamuz algorithm (Tamuz et al. 2005), I have explored the BLS recovery rate for data with only Gaussian random noise (white noise), and for red noise data. This also allowed me to test the effect of red noise for transit signals that cover a different parameter space from that of transits of extra-solar planets, e.g. Hot Jupiters around solar-type stars. The results from my simulations show that transits of Moon-sized objects are detectable in data with only random Gaussian noise for a parent white dwarf of magnitude $V \sim 12$. For fainter white dwarfs increasingly larger radius bodies are detectable. My simulations show, that as expected, SuperWASP detection limits are reduced in the presence of red noise (see chapter 3). Nevertheless, Earth-sized companions to white dwarfs remain readily detectable even in low signal-to-noise light-curves. Moreover, in the case of good quality data for which red noise has been importantly reduced by powerful de-trending, Mars and even Mercury sized bodies can yield transits with detectable signal-to-noise (see e.g. Table 3.3, chapter 3).

Encouraged by my results I have investigated a sample of 194 white dwarfs in the SuperWASP survey. This sample is a cross-correlation of the McCook & Sion catalogue (McCook & Sion 2003) and the SuperWASP database. This study to date found no evidence for transits of sub-stellar and terrestrial companions in the light-curves of the 194 stars. My key result allowed me to estimate an upper limit to the frequency of transiting sub-stellar and planetary companions to white dwarfs (see chapter 4).

Although my attempt to find planetary companions to white dwarfs proved fruitless, I emphasise the importance of searching for sub-stellar and planetary companions

to white dwarfs. The results obtained from my research are far from conclusive as very large star samples are needed in order to test sub-stellar and planetary survival to the later stages of stellar evolution. We know that about 2% of isolated white dwarfs have infra-red excesses due to the presence of dust and gas discs (Farihi et al. 2009). Because of the very low transit probability of rocky planetary companions to white dwarfs (less than few percent see Figure 3.3, chapter 3) I need a target sample at least ten times larger than mine.

Future surveys such as Pan-STARRS (<http://pan-starrs.ifa.hawaii.edu/public>) and LSST (<http://www.lsst.org/lsst>) capable of detecting tens of thousands of white dwarfs will allow us to test sub-stellar and planetary survival. However, my work has demonstrated that observations of very high cadence and long baseline are needed to detect the signature of transiting systems such as in the case investigated in this work. Future space missions such as PLATO might also offer the possibility of detecting these systems. The PLATO mission (<http://www.lesia.obspm.fr/perso/claude-catala/plato>), will observe stars to a magnitude limit similar to that of SuperWASP, but will observe the same field continuously for very long periods and without interruption. This will provide well sampled light-curves of very long baseline with no observational gaps and might yield the detection of small rocky bodies around white dwarfs. My results have shown that terrestrial planetary bodies with sizes comparable to Mars and even Mercury can yield detectable transit signatures in SuperWASP light-curve.

6.1.2 WDs variability

As part of my research I have also studied the sample of 194 white dwarfs to search for photometric variability due to star spots, non-radial pulsations and or to the presence of low-mass stellar companions showing the effects of irradiation and reflection. I have analysed each target using multiple period-searching techniques: the Lomb-Scargle (Lomb 1976; Scargle 1982) modified periodogram and the CLEAN algorithm (Roberts et al. 1987; Foster 1995) are designed to detect weak periods in unevenly spaced datasets showing sinusoidal variability. The Phase Dispersion Minimisation (PDM) technique (Stellingwerf 1978) can be very efficient in identifying non-sinusoidal variability. Finally, I have performed a visual inspection of each folded light-curve to identify periods due to residual systematic effects such as gaps due to the day-night alternation and/or to residuals affecting groups of targets in a field (for example residual Moon-light variation). I considered a period successfully detected if it was recovered using two of the methods above within an interval of 0.003d from each other.

I find more than $\sim 52\%$ of stars in my sample to have periods detected with a 99% confidence, however the majority of the targets are detected at periods close to one day and the day harmonics and sub-harmonics and were therefore discarded for further investigations. My study finds just 12 variable white dwarfs in a sample of 194 stars. Of those, 6 are known binary systems and 2 are known isolated non-radial pulsators. The remaining 4 stars were not previously known to be photometrically variable sources. However, a more detailed analysis of these objects is needed to investigate the nature of their variability and will be the subject of a forthcoming paper (Faedi et al. 2009, in prep.).

6.2 Future work

6.2.1 A search for hidden white dwarfs by occultations due to low-mass stellar companions

Motivated by my previous work I aim to extend my search for white dwarf companions into the stellar regime. Following the discovery of the eclipsing system DE CVn (van den Besselaar et al., 2007), where the white dwarf is optically undetectable, I have searched and detected the system's eclipses by means of my implementation of the BLS routine. Encouraged by my independent detection of DE CVn, I aim to detect more such systems. This will allow me to put constraints on the true frequency of close stellar companions to white dwarfs.

Large gaps in our knowledge of binary stellar evolution affect our understanding of evolved compact objects as well as of phenomena such as supernovae type Ia explosions. The poorly understood phase of common envelope (CE) evolution results in considerable uncertainties in binary evolution models (Willems & Kolb 2004). During the CE phase the more massive component in a binary evolves into a red giant. When the binary initial orbital period is ≤ 10 years, the envelope of the giant will encompass the secondary star. This forces the secondary and the core of the primary to spiral towards each other (see Paczynski 1976 and Iben & Livio 1993 for a review). Due to the very short duration of the CE phase (≤ 1000 years; Taam & Sandquist 2000) it is virtually impossible to directly observe this phase. However we can constrain models of CE evolution by studying systems that have undergone CE evolution in the past. Eclipsing binary systems with white dwarf primaries are

extremely helpful in this regard. A detailed analyses of the light-curves and radial velocity curves of such systems would allow precise physical parameters including masses, radii and orbital distances to be derived. By fixing these parameters more accurate models can be derived to test the data. Moreover the evolution of close post CE binary systems (PCEBs) and in particular, cataclysmic variable systems (CVs), is governed by angular momentum loss (AML) driven by the combination of gravitational radiation (for periods $< 3h$), and magnetic braking (for periods $> 3h$) (King 1988; Verbunt & Zwaan 1981). Both mechanisms are not well understood (Taam & Sandquist 2000). Therefore the detection of more such systems will help to test models of close binary evolution theory as well as shedding light on the period distribution features, the period gap and the period minimum. Politano & Weiler (2006) suggest that observations of masses and spectral types of PCEBs can be sufficient to confirm or disprove the magnetic braking model.

The known population of PCEBs appears to be biased towards hot/young white dwarfs, because the degenerate component has been detected as a blue optical or soft X-ray source, the major discovery channel for PCEBs. Schreiber & Gänsicke (2003) predicted the existence of a large, currently undiscovered, population of old PCEBs containing cold/old white dwarfs contributing only to a small fraction of the optical emission of the system. These systems will be rejected when using colour based selection criteria. New detections of eclipsing binary systems with a cold WD primary component, such as DE CVn ($T_{\text{eff}} = 8000\text{K}$ see van den Besselaar et al. 2007), will help test population synthesis models. Their characteristics will allow us to better define their space densities as a function of composition, e.g. white dwarf temperature, spectral type and age.

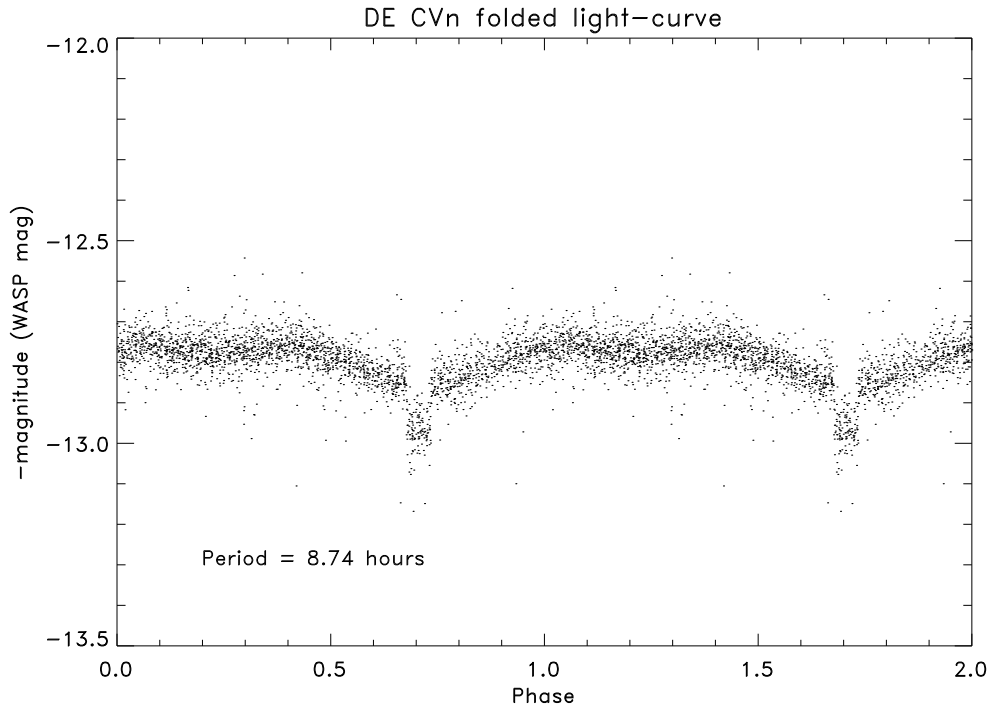


Figure 6.1: Folded light-curve of DE CVn on the orbital period ~ 8.74 hours detected using my implementation of the BLS algorithm. The Figure shows the eclipses of the white dwarf by means of the M dwarf.

6.2.2 Technique

I aim to search the SuperWASP list of red dwarf counterparts for eclipses by means of the BLS algorithm. I expect white dwarfs to show eclipses characterised by a squared shape with sharp ingress and egress (see for example the eclipses of the WD in the system NN Ser, Brinkworth et al. 2006), and the eclipse depth to be a few tenths of a magnitude, (e.g. Figure 6.1). The eclipse will be of short duration, between a few to a few tens of minutes, and will show strong colour dependence and out-of-eclipse variability. I set the range of orbital periods to be between 2 hours and 15 days, my implementation of the BLS algorithm is optimised to account for eclipses of short duration. I have already shown that the SuperWASP data are of

sufficient quality to allow me to search for such binary systems (Figure 6.1). In addition the simulations from my thesis work, show that I am able to recover very short, (1 to 35 minutes), and deep eclipses (from $\sim 3\%$ to 100%) in SuperWASP light-curves. I have tested this approach with two known PCEB systems DE CVn (Figure 6.1) and V471 Tau (Figure 6.2) (van den Besselaar et al. 2007; Kamiński et al. 2007).

DE CVn is a WD + M3V dwarf eclipsing binary system in a ~ 8.7 hours orbit, with a magnitude of $V \simeq 12.8$. The white dwarf in this system is spectroscopically unseen, therefore this object is excluded from the list of 194 SuperWASP white dwarfs previously searched. However the source has been observed by SuperWASP in two fields. This eclipsing binary is easily identified in the SuperWASP light-curve using my implementation of the BLS algorithm. My independent detection of the correct orbital period shows my ability to detect eclipses of WDs by low-mass stellar companions even in the presence of out-of-eclipse variability. For DE CVn such variability is due to the heating effect the white dwarf has on the M dwarf, which is tidally locked. I note that this kind of variability appears to be quite stable in time. Figure 6.1 shows the light-curve of DE CVn folded on the orbital period. My independent detection of DE CVn certify the possibility of detecting new EB systems with unseen cold/old white dwarf primary components that seem to be missed in the population of post common envelope binaries as discussed by (Schreiber & Gänsicke, 2003).

The binary system V471 Tau consists of a WD + K2V dwarf. It is a candidate pre-CV eclipsing binary system of magnitude $V \simeq 9.5$ (Kamiński et al. 2007). The light-curve of V471 Tau is dominated by the sinusoidal variability due to the presence

of star spots on the secondary. In this case too, the white dwarf in the system is optically invisible, hidden in the glare of the secondary, although hot enough to outshine the K dwarf in the UV. I used the BLS algorithm to search for eclipses, and detected a significant peak in the BLS power spectrum with a period of 12.5 hours. However, upon initial inspection of the phase-folded light-curve the eclipse was visible only when plotting the data in sections with duration of about 28 days. This reduced the effect of the change in the intensity of the star spots' revealing the WD eclipse. Figure 6.2 shows the light-curve of V471 Tau folded on the orbital period of 12.5 hours. For V471 Tau the orbital period and the spots' period are the same because the two stars are tidally locked. My analysis of V471 Tau shows that WD eclipses due to low-mass stellar companions are detectable in SuperWASP data. It also suggests that a better approach for the detection of the eclipse in these systems would be to fit and remove any sinusoidal variability before searching for the eclipse signature using a BLS algorithm. This is true in particular for binary systems where the two components are not in synchronous rotation.

I will perform a cost-benefit analyses of such a method. I aim to search for SuperWASP counterparts in the list of all known PCEB binaries from Morales-Rueda et al. (2005). I will use this sample (e.g. V471 Tau and DE CVn are in Morales-Rueda list) to test my two-step detection method, and so investigate my ability to detect the white dwarf occultation.

I aim to investigate my ability to identify new WD + red dwarf binary systems. I will compile a list of all known nearby/bright red dwarfs spectral type K and M from on-line catalogues, such as the Gliese catalogue (Gliese & Jahreiss 1995), that I will cross-correlate with the SuperWASP data archive. The resultant list of SuperWASP

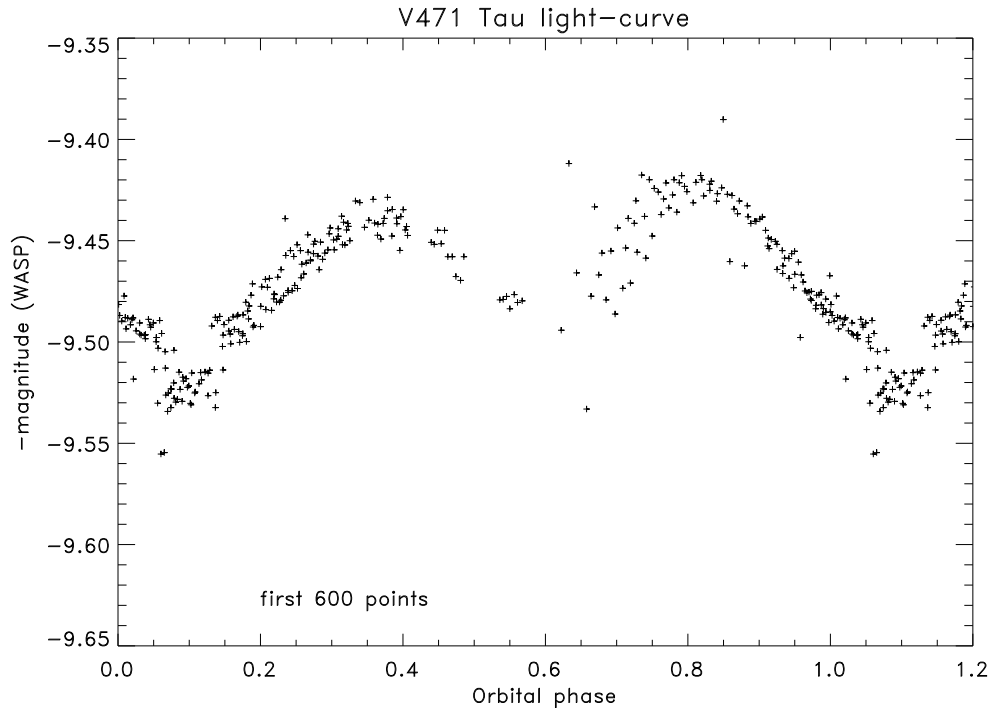


Figure 6.2: V471 Tau folded light-curve on the orbital period 12.5 hours. The variability is due to the presence of star spots in the secondary. This plot shows the first 600 data points of the time series, that span ~ 28 days. The transit remain hidden by the spots variability when folding the entire light-curve.

counterparts will then be searched for eclipsing unseen companions using my method outlined above. New PECB systems with secondary of spectral type K and M might be discovered as suggested by the example discussed above.

Finally, once tested, I can also apply my two-step detection method to the SuperWASP planet program. The stellar variability due to the presence of spots in the star surface is one of the causes of contamination when searching for extrasolar planet transits around main sequence stars. The spots' variability can be important enough to hide the transit signal and leave the planet undetected. I first encountered this problem with V471 Tau.

BIBLIOGRAPHY

Adams W. S., 1915, PASP, 27, 236

Adelman S. J., 2004, in J. Zverko, J. Ziznovsky, S. J. Adelman, & W. W. Weiss ed., The A-Star Puzzle Vol. 224 of IAU Symposium, The physical properties of normal A stars. pp 1–11

Agol E., Cowan N. B., Bushong J., Knutson H., Charbonneau D., Deming D., Steffen J. H., 2009, in IAU Symposium Vol. 253, Transits and secondary eclipses of HD 189733 with Spitzer. pp 209–215

Alcock C., 2000, Science, 287, 74

Alcock C., Allsman R. A., Axelrod T. S., Bennett D. P., Cook K. H., Park H. S., Marshall S. L., Stubbs C. W., Griest K., Perlmutter S., Sutherland W., Freeman K. C., Peterson B. A., Quinn P. J., Rodgers A. W., 1993, in Soifer B. T., ed., Sky Surveys. Protostars to Protogalaxies Vol. 43 of Astronomical Society of the Pacific Conference Series, The MACHO Project - a Search for the Dark Matter in the Milky-Way. pp 291–+

- Alonso R., Brown T. M., Torres G., Latham D. W., Sozzetti A., Mandushev G., Belmonte J. A., Charbonneau D., Deeg H. J., Dunham E. W., O'Donovan F. T., Stefanik R. P., 2004, *ApJ*, 613, L153
- Arnold L., Gillet S., Lardièrre O., Riaud P., Schneider J., 2002, EGS XXVII General Assembly, Nice, 21-26 April 2002, abstract #5082, 27, 5082
- Bakos G., Noyes R. W., Kovács G., Stanek K. Z., Sasselov D. D., Domsa I., 2004, *PASP*, 116, 266
- Bakos G. Á., et al., 2007, *ApJ*, 656, 552
- Bakos G. Á., et al., 2009, *ArXiv e-prints*
- Barge P., Baglin A., Auvergne M., Buey J.-T., Catala C., Michel E., Weiss W. W., Deleuil M., Jorda L., Moutou C., COROT Team 2005, in Casoli F., Contini T., Hameury J. M., Pagani L., eds, *SF2A-2005: Semaine de l'Astrophysique Francaise CoRoT: a first space mission to find terrestrial planets*. pp 193–+
- Barron J. T., Stumm C., Hogg D. W., Lang D., Roweis S., 2008, *AJ*, 135, 414
- Barstow M. A., Bond H. E., Holberg J. B., Burleigh M. R., Hubeny I., Koester D., 2005, *MNRAS*, 362, 1134
- Barstow M. A., Jordan S., O'Donoghue D., Burleigh M. R., Napiwotzki R., Harrop-Allin M. K., 1995, *MNRAS*, 277, 971
- Beaulieu J.-P., et al., 2006, *Nature*, 439, 437
- Becklin E. E., Zuckerman B., 1988, *Nature*, 336, 656

- Benedict G. F., McArthur B. E., Forveille T., Delfosse X., Nelan E., Butler R. P., Spiesman W., Marcy G., Goldman B., Perrier C., Jefferys W. H., Mayor M., 2002, *ApJ*, 581, L115
- Bennett D. P., et al., 2008, *ApJ*, 684, 663
- Bergeron P., Ruiz M.-T., Leggett S. K., 1994, in *Bulletin of the American Astronomical Society* Vol. 26 of *Bulletin of the American Astronomical Society*, *The Chemical Evolution of Very Cool White Dwarfs*. pp 1470–+
- Bergeron P., Saumon D., Wesemael F., 1995, *ApJ*, 443, 764
- Beuermann K., Burwitz V., Rauch T., 2006, *A&A*, 458, 541
- Borucki W. J., Koch D. G., Jenkins J. M., 2001, in *Bulletin of the American Astronomical Society* Vol. 33 of *Bulletin of the American Astronomical Society*, *Detection by Transit Photometry*. pp 1479–+
- Boss L., 1910, *Preliminary General Catalogue of 6188 stars for the epoch 1900*
- Brinkworth C. S., Marsh T. R., Dhillon V. S., Knigge C., 2006, *MNRAS*, 365, 287
- Brinkworth C. S., Marsh T. R., Morales-Rueda L., Maxted P. F. L., Burleigh M. R., Good S. A., 2005, *MNRAS*, 357, 333
- Brown T. M., 2001, *ApJ*, 553, 1006
- Brown T. M., 2003, *ApJ*, 593, L125
- Brown T. M., Charbonneau D., 2000, in Garzón G., Eiroa C., de Winter D., Mahoney T. J., eds, *Disks, Planetesimals, and Planets* Vol. 219 of *Astronomical Society of the Pacific Conference Series*, *The STARE Project: a Transit Search for Hot Jupiters*. pp 584–+

- Burgasser A. J., Kirkpatrick J. D., Reid I. N., Brown M. E., Miskey C. L., Gizis J. E., 2003, *ApJ*, 586, 512
- Burke C. J., Gaudi B. S., DePoy D. L., Pogge R. W., 2006, *AJ*, 132, 210
- Burleigh M. R., Clarke F. J., Hodgkin S. T., 2002, *MNRAS*, 331, L41
- Burleigh M. R., et al., 2006, *MNRAS*, 373, 1416
- Calchi Novati S., et al., 2005, *A&A*, 443, 911
- Cameron A. C., et al., 2007, *MNRAS*, 375, 951
- Cassinelli J. P., 1979, *ARA&A*, pp 275–308
- Castor J. I., 1981, in Iben Jr. I., Renzini A., eds, *Physical Processes in Red Giants* Vol. 88 of *Astrophysics and Space Science Library*, Origin of winds in cool giants and supergiants. pp 285–299
- Chandrasekhar S., 1935, *MNRAS*, 95, 676
- Charbonneau D., 2008, in *Bulletin of the American Astronomical Society* Vol. 40 of *Bulletin of the American Astronomical Society*, Observational Constraints on the Chemistry and Dynamics of Exoplanet Atmospheres. pp 463–+
- Charbonneau D., Brown T. M., Burrows A., Laughlin G., 2007, in Reipurth B., Jewitt D., Keil K., eds, *Protostars and Planets V* When Extrasolar Planets Transit Their Parent Stars. pp 701–716
- Chauvin G., Lagrange A.-M., Dumas C., Zuckerman B., Mouillet D., Song I., Beuzit J.-L., Lowrance P., 2004, *A&A*, 425, L29

Chauvin G., Lagrange A.-M., Dumas C., Zuckerman B., Mouillet D., Song I., Beuzit J.-L., Lowrance P., 2005, *A&A*, 438, L25

Collier Cameron A., et al., 2006, *MNRAS*, 373, 799

Collier Cameron A., et al., 2007, *MNRAS*, 380, 1230

Dantona F., Mazzitelli I., 1978, *A&A*, 66, 453

Debes J. H., Sigurdsson S., 2002, *ApJ*, 572, 556

Deming D., Brown T. M., Charbonneau D., Harrington J., Richardson L. J., 2005, *ApJ*, 622, 1149

Deming D., Harrington J., Laughlin G., Seager S., Navarro S. B., Bowman W. C., Horning K., 2007, *ApJ*, 667, L199

Dong S., et al., 2009, *ApJ*, 698, 1826

Dufour P., Liebert J., Fontaine G., Behara N., 2007, *Nature*, 450, 522

Duncan M. J., Lissauer J. J., 1998, *Icarus*, 134, 303

Dunham E. W., Mandushev G. I., Taylor B. W., Oetiker B., 2004, *PASP*, 116, 1072

Eddington A. S., 1924, *MNRAS*, 84, 308

Eisenstein D. J., et al., 2006, *ApJ*, 167, 40

Faber S. M., Gallagher J. S., 1979, *ARA&A*, 17, 135

Farihi J., Becklin E. E., Zuckerman B., 2005, *ApJ*, 161, 394

Farihi J., Jura M., Zuckerman B., 2009, *ArXiv e-prints*

- Farihi J., Zuckerman B., Becklin E. E., 2008, *ApJ*, 674, 431
- Farihi J., Zuckerman B., Becklin E. E., Jura M., 2007, in Napiwotzki R., Burleigh M. R., eds, *Astronomical Society of the Pacific Conference Series Vol. 372, Spitzer Observations of GD 362 and Other Metal-Rich White Dwarfs*. p. 315
- Ferrario L., Vennes S., Wickramasinghe D. T., Bailey J. A., Christian D. J., 1997, *MNRAS*, 292, 205
- Ferrario L., Wickramasinghe D. T., 2007, in Napiwotzki R., Burleigh M. R., eds, *15th European Workshop on White Dwarfs Vol. 372 of Astronomical Society of the Pacific Conference Series, High Field Magnetic White Dwarfs, Pulsars, Magnetars, and their Main Sequence Progenitors*. pp 163–+
- Fontaine G., Brassard P., 2008, *PASP*, 120, 1043
- Fontaine G., Brassard P., Bergeron P., 2001, *PASP*, 113, 409
- Fontaine G., Lacombe P., McGraw J. T., Dearborn D. S. P., Gustafson J., 1982, *ApJ*, 258, 651
- Ford E. B., 2006, in Kannappan S. J., Redfield S., Kessler-Silacci J. E., Landriau M., Drory N., eds, *New Horizons in Astronomy: Frank N. Bash Symposium Vol. 352 of Astronomical Society of the Pacific Conference Series, What Do Multiple Planet Systems Teach Us about Planet Formation?*. pp 15–+
- Foster G., 1995, *AJ*, 109, 1889
- Fowler R. H., 1926, *MNRAS*, 87, 114
- Frink S., Mitchell D. S., Quirrenbach A., Fischer D. A., Marcy G. W., Butler R. P., 2002, *ApJ*, 576, 478

- Gänsicke B. T., Marsh T. R., Southworth J., Rebassa-Mansergas A., 2006, *Science*, 314, 1908
- Gänsicke B. T., Marsh T. R., Southworth J., Rebassa-Mansergas A., 2007, *ArXiv e-prints*, 710
- Gaudi B. S., et al., 2008, *Science*, 319, 927
- Gaudi B. S., Seager S., Mallen-Ornelas G., 2005, *ApJ*, 623, 472
- Genova R., Bowyer S., Vennes S., Lieu R., Henry J. P., Gioia I., 1995, *AJ*, 110, 788
- Gliese W., Jahreiss H., 1995, *VizieR Online Data Catalog*, 5070, 0
- Graham J. R., Macintosh B., Doyon R., Gavel D., Larkin J., Levin M., Oppenheimer B., Palmer D., Saddlemyer L., Sivaramakrishnan A., Veran J., Wallace K., Gemini Planet Imager Science Team 2007, in *Bulletin of the American Astronomical Society Vol. 38 of Bulletin of the American Astronomical Society, Ground-Based Direct Detection of Exoplanets with the Gemini Planet Imager (GPI)*. pp 968–+
- Greenstein J. L., Oke J. B., Shipman H. L., 1971, *ApJ*, 169, 563
- Grillmair C. J., Charbonneau D., Burrows A., Armus L., Stauffer J., Meadows V., Van Cleve J., Levine D., 2007, *ApJ*, 658, L115
- Hatzes A. P., Guenther E. W., Endl M., Cochran W. D., Döllinger M. P., Bedalov A., 2005, *A&A*, 437, 743
- Hebb L., et al., 2008, *ArXiv e-prints*
- Hog E., Fabricius C., Makarov V. V., Urban S., Corbin T., Wycoff G., Bastian U., Schwekendiek P., Wicenc A., 2000, *VizieR Online Data Catalog*, 1259, 0

- Holberg J. B., 2007, in Napiwotzki R., Burleigh M. R., eds, 15th European Workshop on White Dwarfs Vol. 372 of Astronomical Society of the Pacific Conference Series, White Dwarfs as Photometric Calibrators of Large Surveys. pp 145–+
- Holberg J. B., Barstow M. A., Bruhweiler F. C., Cruise A. M., Penny A. J., 1998, *ApJ*, 497, 935
- Holberg J. B., Barstow M. A., Green E. M., 1997, *ApJ*, 474, L127+
- Holberg J. B., Bergeron P., 2006, *AJ*, 132, 1221
- Horne J. H., Baliunas S. L., 1986, *ApJ*, 302, 757
- Horne K., 2003, in Deming D., Seager S., eds, Scientific Frontiers in Research on Extrasolar Planets Vol. 294 of Astronomical Society of the Pacific Conference Series, Status and Prospects of Planetary Transit Searches: Hot Jupiters Galore. pp 361–370
- Horne K., 2006, in N. Solomos ed., Recent Advances in Astronomy and Astrophysics Vol. 848 of American Institute of Physics Conference Series, The Quest for Extrasolar Planets. pp 787–799
- Huegelmeier S. D., Dreizler S., 2009, ArXiv e-prints
- Iben Jr. I., Renzini A., 1983, *ARA&A*, 21, 271
- Iben I. J., 1965, *ApJ*, 142, 1447
- Iben I. J., Laughlin G., 1989, *ApJ*, 341, 312
- Iben I. J., Livio M., 1993, *PASP*, 105, 1373
- Ida S., Lin D. N. C., 2008, *ApJ*, 685, 584

- Jeans J. H., 1924, MNRAS, 85, 2
- Jeffries R. D., Burleigh M. R., Robb R. M., 1996, A&A, 305, L45+
- Johnson J. B., 1925, Phys. Rev., 26, 71
- Jura M., 2003, ApJ, 584, L91
- Jura M., 2008, AJ, 135, 1785
- Jura M., Farihi J., Zuckerman B., 2009, AJ, 137, 3191
- Kalas P., Fitzgerald M. P., Clampin M., Graham J. R., Chiang E., Kite E. S., Stapelfeldt K., Krist J., 2009, in Bulletin of the American Astronomical Society Vol. 41 of Bulletin of the American Astronomical Society, Fomalhaut b: Direct Detection of a ϵ Jupiter-mass Object Orbiting Fomalhaut. pp 491–+
- Kamiński K. Z., Ruciński S. M., Matthews J. M., Kuschnig R., Rowe J. F., Guenther D. B., Moffat A. F. J., Sasselov D., Walker G. A. H., Weiss W. W., 2007, AJ, 134, 1206
- Kane S. R., Collier Cameron A., Horne K., James D., Lister T. A., Pollacco D. L., Street R. A., Tsapras Y., 2005, MNRAS, 364, 1091
- Kane S. R., Horne K., Lister T., Cameron A. C., Street R. A., Pollacco D. L., James D., Tsapras Y., 2004, in Beaulieu J., Lecavelier Des Etangs A., Terquem C., eds, Extrasolar Planets: Today and Tomorrow Vol. 321 of Astronomical Society of the Pacific Conference Series, Recent Results from the Wide Angle Search for Planets (WASP) Prototype. pp 115–+
- Kepler S. O., et al., 2003, A&A, 401, 639

- King A. R., 1988, QJRAS, 29, 1
- Kipping D. M., 2008, MNRAS, 389, 1383
- Knox R. A., Hawkins M. R. S., Hambly N. C., 1999, MNRAS, 306, 736
- Knutson H., Charbonneau D., 2009, in American Astronomical Society Meeting Abstracts Vol. 214 of American Astronomical Society Meeting Abstracts, Confirmation and Characterization of Kepler Mission Exoplanets: The Era of Rock and Ice Exoplanets
- Knutson H. A., 2008, in Fischer D., Rasio F. A., Thorsett S. E., Wolszczan A., eds, Astronomical Society of the Pacific Conference Series Vol. 398 of Astronomical Society of the Pacific Conference Series, Mapping the Atmospheres of Hot Jupiters. pp 363–+
- Koch D., Borucki W., 1996, in Doyle L. R., ed., Circumstellar Habitable Zones A Search For Earth-Sized Planets In Habitable Zones Using Photometry. pp 229–+
- Koester D., 2002, A&A, 11, 33
- Koester D., Chanmugam G., 1990, Reports on Progress in Physics, 53, 837
- Koester D., Provencal J., Shipman H. L., 1997, A&A, 320, L57
- Koester D., Rollenhagen K., Napiwotzki R., Voss B., Christlieb N., Homeier D., Reimers D., 2005, A&A, 432, 1025
- Kotak R., van Kerkwijk M. H., Clemens J. C., Koester D., 2003, A&A, 397, 1043
- Kovács G., Zucker S., Mazeh T., 2002, A&A, 391, 369
- Kruger A. T., Loredó T. J., Wasserman I., 2002, ApJ, 576, 932

- Larson R. B., 1987, *Comments on Astrophysics*, 11, 273
- Leggett S. K., Ruiz M. T., Bergeron P., 1998, *ApJ*, 497, 294
- Liebert J., Dahn C. C., Gresham M., Strittmatter P. A., 1979, *ApJ*, 233, 226
- Liebert J., Dahn C. C., Monet D. G., 1988, *ApJ*, 332, 891
- Lineweaver C. H., Grether D., 2003, *ApJ*, 598, 1350
- Littlefair S. P., Dhillon V. S., Marsh T. R., Gänsicke B. T., Southworth J., Watson C. A., 2006, *Science*, 314, 1578
- Littlefair S. P., Dhillon V. S., Martín E. L., 2003, *MNRAS*, 340, 264
- Lomb N. R., 1976, *Ap&SS*, 39, 447
- Luyten W., 1970, *White dwarfs*
- Luyten W. J., 1922a, *PASP*, 34, 54
- Luyten W. J., 1922b, *PASP*, 34, 156
- Luyten W. J., 1950, *AJ*, 55, 86
- Malo A., Wesemael F., Bergeron P., 1999, *ApJ*, 517, 901
- Marcy G., Butler R. P., Fischer D., Vogt S., Wright J. T., Tinney C. G., Jones H. R. A., 2005, *Progress of Theoretical Physics Supplement*, 158, 24
- Margon B., Liebert J., Lampton M., Spinrad H., Bowyer S., Gatewood G., 1976, *ApJ*, 209, 525
- Marois C., Macintosh B., Barman T., Zuckerman B., Song I., Patience J., Lafrenière D., Doyon R., 2008, *Science*, 322, 1348

- Marquardt D. W., 1963, *SIAM Journal on Applied Mathematics*, 11, 431
- Matsakis D. N., Taylor J. H., Eubanks T. M., 1997, *A&A*, 326, 924
- Maxted P. F. L., Napiwotzki R., Dobbie P. D., Burleigh M. R., 2006, *Nature*, 442, 543
- Mayor M., Bonfils X., Forveille T., Delfosse X., Udry S., Bertaux J. ., Beust H., Bouchy F., Lovis C., Pepe F., Perrier C., Queloz D., Santos N. C., 2009, *ArXiv e-prints*
- Mayor M., et al., 2003, *The Messenger*, 114, 20
- Mayor M., Queloz D., 1995, *Nature*, 378, 355
- Mazzitelli I., Dantona F., 1986, *ApJ*, 311, 762
- McAlister H. A., Mason B. D., Hartkopf W. I., Roberts Jr. L. C., Shara M. M., 1996, *AJ*, 112, 1169
- McCarthy C., Zuckerman B., 2004, *AJ*, 127, 2871
- McCook G. P., Sion E. M., 2003, *VizieR Online Data Catalog*, 3235, 0
- McCullough P. R., Regan M., Figer D., Lindsay K., Morse E., Stockman H., Rauscher B. J., Hill R. J., 2005, in *Bulletin of the American Astronomical Society* Vol. 37 of *Bulletin of the American Astronomical Society*, *The Quantum Efficiency of JWST Near-infrared Detectors*. pp 1351–+
- McGraw J. T., 1979, *ApJ*, 229, 203
- Mestel L., 1952, *MNRAS*, 112, 583
- Monet D. G., et al., 2003, *AJ*, 125, 984

- Montgomery M. H., Williams K. A., Winget D. E., Dufour P., DeGennaro S., Liebert J., 2008, *ApJ*, 678, L51
- Morales-Rueda L., Marsh T. R., Maxted P. F. L., Nelemans G., Karl C., Napiwotzki R., Moran C. K. J., 2005, *MNRAS*, 359, 648
- Mouillet D., et al., 2009, in Moorwood A., ed., *Science with the VLT in the ELT Era SPHERE: A ‘Planet Finder’ Instrument for the VLT*. pp 337–+
- Mukadam A. S., Gänsicke B. T., Szkody P., Aungwerojwit A., Howell S. B., Fraser O. J., Silvestri N. M., 2007, *ApJ*, 667, 433
- Mullally F., Winget D. E., Degennaro S., Jeffery E., Thompson S. E., Chandler D., Kepler S. O., 2008, *ApJ*, 676, 573
- Napiwotzki R., Barstow M. A., Fleming T., Holweger H., Jordan S., Werner K., 1993, *A&A*, 278
- Norton A. J., et al., 2007, *A&A*, 467, 785
- Oppenheimer B. R., Hambly N. C., Digby A. P., Hodgkin S. T., Saumon D., 2001, *Science*, 292, 698
- Ostriker J. P., Peebles P. J. E., 1973, *ApJ*, 186, 467
- Paczynski B., 1971, *ARA&A*, 9, 183
- Paczynski B., 1976, in Eggleton P., Mitton S., Whelan J., eds, *Structure and Evolution of Close Binary Systems IAU Symposium, Common Envelope Binaries*. pp 75–+
- Paczynski B., 1991, *ApJ*, 371, L63

- Parthasarathy M., Branch D., Jeffery D. J., Baron E., 2007, *New Astronomy Review*, 51, 524
- Patterson J., 1998, *PASP*, 110, 1132
- Patterson J., Thorstensen J. R., Kemp J., 2005, *PASP*, 117, 427
- Peraiah A., 1983, *Journal of Astrophysics and Astronomy*, 4, 11
- Politano M., Weiler K. P., 2006, *ApJ*, 641, L137
- Pollacco D. L., et al., 2006, *PASP*, 118, 1407
- Pont F., et al., 2008, *A&A*, 487, 749
- Pont F., Zucker S., Queloz D., 2006, *MNRAS*, 373, 231
- Pravdo S. H., Shaklan S. B., 2009, *ApJ*, 700, 623
- Press W. H., 1978, *Comments on Astrophysics*, 7, 103
- Press W. H., Teukolsky S. A., Vetterling W. T., Flannery B. P., 1992, *Numerical recipes in FORTRAN. The art of scientific computing*. Cambridge: University Press, —c1992, 2nd ed.
- Rasio F. A., Tout C. A., Lubow S. H., Livio M., 1996, *ApJ*, 470, 1187
- Reach W. T., Kuchner M. J., von Hippel T., Burrows A., Mullally F., Kilic M., Winget D. E., 2005, *ApJ*, 635, L161
- Reimers D., Koester D., 1982, *A&A*, 116, 341
- Roberts D. H., Lehar J., Dreher J. W., 1987, *AJ*, 93, 968
- Roche E., 1859, *Annales de l'Observatoire de Paris*, 5, 353

- Sackett P. D., 1999, in Mariotti J.-M., Alloin D., eds, NATO ASIC Proc. 532: Planets Outside the Solar System: Theory and Observations Searching for Unseen Planets via Occultation and Microlensing. pp 189–+
- Santos N. C., 2008, *New Astronomy Review*, 52, 154
- Sato B., et al., 2003, *ApJ*, 597, L157
- Sato Y., Tamura M., Kandori R., Nakajima Y., Kusakabe N., Hashimoto J., Kudo T., Saito H., Kitamura Y., Kawamura A., Nishiyama S., Sunada K., Ueno M., 2008, *PASJ*, 60, 429
- Scargle J. D., 1982, *ApJ*, 263, 835
- Schatzman E., 1945, *Annales d'Astrophysique*, 8, 143
- Schatzman E. L., 1958, *White dwarfs*
- Schmidt G. D., Smith P. S., Harvey D. A., Grauer A. D., 1995, *AJ*, 110, 398
- Schmidt G. D., Szkody P., Silvestri N. M., Cushing M. C., Liebert J., Smith P. S., 2005, *ApJ*, 630, L173
- Schönberg M., Chandrasekhar S., 1942, *ApJ*, 96, 161
- Schreiber M. R., Gänsicke B. T., 2003, *A&A*, 406, 305
- Schwarzenberg-Czerny A., 1991, *MNRAS*, 253, 198
- Seager S., Mallén-Ornelas G., 2003, *ApJ*, 585, 1038
- Silk J., 1991, *Science*, 251, 537
- Silvotti R., et al., 2007, *Nature*, 449, 189

- Simon A., Szatmáry K., Szabó G. M., 2007, *A&A*, 470, 727
- Sion E. M., Greenstein J. L., Landstreet J. D., Liebert J., Shipman H. L., Wegner G. A., 1983, *ApJ*, 269, 253
- Smith A. M. S., et al., 2006, *MNRAS*, 373, 1151
- Steele P. R., Burleigh M. R., Farihi J., Gänsicke B. T., Jameson R. F., Dobbie P. D., Barstow M. A., 2009, *A&A*, 500, 1207
- Stellingwerf R. F., 1978, *ApJ*, 224, 953
- Szabó G. M., Szatmáry K., Divéki Z., Simon A., 2006, *A&A*, 450, 395
- Taam R. E., Sandquist E. L., 2000, *ARA&A*, 38, 113
- Tamanaha C. M., Silk J., Wood M. A., Winget D. E., 1990, *ApJ*, 358, 164
- Tamura M., et al., 2006, in Society of Photo-Optical Instrumentation Engineers (SPIE) Conference Series Vol. 6269 of Society of Photo-Optical Instrumentation Engineers (SPIE) Conference Series, Concept and science of HiCIAO: high contrast instrument for the Subaru next generation adaptive optics
- Tamuz O., Mazeh T., Zucker S., 2005, *MNRAS*, 356, 1466
- Tinetti G., Vidal-Madjar A., Liang M.-C., Beaulieu J.-P., Yung Y., Carey S., Barber R. J., Tennyson J., Ribas I., Allard N., Ballester G. E., Sing D. K., Selsis F., 2007, *Nature*, 448, 169
- Udalski A., Paczynski B., Zebrun K., Szymanski M., Kubiak M., Soszynski I., Szweczyk O., Wyrzykowski L., Pietrzynski G., 2002, *Acta Astronomica*, 52, 1

- van den Besselaar E. J. M., Greimel R., Morales-Rueda L., Nelemans G., Thorstensen J. R., Marsh T. R., Dhillon V. S., Robb R. M., Balam D. D., Guenther E. W., Kemp J., Augusteijn T., Groot P. J., 2007, *A&A*, 466, 1031
- van Loon J. T., 2008, *Memorie della Societa Astronomica Italiana*, 79, 412
- van Zyl L., et al., 2004, *MNRAS*, 350, 307
- Verbunt F., Zwaan C., 1981, *A&A*, 100, L7
- Villaver E., Livio M., 2007, *ApJ*, 661, 1192
- Wall J. V., Jenkins C. R., 2003, *Practical Statistics for Astronomers*. Princeton Series in Astrophysics
- Weidemann V., Koester D., 1983, *A&A*, 121, 77
- Werner K., Rauch T., Kruk J. W., 2008, *A&A*, 492, L43
- West R. G., et al., 2009, *AJ*, 137, 4834
- Willems B., Kolb U., 2004, *A&A*, 419, 1057
- Wilson D. M., 2007, in Afonso C., Weldrake D., Henning T., eds, *Transiting Extragalactic Planets Workshop Vol. 366 of Astronomical Society of the Pacific Conference Series, SuperWASP - Transiting Planet Candidate Selection*. pp 187–+
- Winget D. E., et al., 1994, *ApJ*, 430, 839
- Winget D. E., Kepler S. O., 2008, *ARA&A*, 46, 157
- Winget D. E., Nather R. E., Hill J. A., 1987, *ApJ*, 316, 305
- Winget D. E., Robinson E. L., Nather R. D., Fontaine G., 1982, *ApJ*, 262, L11

Winget D. E., van Horn H. M., Hansen C. J., 1981, ApJ, 245, L33

Winget D. E., van Horn H. M., Tassoul M., Fontaine G., Hansen C. J., Carroll
B. W., 1982, ApJ, 252, L65

Wolszczan A., Frail D. A., 1992, Nature, 355, 145

Wood M. A., 1992, ApJ, 386, 539

Zuckerman B., Koester D., Reid I. N., Hünsch M., 2003, ApJ, 596, 477